Engineering quantum state with light



Hongmin Gao

Oriel College

University of Oxford

A thesis submitted for the degree of

Doctor of Philosophy

Trinity 2021

Acknowledgements

This thesis marks the conclusion of my DPhil studies at the University of Oxford. I would like to take this space to express my gratitude for the support and help I have received over the past four years.

First and foremost, I would like to thank my supervisor, Dieter Jaksch, for the opportunities and guidance he has given me over the past four years. His academic rigour and insightful questions have been a consistent source of inspiration for me throughout. I would also like to thank him particularly for his patience and encouragement when I got awfully stuck (more than we would have liked, probably).

I would also like to thank all members of Jaksch group for the help I have received and for making the past four years such a pleasant experience. I am especially grateful to Frank Schlawin, Jordi Mur-Petit and Jon Coulthard, who all acted as second supervisors at various points in my studies and have been incredibly generous with their time. I feel very fortunate to have collaborated on a number of projects with them. I must also thank Carlos Sánchez Muñoz, who kindly agreed to be my Blender sensei.

I would like to extend my thanks to my friends at Oxford, particularly Guillaume, Rian and Jaume for all the fun we had outside of academic work.

Finally, I am grateful to my family for being my bedrock of support over the years.

Abstract

Controlling the states of quantum systems is a subject of major interest for both fundamental science and technological development. In this thesis, we carry out theoretical studies on how this can be achieved using light, both of classical and of quantum mechanical nature.

We study a driven cavity system, where the driving field is classical and the cavity field is quantum mechanical. We demonstrate how virtual scattering of driving photons inside the cavity via two-photon processes can induce controllable long-range electron interactions in two-dimensional materials. We show that both the strength and the sign of the interactions can be tuned by the driving parameters and that the interactions are not screened effectively except at very low frequencies. For realistic cavity parameters, driving-induced heating of the electrons by inelastic photon scattering is suppressed and coherent electron interactions dominate. When the interactions are attractive, they cause an instability in the Cooper channel at a temperature proportional to the square root of the driving intensity. Our results open up a new avenue for engineering quantum materials on-demand and the possibility of studying the effect of long-range interactions in condensed matter systems.

Following that, we take a more general approach to investigate the effect of long-range density-density electron attractive interactions on a superconductor. We show that the low-lying excitations of a 2D conventional superconductor can be significantly altered by these long-range interactions. Using BCS theory, we find that these interactions combine non-linearly with the intrinsic local attractions of the superconductor to increase the Bogoliubov quasiparticle excitation energies, thus enlarging the superconducting gap. Moreover, we show how the long-range nature of the driven-cavity-induced attractions qualitatively changes the collective excitations of the superconductor. Specifically, they lead to the appearance of additional collective excitations of the excitonic modes. They further

push the Higgs mode "in gap": it lies below the Bogoliubov quasiparticle continuum such that it cannot decay through the quasiparticle excitations.

Contents

1 Introduction **1**

1.1 Contribution of this thesis 5

1.2 Structure of the thesis 6

1.3 Publications 7

1.4 Summary of the last three publications 8

2 Foundational theory: light-matter interaction and many-body physics 11

2.1 Derivation of the light-matter interaction Hamiltonian 11

2.1.1 Electron Hamiltonian 14

2.1.2 EM field Hamiltonian 15

2.2 Matsubara Green's function formalism 15

2.2.1 Retarded functions and linear response theory 16

2.2.2 Matsubara single-particle Green's function 18

2.2.3 Interacting systems, higher-order expansions and Feynman diagrams 20

2.2.3.1 Example: Coulomb interactions and plasma resonance 26

2.2.3.2 Spectral function 28

2.3 Conclusion 30

3 Photoinduced electron pairing in a driven cavity **31**

3.1 Setup 32

3.2 The light-matter interaction Hamiltonian in Coulomb gauge 34

3.3 Light-matter interaction 35

3.3.1 Paramagnetic interactions 35

3.3.2 Diamagnetic interactions 37

3.3.3 Effect of the environment modes 38

3.4 Cavity-mediated interactions 39

3.5 Screening 40

3.6 Cooper channel instability 45
3.7 Conclusion 49

4 A brief review of the BCS theory 50
4.1 BCS mean field theory 50
4.1.1 Mean fields 50
4.1.2 Mean-field Hamiltonian and the gap equation 51
4.1.3 Structure of the spin sector 52
4.1.4 Example: s-wave electron-phonon superconductivity 53
4.1.4.1 Critical temperature 54
4.1.4.2 Zero-temperature gap function 55
4.2 Anderson's pseudospin representation 55
4.2.1 Example cont'd: s-wave electron-phonon superconductivity . . 56
4.2.1.1 Collective modes 58
4.3 Conclusion 60

5 Higgs mode stabilization by photo-induced long-range interactions in a superconductor 62
5.1 Setup 64
5.2 Model 65
5.3 Critical temperature enhancement 66
5.4 Zero-temperature gap structure 68
5.5 Collective modes 70
5.5.1 Excitonic/Bardasis-Schrieffer modes 71
5.5.2 Stabilisation of the Higgs mode 72
5.6 Conclusion 75

6 Conclusions 77

A Proof: connection between Matsubara Green's function and retarded Green's functions 80

B Estimates of Laser Induced Heating 82

C Enhancement of the critical temperature by long-range interactions 85

Bibliography 88

Chapter 1

Introduction

Studies on the properties of quantum matter have long interested physicists and have led to numerous technological advances, including the field of electronics. From smart-phones to solar panels, many semiconductor technologies are based on the band theory, which describes macroscopic system of non-interacting free electron gases moving in static, periodic electric potentials produced by the non-mobile charges [1]. Within this theory, the absence of interactions between electrons allows us to consider the electrons one at a time without having to worry about the effect of one electron on another beyond that of Fermi-Dirac statistics. This simplification greatly simplifies the size of the Hilbert space needed to be considered.

On the other hand, microscopic interactions between the constituent particles through the electromagnetic fields, though complicating the task of analysing the properties of matter (by increasing of the size of the Hilbert space exponentially), allow for the charged particles to correlate with one another to exhibit collective phenomena [2]. One such example of them is the phenomenon of superconductivity, in which electrons pair up and condense into a superfluid of the electron pairs, which conducts electricity without resistance and repels magnetic field in the bulk of the superconducting material [3]. Since its initial discovery by Onnes in 1911 [4] when he measured a sudden drop in the resistivity of mercury at a very low critical temperature, the phenomenon has been found in a wide range of metals and other compounds at different temperatures [5], some even at close to room temperature, albeit under very high pressure [6]. Superconducting materials have found many applications, e.g., inside MRI machines as powerful magnets, and in SQUID magnetometers as components of Josephson junctions. Another striking collective phenomena brought about by interactions is spin-charge separation in one-dimensional quantum systems [7, 8, 9, 10], where the collective excitations of the system exhibit either only charge but no spin, or only spin but no charge. This is in stark contrast to the elementary

excitations of in an electron gas which have both spin and charge degrees of freedom. The separated spin and charge excitation are soliton-like, and they travel at different speeds determined by the microscopic interactions between the underlying electrons.

Since the ability to engineer and control the quantum materials is a necessary step towards utilising their properties for technological purposes, much of the modern research in quantum condensed matter physics is centred on modifying the microscopic details to search for novel phases of matter and improving their functionalities based on the electronic degrees of freedom.

Until relatively recently, researchers have mostly explored modifying quantum matter through means such as chemical doping [11], external pressure [12], lattice straining [13, 14], or exfoliating materials into single atomic layers and combining them into van der Waals crystals [15], which are all quite static compared to electron dynamics. However, there is now a burgeoning field where researchers manipulate the microscopic interactions in the materials using light at terahertz (THz) frequencies, comparable to the speed of electron dynamics.

The developments in photonic technologies have been instrumental for this field. They include intense THz laser pulses [16, 17] and THz photonic cavities in the form of metamaterial resonators which can achieve ultrastrong coupling with 2D electrons [18]. Each of them represents one way to overcome the small value of the fine structure constant ($\alpha \approx 1/137$), which sets the coupling strength between an electron and a single photon[1].

The first class of technology employs the strategy of using a large number, N, of coherent photons to enhance the interaction strength by a factor of $\sqrt{N}$. High intensity, narrowband, shaped pulses in the THz frequencies have allowed researchers to strongly drive specific low-energy degrees of freedom in quantum materials. Instead of simply heating up the quantum system and rendering the quantum state featureless, the radiation can, under some circumstances, change the materials' properties and induce order, albeit only transiently. Examples include driving-induced metal-insulator transitions [20, 21], synthetic magnetic fields [22], switching ferroelectric polarization [23, 24], melting of striped phases [25, 26, 27] or charge density waves [28, 29], and driving-induced transient superconducting-like phases above their intrinsic critical temperature [30, 31, 32, 27, 33]. The inevitable heating caused by the periodic driving, however, poses a major challenge to stabilising the transient behaviour to longer

[1]We are using the term 'photon' rather loosely here, see Ref. [19] for why 'photon' is such a misnomer.

times. In this direction, experimentalists have, for example, used pulses of longer durations (up to 1ns) but lower peak intensity to induce a metastable superconducting state in K_3C_{60} lasting over 10ns [33]. From the theory side, it has been shown that symmetry properties [34] and geometric frustration [35] could protect the quantum state from heating to a featureless infinite temperature state.

On the other hand, the second class of technology, the cavities, takes a different route to enhancing the light-matter interaction by confining the light in real space.

Coupling of matter with light trapped by cavities have been studied extensively in the field of quantum optics since Purcell's demonstration in 1946 that the spontaneous emission of an emitter can be enhanced or suppressed by engineering its electromagnetic environment [36]. There, the cavity is usually a Fabry-Pérot resonator formed by a pair of highly (but not perfectly) reflective mirrors; the (small) half-width of the cavity's resonance comes from the imperfect reflectivity. The resonance is typically in the optical frequencies and the well-defined spatial mode of the cavity couples to the dipolar transitions between the internal state of atoms. We can think of the enhancement of light-matter interactions (compared to in free space) to be due to the trapped photon having a higher chance of interacting with the atoms as it bounces between the two mirrors many times before leaking out of the cavity. The strength of coupling between the cavity mode excitation and the atomic dipole transition can be characterized by the Rabi frequency, Ω, which describes how fast the dipole transition happens in the atom due to the light field. In the context of light-atom coupling, Ω gives the rate at which an excitation (or energy) is transferred between the cavity and the atom. When the Rabi frequency becomes greater than the spontaneous decay rate of the atom and the cavity decay rate, an excitation can be coherently transferred back-and-forth between the atom and cavity, and we enter the so-called 'strong coupling' regime, which has been achieved with atoms [37, 38, 39, 40] as well as with particle-hole excitons in semiconductors [41, 42, 43, 44, 45].

Despite that both intense laser light and cavity confinement both enhance light-matter coupling by increasing the electromagnetic field 'strength' in some sense, the nature of their fields are very different. In contrast to the intense laser light, which is well-described by a classical electromagnetic field with a well-defined phase, the light field of a cavity usually necessitates a quantum mechanical description with uncertainties in both the phase and the amplitude of the field. The quantum fluctuation of the cavity electromagnetic field plays a key role such that even an empty cavity with $\langle E \rangle = 0$ (i.e., the expectation value of the electric field strength E is zero) can shift the energy levels of the matter coupled to it [46, 47]. The cavity confinement of

light field greatly amplifies the field fluctuation. This is particularly true for terahertz cavities, whose cavity mode volume can be compressed below the diffraction limit by as much as five orders of magnitude such that ultrastrong light-matter coupling can be achieved with even empty cavities [18, 48, 49]. This avoids the issue of heating caused by periodic (Floquet) driving, yet at the same time, due to the close analogy between the Floquet-Hilbert space of a periodically driven quantum system and the Hilbert space of a coupled cavity-matter system, the strong coupling to the cavity field could realise quantum states similar to those achieved through driving [50] but with much longer lifetimes. This connection (a crossover) between a Floquet system and a cavity-coupled system has recently been elucidated in Ref. [51].

Inspired by the aforementioned observations of transient superconducting-like states above the equilibrium critical temperature in Fullerene superconductors by strong periodic driving of a local molecular vibration [32, 33], researchers have coupled the phonon mode of Rb_3C_{60} that is thought to assist superconductivity at equilibrium to an empty terahertz plasmonic cavity [52]. In this experiment, a 50% increase of the superconducting critical temperature of Rb_3C_{60} was reported. In contrast to the experiments using strong driving, the superconductivity in this experiment is at equilibrium. Theorists studied similar setups and explained the enhancement of electron-phonon interactions due to the coupling to light [53, 54]. Another theoretical result with a similar theme is the prediction of an enhancement of the superconducting gap when the superconductor is coupled to a cavity through a mechanism analogous to the Eliashberg effect of microwave radiations on superconductors [55, 56, 57, 58]. Meanwhile, theory began exploring cavity-coupled, strongly-correlated lattice models, such as the Hubbard model, whose properties (particularly spin-exchange correlations) under strong periodic driving have been investigated in recent years [59, 60, 61]. At low cavity photon numbers, the difference between Floquet driving and quantum field fluctuations is expected to be most significant. For example, long-range interactions are mediated by the cavity when the repulsive Hubbard model is below half-filling; and they play a crucial role in determining the ground state properties [62]. These interactions do not exist when the model is Floquet-driven [60]. This is because, unlike cavities, the classical periodic driving gives an excitation spectrum that is not bounded from below, such that the correlated-hopping amplitudes due to virtual absorption and emission of quanta of driving energy destructively interfere. Ref. [63] took advantage of this fact and showed that the electronic order of an attractive Hubbard model coupled to a cavity with few photons could be selectively enhanced by changing the cavity frequency.

In addition to Floquet engineering, valuable insights and inspirations also came from more extensively studied quantum optical systems. One of such systems is a (pumped) cavity-coupled semiconductor quantum well, in which the cavity field dresses the excitons in the semiconductors quantum well to produce a exciton-polariton condensate [64]. These nonequilibrium steady states of coupled light and matter have applications in quantum simulations [65] as well as quantum information processing [66]. They have even been proposed to mediate superconductivity [67, 68, 69]; the proposal of cavity-mediated Amperean pairing of electrons [70] was partially inspired by these studies. Building on the knowledge of polaritons, cavities have recently been used to change molecular properties [71, 72, 73, 74, 75], conductance of organic semiconductors [76, 77, 78], and magnetotransport of 2D electron gases [79, 80]. Studies of driven cavity systems [81, 82, 83] also had influence from cavity-coupled ultracold atomic gases, for which well-established techniques exist for cooling, real-time atomic position monitoring as well as creating tailored long-range interactions [84].

1.1 Contribution of this thesis

The present thesis belongs to this broad theme of controlling quantum matter using light. We contribute to the field by proposing a novel method that utilises both an intense THz laser and a THz cavity to engineer long-range electron interactions in materials, and also by predicting the effects of such interactions on superconductors. In this way, the thesis has two parts.

In the first part, we consider the coupling of two-dimensional electron systems to both the periodic driving of a laser and the vacuum fluctuation of a terahertz cavity. We demonstrate how virtual scattering of laser photons inside a cavity via two-photon processes can induce controllable long-range electron interactions in the two-dimensional materials. We find that these interactions are not screened effectively except at very low frequencies and that for realistic cavity parameters, laser-induced heating of the electrons by inelastic photon scattering is suppressed and coherent electron interactions dominate. With red-detuned driving (relative to the cavity frequency), the interactions are attractive, and they can cause an instability in an electron gas in the Cooper channel at a temperature proportional to the square root of the driving intensity. These results provide a novel route for engineering electron interactions in a wide range of two-dimensional materials including AB-stacked bilayer graphene and the conducting interface between $LaAlO_3$ and $SrTiO_3$. In contrast to previous studies on tuneable cavity-mediated long-range interactions which almost

exclusively considered ultracold atom experimental setups, this work opens the possibility of implementing and studying long-range interactions in electron systems as well as controlling quantum phases of matter through on-demand quantum systems engineering.

In the second part, we apply these interactions to a superconductor whose superconducting phase is induced by local electron attractions. In these systems, the intrinsic local electron attractions and the driven-cavity-induced long-range attractions combine in a non-linear way to qualitatively change the excitations in superconducting state. Focusing on the zero-temperature limit, we show that the Bogoliubov quasiparticle excitation energies are enhanced by the induced interactions. Moreover, we show how the long-range nature of the driven-cavity-induced attractions qualitatively changes the collective excitations of the superconductor. Specifically, they lead to the appearance of additional collective excitations of the excitonic modes. More strikingly, the long-range interactions allow for the stabilization of the Higgs mode, which is usually damped by quasiparticle excitations and decays rapidly. Unlike the few other known mechanisms for stabilizing the Higgs mode, ours does not require strong disorder or coexisting charge-density-wave orders. Hence, this method can be applied to a range of superconducting materials. Our work forms an important step towards experimental detection, investigation and utilization of the Higgs mode in superconductors.

1.2 Structure of the thesis

In Chapter. 2, we set the stage for the rest of the thesis by first deriving a very general (non-relativistic and quantized) Hamiltonian describing a system of interacting light and matter. This prepares us to obtain a Hamiltonian describing the setup we consider in Chapter. 3. We also introduce the Matsubara Green's function formalism for quantum many-body physics, which we apply in Chapter. 3 to study the effects of light-matter interactions, particularly electron screening, in the system considered.

In Chapter. 3, we present and explain our proposal for inducing controllable long-range electron interactions in two-dimensional materials using an external laser and a cavity. We show that laser light that is red(blue)-detuned from the cavity yields attractive(repulsive) interactions, whose strength is proportional to the laser intensity. Equiped with Matsubara Green's function formalism introduced in Chapter. 2, we discuss screening of the interactions by the electrons and show that it is negligible except at very low frequencies. We also discuss laser-induced heating in the system.

We then consider the case when the interactions are attractive, and show that they cause an instability in the Cooper channel at a temperature proportional to the square root of the driving intensity.

In the following parts of the thesis, we explore how these induced long-range interactions alter the properties of BCS superconductors. We study the combined effect of induced and intrinsic attractive interactions using BCS theory, which we briefly review in Chapter. 4. In Chapter. 4, we also introduce Anderson's pseudospin representation of BCS mean-field theory. It is used to describe the collective excitations (including the Higgs mode) in the superconductor. For concreteness and in preparation for Chapter. 5, we take the s-wave conventional superconductor as an example, and calculate properties such as critical temperature, zero-temperature gap and the Higgs mode energy using the theory framework presented in the chapter.

Building on the previous chapters, in Chapter. 5, we study the low-lying excitations of a 2D superconductor when we impose upon it the controllable long-range attractive interactions discussed in Chapter. 3. We use BCS theory to study the increase of the Bogoliubov quasiparticle excitation energies and the BCS critical temperature due to these long-range interactions. Using Anderson's pseudospin representation introduced in Chapter. 4, we furthermore find that the long-range interactions lead to the appearance of additional collective excitations of the excitonic modes, and stabilise the Higgs mode, which are usually damped by the quasiparticle excitations.

Finally, we summarise our results and suggest possibilities for future directions of research in Chapter. 6.

1.3 Publications

Some of the results presented in this thesis were published/presented as

1. H. Gao, F. Schlawin, M. Buzzi, A. Cavalleri, and D. Jaksch, Photoinduced Electron Pairing in a Driven Cavity, *Phys. Rev. Lett.* **125**, 053602 (2020)

2. H. Gao, F. Schlawin, and D. Jaksch, Higgs mode stabilization by photo-induced long-range interactions in a BCS superconductor, *arXiv* 2106.05076 (2021)

The author also co-authored the following publications over the course of the DPhil:

3. H. Gao, J. R. Coulthard, D. Jaksch, and J. Mur-Petit, Controlling magnetic correlations in a driven Hubbard system far from half-filling, *Phys. Rev. A* **101**, 053634 (2020)

4. H. Gao, J. R. Coulthard, D. Jaksch, and J. Mur-Petit, Anomalous Spin-charge Separation in a Driven Hubbard System, *Phys. Rev. Lett.* **125**, 195301 (2020)

5. J. Tindall, F. Schlawin, M. Buzzi, D. Nicoletti, J. R. Coulthard, H. Gao, A. Cavalleri, M. A. Sentef, and D. Jaksch, Dynamical Order and Superconductivity in a Frustrated Many-Body System, *Phys. Rev. Lett.* **125**, 137001 (2020)

1.4 Summary of the last three publications

Items 3, 4 and 5 of the aforementioned publications form different but related research topics from the focus of this thesis; the result therein are only summarised here. Unlike the present thesis, those three publications do not involve the quantum nature of light. However, all of them involve strong classical driving on the Hubbard model which causes the microscopic parameters of the model to oscillate periodically in time. The strength of the classical driving distinguishes those pieces of work from the content of this thesis: the energy scale associated with the amplitudes of the oscillations considered in those papers are comparable to the energy scale associated with the frequencies of the oscillations. In this sense, the classical driving used there is stronger than the driving considered in this thesis by orders of magnitudes. The implication of this fact is that effects of Floquet driving that are negligible in the systems considered in this thesis, e.g., suppression of single-particle hopping in the dynamics of the driven Hamiltonian, become appreciable. Consequently, those effects lead to exotic behaviours of the fermionic system which we discuss in those publications.

In the following, we summarise the key results from each of the three publications.

- H. Gao, J. R. Coulthard, D. Jaksch, and J. Mur-Petit, Controlling magnetic correlations in a driven Hubbard system far from half-filling, *Phys. Rev. A* **101**, 053634 (2020)

This and the next publication are partially inspired by the experimental platform of ultracold atoms in optical lattices and their capabilities to simulate models relevant for condensed matter physics both in and out of equilibrium (for example, because of periodic driving).

In this article, we investigate the behaviour of a strongly repulsive Hubbard model under periodic driving of its lattice. When the driving is fast and off-resonant, we show analytically that the effective (non-time-periodic) Hamiltonian describing the dynamics of this system is the t-J model with additional pair hopping terms, whose

parameters can all be controlled by the drive. We then demonstrate numerically using tensor network methods for a 1D lattice that a slow modification of the driving strength allows near-adiabatic transfer of the system from the ground state of the underlying Hubbard model to the ground state of the effective t-J Hamiltonian. This way, we propose using ultracold fermionic atoms trapped in a periodically shaken optical lattice as a quantum simulator of the t-J Hamiltonian, which describes the dynamics in doped antiferromagnets, and is thought to be relevant to the problem of high-temperature superconductivity in the cuprates.

This technique allows us to access an unusual parameter regime of the t-J Hamiltonian (when the driving is strong) in which the single-particle hopping amplitude (t) is no longer dominant compared to the spin-exchange interaction strength (J), leading to novel behaviours. As an example, we report exact diagonalization calculations illustrating the binding and the anisotropic dynamics of spin-singlet pairs in 2D lattices as a result of strong driving.

These results open new routes to explore the interplay between density and spin in strongly-correlated fermionic systems through their out-of-equilibrium dynamics, and motivate the following publication.

- H. Gao, J. R. Coulthard, D. Jaksch, and J. Mur-Petit, Anomalous Spin-charge Separation in a Driven Hubbard System, *Phys. Rev. Lett.* **125**, 195301 (2020)

Building on the previous work, we consider the same system but at a higher fermion density (close to half-filling), and study the spin-charge separation in the system. Spin-charge separation (SCS) is a striking manifestation of strong correlations in low-dimensional quantum systems, whereby a fermion splits into separate spin and charge excitations that travel at different speeds. Here, we demonstrate that periodic driving enables control over SCS in a Hubbard system near half-filling. In one dimension, we predict analytically an exotic regime where charge travels slower than spin and can even become 'frozen', in agreement with numerical calculations. In two dimensions, the driving slows both charge and spin, and leads to complex interferences between single-particle and pair-hopping processes.

- J. Tindall, F. Schlawin, M. Buzzi, D. Nicoletti, J. R. Coulthard, H. Gao, A. Cavalleri, M. A. Sentef, and D. Jaksch, Dynamical Order and Superconductivity in a Frustrated Many-Body System, *Phys. Rev. Lett.* **125**, 137001 (2020)

In this work led by Dr. J. Tindall, we study a system with spatial anisotropy and geomentric frustration under strong periodic modulation of the Hubbard model parameters. This is in part motivated by a recent experimental observation of photoinduced superconductivity in κ-(BEDT-TTF)$_2$Cu[N(CN)$_2$]Br molecules, and in part by the rich equilibrium phase diagrams spatial anisotropy and frustration can lead to in triangular lattice structures, with regions containing complex, highly entangled states of matter. In this work, we study the driven two-rung triangular Hubbard model and evolve these states out of equilibrium, observing how the interplay between the driving and the initial state unexpectedly shuts down the particle-hole excitation pathway. This restriction, which symmetry arguments fail to predict, dictates the transient dynamics of the system, causing the available particle-hole degrees of freedom to manifest uniform long-range order.

Chapter 2

Foundational theory: light-matter interaction and many-body physics

In this chapter, we first set the stage by deriving a general, non-relativistic Hamiltonian describing a system of interacting light and crystalline matter starting from the Lagrangian. We do so in the Coulomb gauge. This result will be directly useful towards obtaining a Hamiltonian describing the driven, cavity-coupled 2D electron system which we study in the next chapter. We then review the Matsubara Green's function method for quantum many-body systems. The method will be applied to the electron-photon system in the next chapter when we investigate properties such as screening and pairing instabilities in the system.

2.1 Derivation of the light-matter interaction Hamiltonian

In this section, we outline how to derive the light-matter Hamiltonian. Following the approach in Ref. [85], we include both the mobile electrons and the positively charged background, which we assume to be non-magnetic. Since we are mainly interested in the interaction between electrons and photons, we assume that the background atoms move so slowly that their centres of mass are fixed. This way we freeze out the phonons. As the electrons bound to the atoms from the background material can still oscillate around their nuclei, the background is polarizable. We model the total displacement field of the background material alone as $\boldsymbol{D}_{\text{bg}} = \boldsymbol{D}_{static} + \boldsymbol{P}$, where $\boldsymbol{\nabla} \cdot \boldsymbol{D}_{static} = \rho_{\text{bg}}(\boldsymbol{r}) = \sum_{j \in \text{bg}} Q_j \delta(\boldsymbol{r} - \boldsymbol{r}_j)$ and the bulk polarization, $\boldsymbol{P}(\boldsymbol{r}, t) = \epsilon_0 \chi_{\text{bg}} \mathbf{E}(\boldsymbol{r}, t)$, where $\mathbf{E}$ is the net electric field strength at $\boldsymbol{r}$ and time t, ϵ_0 is the vacuum permittivity. We have expressed the background charge distribution as a sum over

the collection of stationary particles $\{j\}$, with charge $\{Q_j\}$ at position $\{\boldsymbol{r}_j\}$. We have also approximated this polarization using a phenomenological polarizability constant χ_{bg}, that is independent of position and frequency.

To derive the full light-matter Hamiltonian, we start from the usual Lagrangian formulation of charged particles interacting with the electromagnetic field with background polarizability incorporated,

$$L = \sum_{j=1}^{N} \left[\frac{1}{2} m_j \dot{\boldsymbol{r}}_j^2 + Q_j \dot{\boldsymbol{r}} \cdot \mathbf{A}(\boldsymbol{r}_j, t) - Q_j \phi(\boldsymbol{r}_j, t)\right] + \frac{\epsilon_0}{2} \int \mathrm{d}^3\boldsymbol{r} \left[\epsilon_r \mathbf{E}^2(\boldsymbol{r}, t) - c^2 \mathbf{B}^2(\boldsymbol{r}, t)\right], \tag{2.1}$$

where m_j is the mass of particle j (either a mobile electron or a stationary background charged atom) with electric charge Q_j located at $\boldsymbol{r}_j$, where the net electrical potential is $\phi(\boldsymbol{r}_j, t)$, and the vector potential is $\mathbf{A}$. $\dot{\boldsymbol{r}}$ means the time derivative of $\boldsymbol{r}$. The electric and magnetic field strengths are denoted by $\mathbf{E}$ and $\mathbf{B}$ respectively. c is the speed of light in vacuum, $\epsilon_r = 1 + \chi_{\text{bg}}$. The first term of Eq. (2.1) describes light-matter interaction, while the second term is the light field in the polarizable medium formed by the background atoms.

Following the usual procedures of Legendre transformation outlined in Ref. [85], we obtain the Hamiltonian in Coulomb gauge, where the vector potential $\mathbf{A}$ is the transverse component ($\boldsymbol{\nabla} \cdot \mathbf{A} = \mathbf{0}$) and the scalar potential ϕ is the longitudinal component.

$$H = \sum_{j=1}^{N} \left[\frac{(\boldsymbol{p}_j - Q_j \mathbf{A}(\boldsymbol{r}_j, t))^2}{2m_j} + \frac{1}{2} Q_j \phi(\boldsymbol{r}_j, t)\right] + \frac{\epsilon_0}{2} \int \mathrm{d}^3\boldsymbol{r} \left[\epsilon_r \dot{\mathbf{A}}^2 - c^2 \mathbf{A} \cdot \nabla^2 \mathbf{A}\right] \tag{2.2}$$

Here, $\boldsymbol{p}_j$ is the conjugate momentum of $\boldsymbol{r}_j$, and we assume the fields decay to zero at the boundaries infinitely far away. We also have $\phi(\boldsymbol{r}) = \sum_j \frac{Q_j}{4\pi\epsilon_0\epsilon_r|\boldsymbol{r}-\boldsymbol{r}_j|}$.

We note that calculations may also be done in a different gauge. In fact, for calculations involving resonant coupling, the dipolar gauge is better suited [86], but it leads to a more complicated interaction terms. In this thesis, we keep away from resonances so the Coulomb gauge is appropriate and the resulting interactions are particularly simple.

The particle index above runs over both mobile electrons and background particles. Since the latter are treated as stationary, their kinetic energies are ignored and their positions are treated as parameters instead of variables. Thus, the Coulomb energy between them is a constant and the Coulomb energy between electrons and

background atoms forms a static potential $V_b(\boldsymbol{r})$ for the electrons. Thus, the total potential energy of the electron j due to the background charges is $V_{bg}(\boldsymbol{r}_j) = -eV_b(\boldsymbol{r}_j)$, where $-e$ is the electron charge. The Hamiltonian [Eq. (2.2)] becomes,

$$H = \sum_{j\in e^-}\Big[\frac{\left(\boldsymbol{p}_j + e\mathbf{A}(\boldsymbol{r}_j,t)\right)^2}{2m} + V_{bg}(\boldsymbol{r}_j)\Big] + \frac{1}{2}\sum_{\substack{j\neq k\\ j,k\in e^-}}\frac{e^2}{4\pi\epsilon_0\epsilon_r|\boldsymbol{r}_j-\boldsymbol{r}_k|} + \frac{\epsilon_0}{2}\int \mathrm{d}^3\boldsymbol{r}\,\Big[\epsilon_r\dot{\mathbf{A}}^2 - \mathbf{A}\cdot\nabla^2\mathbf{A}\Big]. \quad (2.3)$$

Here, m is the bare electron mass.

The vector potential $\mathbf{A}$ satisfies the following equation (due to Maxwell's equations) [85]

$$\left(\nabla^2 - \frac{\epsilon_r}{c^2}\frac{\partial^2}{\partial t^2}\right)\mathbf{A}(\boldsymbol{r},t) = -\mu_0\left(\sum_j Q_j\boldsymbol{v}_j\delta(\boldsymbol{r}-\boldsymbol{r}_j) - \epsilon_0\epsilon_r\boldsymbol{\nabla}\frac{\partial\phi}{\partial t}\right) \quad (2.4)$$

Here, $\boldsymbol{v}_j$ is the velocity of particle j (which is only nonzero for mobile electrons). The second term on the RHS of Eq. (2.4) corresponds to the displacement current density that is due to the mobile electrons.

Since we will later consider a driven cavity system, we make a distinction now between (i) the driving field that is highly populated by a coherent state and can be described as a classical field, and (ii) the remaining field mdoes that are not highly populated and needs to be quantized. We do so by writing the solution to Eq. (2.4) as a mode expansion of the EM field plus the driving transverse field whose vector potential oscillates with angular frequency ω_L (of the driving laser) and amplitude $\mathbf{A}_d$. We treat the latter as a classical field. In this way, we have

$$\mathbf{A}(\boldsymbol{r},t) = \sum_q \mathcal{A}_q\mathcal{C}_q(t)\boldsymbol{u}_q(\boldsymbol{r}) + \mathbf{A}_d\sin(q_Lz - \omega_Lt). \quad (2.5)$$

q_L refers to the driving mode photon wavevector that we fix to lie along the z-axis. $\boldsymbol{u}_q(\boldsymbol{r})$ are transverse photon mode functions that form a complete and orthonormal basis and satisfy

$$\left(\nabla^2 + \frac{\epsilon_r\omega_q^2}{c^2}\right)\boldsymbol{u}_q(\boldsymbol{r}) = 0\ , \quad (2.6)$$

where ω_q is the frequency the mode labelled q oscillates at. The mode functions depend on the boundary condition we impose. If we consider that the light modes are confined inside a box with periodic boundary conditions, the mode functions are complex travelling waves. On the other hand, if we choose a open boundary condition, the mode functions are real.

With this mode decomposition, we can rewrite the free EM field in the Hamiltonian Eq. (2.3) as

$$H_{\text{free EM field}} = \frac{\epsilon_0}{2} \sum_{q\in\{c,q_e\}} \mathcal{A}_q^2(1+\chi_{\text{bg}})\Big[\pi_q\pi_{-q} + \omega_q^2 \mathcal{C}_q\mathcal{C}_{-q}\Big] = \frac{1}{2}\sum_q \Big[\pi_q\pi_{-q} + \omega_q^2\mathcal{C}_q\mathcal{C}_{-q}\Big], \tag{2.7}$$

where $\pi_q = \dot{\mathcal{C}}_{-q}$ is the conjugate momentum for $\mathcal{C}_q$, $\mathcal{C}_{-q} = \mathcal{C}_q$ when q refers to a mode with open boundary condition, e.g. the cavity mode that we will describe in the next chapter. In the above, the normalisation constant is defined as $\mathcal{A}_q = \frac{1}{\sqrt{\epsilon_0(1+\chi_{\text{bg}})}} \equiv \frac{1}{\sqrt{\epsilon_0\epsilon_r}}$.

Combining the above discussion with Eq. (2.3), we arrive at the full Hamiltonian,

$$H = \sum_{j\in e^-}\Big[\frac{\Big(\boldsymbol{p}_j + e\Big[\frac{1}{\sqrt{\epsilon_0\epsilon_r}}\sum_q \mathcal{C}_q(t)\boldsymbol{u}_q(\boldsymbol{r}_j) + \mathbf{A}_d\sin(q_L z - \omega_L t)\Big]\Big)^2}{2m} + V_{bg}(\boldsymbol{r}_j)\Big] + \frac{1}{2}\sum_{\substack{j\neq k\\ j,k\in e^-}} \frac{e^2}{4\pi\epsilon_0\epsilon_r|\boldsymbol{r}_j - \boldsymbol{r}_k|} + \frac{1}{2}\sum_q\Big[\pi_q\pi_{-q} + \omega_q^2\mathcal{C}_q\mathcal{C}_{-q}\Big]. \tag{2.8}$$

We obtain the Hamiltonian for the quantum system through canonical quantisation of the above classical Hamiltonian.

2.1.1 Electron Hamiltonian

The electron field can be quantised by imposing the commutation relation

$$\big[(\boldsymbol{r}_j)_l, (\boldsymbol{p}_k)_m\big] = \mathrm{i}\hbar\delta_{j,k}\delta_{l,m}. \tag{2.9}$$

$\boldsymbol{r}_j$ and $\boldsymbol{p}_j$ are now operators and j and k are particle indices while l and m are spatial dimensional indices.

We expand out Eq. (2.8) to separate out the terms describing the independent electrons,

$$H_{el} = \sum_{j\in e^-}\frac{\boldsymbol{p}_j^2}{2m} + V_{bg}(\boldsymbol{r}_j) \tag{2.10}$$

This single-particle part of the Hamiltonian can be second-quantised by choosing the Bloch states that diagonalises Eq. (2.10). We denote the eigenfunctions as $\Psi_{\mathbf{k},l,\sigma}(\boldsymbol{r}) = e^{\mathrm{i}\mathbf{k}\cdot\boldsymbol{r}}\phi_{\mathbf{k},l,\sigma}(\boldsymbol{r})$, where $\phi_{\mathbf{k},l,\sigma}(\boldsymbol{r})$ has the periodicity of the lattice. We define the field operator for the electrons, $\psi^\dagger(\boldsymbol{r}) = \sum_{\mathbf{k}} \Psi^*_{\mathbf{k},l,\sigma}(\boldsymbol{r})c^\dagger_{\mathbf{k},l,\sigma}$, where $c^\dagger_{\mathbf{k},l,\sigma}$ is the

fermionic creation operator for an electron in a state in Bloch band l with quasi-momentum $\mathbf{k}$ and spin σ. Eq. (2.10) is thus diagonal in quasi-momentum space, $H_{el} = \sum_{\mathbf{k},l,\sigma} \epsilon_{\mathbf{k},l,\sigma} c^\dagger_{\mathbf{k},l,\sigma} c_{\mathbf{k},l,\sigma}$, where $\epsilon_{\mathbf{k},l,\sigma}$ is the electron dispersion. For this thesis, we focus on single-band electrons, so we drop the band index from now on. The couplings to the transverse light fields do not affect the choice of Bloch state basis. In this chapter, we do not use the second-quantised form for the electrons for notational compactness, but we will do so in the next chapter.

2.1.2 EM field Hamiltonian

The EM field can be quantised by imposing the commutation relation

$$[\mathcal{C}_{q_1}, \pi_{q_2}] = \mathrm{i}\hbar\delta_{q_1,q_2} \tag{2.11}$$

We second-quantise this part of the Hamiltonian by defining $\pi_q = \text{-i}\sqrt{\frac{\hbar\omega_q}{2}}\left(b_{-q} - b_q^\dagger\right)$ and $\mathcal{C}_q = \sqrt{\frac{\hbar}{2\omega_q}}\left(b_q + b_{-q}^\dagger\right)$. ($b_{-q} = b_q$ if q the mode function is real.) Eq. (2.11) implies that b_q and $b_q^\dagger$ are bosonic annihilation and creation operators.

Collecting everything together, we arrive at the quantised Hamiltonian for the mobile electrons and the electromagnetic field (which is second quantised) in Coulomb gauge,

$$H = \sum_{j\in e^-}\Big[\frac{\left(\boldsymbol{p}_j + e\sum_q \sqrt{\frac{\hbar}{2\epsilon_0\epsilon_r\omega_q}}\boldsymbol{u}_q(\boldsymbol{r}_j)(b_q + b_{-q}^\dagger) + e\mathbf{A}_d\sin(q_L z - \omega_L t)\right)^2}{2m} + V_{bg}(\boldsymbol{r}_j)\Big]$$
$$+ \frac{1}{2}\sum_{\substack{j\neq k\\ j,k\in e^-}} \frac{e^2}{4\pi\epsilon_0\epsilon_r|\boldsymbol{r}_j - \boldsymbol{r}_k|} + \sum_q \hbar\omega_q(b_q^\dagger b_q + \frac{1}{2}). \tag{2.12}$$

This Hamiltonian describes the full light-electron system. In the next chapter, we will specifiy this further for the system setup we consider, and we will expand out and investigate each of the light-matter coupling terms.

2.2 Matsubara Green's function formalism

In this section, we introduce the Matsubara Green's functions and the diagrammatic method for dealing with interacting quantum systems at finite temperatures. Throughout the section, $\hat{H}$ denotes a time-independent Hamiltonian. We will introduce specifications to it as we progress. Since there will be quite a few capital letters

representing various operators, operators that denote terms from the Hamiltonian in this section will wear hats for clarity.

2.2.1 Retarded functions and linear response theory

The requirement of causality in physics means that retarded functions are central to properties of matter. For example, when discussing screening in this thesis, we will make use of the response functions to density perturbations, which are captured by retarded correlations between density operators [87]. To see this, we invoke linear response theory to consider the effect on the electron density by an external perturbation in momentum modes $\pm\mathbf{q}$ by Hamiltonian $\hat{H}_{\text{ext}}(t)$ (which is in the interaction picture defined by the time-independent Hamtiltonian $\hat{H}$)

$$\hat{H}_{\text{ext}}(t) = [\rho_{\mathbf{q}}(t) + \rho_{-\mathbf{q}}(t)]f(t) \tag{2.13}$$

$$\rho_{\mathbf{q}}(t) = \mathrm{e}^{\frac{\mathrm{i}}{\hbar}\hat{H}t}\rho_{\mathbf{q}}\mathrm{e}^{-\frac{\mathrm{i}}{\hbar}\hat{H}t} \tag{2.14}$$

$$\rho_{\mathbf{q}} = \sum_{\mathbf{k}\sigma} c^{\dagger}_{\mathbf{k}+\mathbf{q}\sigma}c_{\mathbf{k}\sigma}, \tag{2.15}$$

where $\rho_{\mathbf{q}}$ is the density operator[1] in momentum mode $\mathbf{q}$ (we have suppressed the band index since for this thesis we consider a single electronic band), and $f(t)$ is regulated by a Heaviside $\Theta(t)$, which means the perturbation is switched on at $t = 0$, and prior to that the system is in thermal equilibrium under $\hat{H}$. In this interaction picture, the time evolution of the expectation value of the density operator is

$$\frac{1}{\mathcal{Z}}\mathrm{Tr}\Big[\mathrm{e}^{-\beta\hat{H}}U^{-1}(t)\rho_{\mathbf{q}}(t)U(t)\Big] \equiv \langle U^{-1}(t)\rho_{\mathbf{q}}(t)U(t)\rangle, \tag{2.16}$$

where $\langle\ldots\rangle$ denotes thermal averaging, and

$$\mathcal{Z} = \mathrm{Tr}\Big[\mathrm{e}^{-\beta\hat{H}}\Big] \tag{2.17}$$

$$U(t) = \mathcal{T}\exp\left\{-\frac{\mathrm{i}}{\hbar}\int_0^t \mathrm{d}t'\ \hat{H}_{\text{ext}}(t')\right\}. \tag{2.18}$$

$\mathcal{T}$ stands for time-ordering [88]:

$$\mathcal{T}c_{\mathbf{k}\sigma}(t_1)c^{\dagger}_{\mathbf{k}\sigma}(t_2) \equiv \Theta(t_1 - t_2)c_{\mathbf{k}\sigma}(t_1)c^{\dagger}_{\mathbf{k}\sigma}(t_2) - \Theta(t_2 - t_1)c^{\dagger}_{\mathbf{k}\sigma}(t_2)c_{\mathbf{k}\sigma}(t_1), \tag{2.19}$$

where the $-$ sign reflects the anticommutation relation between fermionic operators. For bosonic operators, it will be a $+$ sign. The time dependence of the fermionic operators arises because we are in the interaction picture defined by $\hat{H}$.

[1]The meaning of "density operator" here differs from the usual usage of the term in quantum information theory.

To linear order in $f(t)$, we have the change (in the interaction picture) in the expectation value of $\rho_{\mathbf{q}}(t)$ due to the external perturbation,

$$\delta\langle\rho_{\mathbf{q}}(t)\rangle = \langle\rho_{\mathbf{q}}(t)\rangle - \langle\rho_{\mathbf{q}}(t<0)\rangle = \frac{\mathrm{i}}{\hbar}\int_{-\infty}^{t} \mathrm{d}t^{'}\,\langle\Big[\hat{H}_{\mathrm{ext}}(t^{'}),\rho_{\mathbf{q}}(t)\Big]\rangle. \tag{2.20}$$

Inserting the form of $\hat{H}_{\mathrm{ext}}$, we arrive at the definition of the density response function

$$\delta\langle\rho_{\mathbf{q}}(t)\rangle = \mathcal{V}\int_{-\infty}^{t} \mathrm{d}t^{'}\,\chi_{\mathrm{ret}}(\mathbf{q},t,t^{'})f(t^{'}) \tag{2.21}$$

$$\chi_{\mathrm{ret}}(\mathbf{q},t,t^{'}) = -\frac{\mathrm{i}}{\hbar\mathcal{V}}\Theta(t-t^{'})\langle\Big[\rho_{\mathbf{q}}(t),\rho_{-\mathbf{q}}(t^{'})\Big]\rangle, \tag{2.22}$$

where the Heaviside theta function ensures causality and makes the correlation retarded, and $\mathcal{V}$ is the normalization volume. As we can see, the retarded density response is indeed related to retarded density-density correlations.

Another retarded function that we will need in this thesis is the response function relating to particle creation and annihilation, better known as retarded single-particle Green's function. For fermions, it is defined as [88]

$$G_{\mathrm{ret}}(\mathbf{k}\sigma;t_1,t_2) = -\frac{\mathrm{i}}{\hbar}\Theta(t_1-t_2)\langle\Big\{c_{\mathbf{k}\sigma}(t_1),c^{\dagger}_{\mathbf{k}\sigma}(t_2)\Big\}\rangle \tag{2.23}$$

and for bosons, it is defined as

$$D_{\mathrm{ret}}(\mathbf{q};t_1,t_2) = -\frac{\mathrm{i}}{\hbar}\Theta(t_1-t_2)\langle[A_{\mathbf{q}}(t_1),A_{-\mathbf{q}}(t_2)]\rangle \tag{2.24}$$

$$A_{\mathbf{q}}(t) = \quad b^{\dagger}_{\mathbf{q}} + b_{-\mathbf{q}}, \tag{2.25}$$

where $b_{\mathbf{q}}$ annihilates a boson in momentum mode $\mathbf{q}$, and we have suppressed the polarization index. These single-particle retarded Green's functions can be intuitively interpreted as the single-particle propagators under the Hamiltonian $\hat{H}$. They are central to this formalism. For instance, their imaginary parts give the single-particle spectral functions, which provide information on the thermal occupation of a state. We will return to this point after discussing how they can be calculated.

The computation of the above Green's function is rather complicated when $\hat{H} = \hat{H}_0 + \hat{V}$ includes interactions and is not exactly solvable. Here, $\hat{H}_0$ describes non-interacting particles and is exactly solvable, but $\hat{V}$ describes two-body interactions and can only be treated perturbatively ($\Big[\hat{H}_0,\hat{V}\Big] \neq 0$). In this case, the expansion of the exponential terms (inside the angle bracket denoting thermal averaging) needs to be carried out for both the Boltzmann factor and the time evolution, which is rather

complicated and messy. The remedy for this is the Matsubara formalism, which considers time as an imaginary temperature (such that $it \to \tau$, $\tau \in \mathbb{R}$)[2], such that only exponentials in the form of a Boltzmann factor need to be expanded.

2.2.2 Matsubara single-particle Green's function

Generally, Matsubara Green's functions are defined as

$$\mathcal{C}_{P,Q}(\tau,\tau') = -\frac{1}{\hbar}\langle \mathcal{T}_\tau P(\tau)Q(\tau')\rangle \tag{2.26}$$

for some operators P and Q. $\mathcal{T}_\tau$ means time ordering according to the imaginary time, τ. In this way, the fermionic Matsubara Green's function is defined as [88]

$$G(\mathbf{k}\sigma;\tau) \equiv -\frac{1}{\hbar}\frac{\mathrm{Tr}\left[\mathrm{e}^{-\beta\hat{H}}\mathcal{T}_\tau c_{\mathbf{k}\sigma}(\tau)c^\dagger_{\mathbf{k}\sigma}(0)\right]}{\mathrm{Tr}\left[\mathrm{e}^{-\beta H}\right]} = -\frac{1}{\hbar}\langle \mathcal{T}_\tau c_{\mathbf{k}\sigma}(\tau)c^\dagger_{\mathbf{k}\sigma}(0)\rangle, \tag{2.27}$$

where $c_{\mathbf{k}\sigma}(\tau) = \mathrm{e}^{\tau\hat{H}}c_{\mathbf{k}\sigma}(0)\mathrm{e}^{-\tau\hat{H}}$, and we have used the time-independence of the Hamiltonian, which means the Green's function only depends on the time difference. Using the cyclic property of the trace, we can show that

$$G(\mathbf{k}\sigma;\tau) = -G(\mathbf{k}\sigma;\tau+\beta), \quad \tau < 0. \tag{2.28}$$

This identity means that we can set τ to have domain $-\beta \le \tau \le \beta$ in this formalism, and that the Green's function can be expanded in a Fourier series

$$G(\mathbf{k}\sigma;\mathrm{i}p_n) = \int_0^\beta \mathrm{d}\tau\, \mathrm{e}^{\mathrm{i}\hbar p_n\tau}G(\mathbf{k}\sigma;\tau) \tag{2.29a}$$

$$G(\mathbf{k}\sigma;\tau) = \frac{1}{\beta}\sum_n \mathrm{e}^{-\mathrm{i}\hbar p_n\tau}G(\mathbf{k}\sigma;\mathrm{i}p_n), \tag{2.29b}$$

where $p_n = (2n+1)\pi k_B T/\hbar$, $n \in \mathbb{Z}$ is the fermionic Matsubara frequency.

For a non-interacting system, $\hat{V} = 0$, and $\hat{H}_0 = \sum_{\mathbf{k}\sigma}\xi_{\mathbf{k}\sigma}c^\dagger_{\mathbf{k}\sigma}c_{\mathbf{k}\sigma}$, where $\xi_{\mathbf{k}\sigma} = \epsilon_{\mathbf{k}\sigma} - \mu$ is the dispersion of the fermions measured from chemical potential μ. We have assumed that they are both spin-independent. The non-interacting (or unperturbed) electron Green's function is found using the definition above and the Fermi-Dirac distribution $n_F(\xi) = 1/(\mathrm{e}^{\beta\xi}+1)$ to be [88]

$$G^{(0)}(\mathbf{k}\sigma;\mathrm{i}p_n) = \frac{1}{\mathrm{i}\hbar p_n - \xi_{\mathbf{k}\sigma}}. \tag{2.30}$$

[2]This has no physical meaning, rather, it is a mathematical trick. The usefulness of this trick will be clearer later when we talk about analytic continuation.

The Matsubara Green's function for the (transverse) photons is bosonic in nature. It is defined as

$$D(\mathbf{q};\tau) \equiv -\frac{1}{\hbar}\langle \mathcal{T}_\tau A(\mathbf{q},\tau)A(-\mathbf{q},0)\rangle \tag{2.31}$$

$$A(\mathbf{q},\tau) = \mathrm{e}^{\hat{H}\tau}(b_{\mathbf{q}} + b^\dagger_{-\mathbf{q}})\mathrm{e}^{-\hat{H}\tau}, \tag{2.32}$$

where $b_{\mathbf{q}}$ annihilates a photon in momentum mode $\mathbf{q}$, and we have supressed the polarization index. In a similar way as the electron Green's function, the cyclic property of the trace gives

$$D(\mathbf{q};\tau) = D(\mathbf{q};\tau+\beta), \quad \tau < 0. \tag{2.33}$$

Therefore, the Fourier series expansion for the bosonic Matsubara Green's function is

$$D(\mathbf{q};\mathrm{i}\nu_n) = \int_0^\beta \mathrm{d}\tau\, \mathrm{e}^{\mathrm{i}\hbar\nu_n\tau} D(\mathbf{q};\tau) \tag{2.34a}$$

$$D(\mathbf{q};\tau) = \frac{1}{\beta}\sum_n \mathrm{e}^{-\mathrm{i}\hbar\nu_n\tau} D(\mathbf{q};\mathrm{i}\nu_n) \tag{2.34b}$$

$$\nu_n = 2n\pi k_B T. \tag{2.34c}$$

ν_n is the bosonic Matsubara frequency. Using the Bose-Einstein statistics $n_B(E) = 1/(\mathrm{e}^{\beta E}-1)$, the unperturbed photon Green's function is found to be [88]

$$D^{(0)}(\mathbf{q},\mathrm{i}\nu_n) = -\frac{2\omega_{\mathbf{q}}/\hbar}{\nu_n^2 + \omega_{\mathbf{q}}^2}. \tag{2.35}$$

At this point one might (rightfully) ask: this imaginary time formalism is all well and good, but how is it useful for calculating anything, like the retarded response functions? The answer is that retarded functions can be directly obtained from their corresponding functions of the Matsubara frequencies by simply replacing $\mathrm{i}\nu_n$ in the response function in the Matsubara formalism by $\omega + \mathrm{i}\eta$, where η is infinitesimal; this technique is referred to as analytic continuation [88]. The proof uses the Lehmann representation, which is not particularly useful in calculating physical quantities. For this reason, we do not include the proof here, but we present it in Appendix. A instead. Because it is easier to compute the Matsubara functions for interacting systems (since one only has to expand the exponentials for thermal averaging, rather than for both the thermal averaging and the time evolution if time is not treated as an imaginary temperature), this is a powerful method for finding the corresponding retarded functions.

2.2.3 Interacting systems, higher-order expansions and Feynman diagrams

At this point, we start discussing interacting systems, thus we specify that $\hat{H} = \hat{H}_0 + \hat{V}$. $\hat{H}_0 = \sum_{\mathbf{k}\sigma} \xi_{\mathbf{k}} c^\dagger_{\mathbf{k}\sigma} c_{\mathbf{k}\sigma} + \sum_{\mathbf{q}} \hbar\omega_{\mathbf{q}} b^\dagger_{\mathbf{q}} c_{\mathbf{q}}$ is a single-particle Hamiltonian in which the up and down spins have the same dispersion, and $\hat{V}$ describes interactions. For this thesis, we focus on interactions between the electrons (fermions) and photons (bosons) as well as between electrons (Coulomb repulsion).

As a first example to illustrate the perturbative expansion and Feynman diagrams, let's see how to get a perturbative expansion for the single-particle bosonic Green's function when there are interactions. For simplicity, we ignore Coulomb interactions for now such that

$$\hat{V} = \frac{1}{\sqrt{\mathcal{V}}} \sum_{\mathbf{q}} M_{\mathbf{q}} \rho_{\mathbf{q}} A(\mathbf{q}), \tag{2.36}$$

where $M_{\mathbf{q}}$ is the interaction matrix element for electron-boson coupling. We will, however, discuss Coulomb interactions in the later examples.

To carry out the expansion, it's convenient to be in the interaction picture defined by $\hat{H}_0$. In this picture, the bosonic Green's function is written as

$$D(\mathbf{q};\tau) = \frac{-1}{\hbar\mathcal{Z}} \mathrm{Tr}\left[\mathrm{e}^{-\beta\hat{H}_0}\left(\mathrm{e}^{\beta\hat{H}_0}\mathrm{e}^{-\beta\hat{H}}\right)\mathcal{T}_\tau\left(\mathrm{e}^{\tau\hat{H}}\mathrm{e}^{-\tau\hat{H}_0}\right)\left(\mathrm{e}^{\tau\hat{H}_0}A(\mathbf{q})\mathrm{e}^{-\tau\hat{H}_0}\right)\left(\mathrm{e}^{\tau\hat{H}_0}\mathrm{e}^{-\tau\hat{H}}\right)A(-\mathbf{q})\right] \tag{2.37}$$

$$= -\frac{1}{\hbar}\frac{\mathrm{Tr}\left[\mathrm{e}^{-\beta\hat{H}_0}U(\beta)\mathcal{T}_\tau U^{-1}(\tau)A^I(\mathbf{q},\tau)U(\tau)A^I(-\mathbf{q},0)\right]}{\mathrm{Tr}\left[\mathrm{e}^{-\beta\hat{H}_0}U(\beta)\right]} \tag{2.38}$$

$$= -\frac{1}{\hbar}\frac{\mathrm{Tr}\left[\mathrm{e}^{-\beta\hat{H}_0}\mathcal{T}_\tau U(\beta)A^I(\mathbf{q},\tau)A^I(-\mathbf{q},0)\right]}{\mathrm{Tr}\left[\mathrm{e}^{-\beta\hat{H}_0}U(\beta)\right]} \tag{2.39}$$

$$\equiv -\frac{1}{\hbar}\frac{\langle\mathcal{T}_\tau U(\beta)A^I(\mathbf{q},\tau)A^I(-\mathbf{q},0)\rangle_0}{\langle U(\beta)\rangle_0}. \tag{2.40}$$

We have used the superscript "I" to distinguish the operator in this interaction picture. The subscript "0" of the angle bracket indicates that the thermal averaging is done with respect to $\hat{H}_0$. U satisfies

$$\frac{\partial}{\partial\tau}U(\tau) = \mathrm{e}^{\tau\hat{H}_0}\left(\hat{H}_0 - \hat{H}\right)\mathrm{e}^{-\tau\hat{H}} = -\mathrm{e}^{\tau\hat{H}_0}\hat{V}\mathrm{e}^{-\tau\hat{H}} = -\hat{V}^I(\tau)U(\tau). \tag{2.41}$$

Therefore,

$$U(\tau) = 1 - \int_0^\tau \mathrm{d}\tau_1 \, \hat{V}^I(\tau_1) U(\tau_1) \tag{2.42}$$

$$= 1 - \int_0^\tau \mathrm{d}\tau_1 \, \hat{V}^I(\tau_1) + \int_0^\tau \mathrm{d}\tau_1 \int_0^{\tau_1} \mathrm{d}\tau_2 \, \hat{V}^I(\tau_1)\hat{V}^I(\tau_2) + \dots \tag{2.43}$$

Substituting Eq. (2.43) into Eq. (2.39), we get the expansions for the perturbed single-particle Matsubara Green's function for the boson. For the numerator

$$\begin{aligned}
&\langle \mathcal{T}_\tau U(\beta) A^I(\mathbf{q},\tau) A^I(-\mathbf{q},0)\rangle_0 \\
&= \sum_{n=0}^{\infty} \frac{(-1)^n}{n!} \int_0^\beta \mathrm{d}\tau_1 \cdots \int_0^\beta \mathrm{d}\tau_n \, \langle \mathcal{T}_\tau A^I(\mathbf{q},\tau) \hat{V}^I(\tau_1) \cdots \hat{V}^I(\tau_n) A^I(-\mathbf{q},0)\rangle_0,
\end{aligned} \tag{2.44}$$

and for the denominator

$$\langle \mathcal{T}_\tau U(\beta)\rangle_0 = \sum_{n=0}^{\infty} \frac{(-1)^n}{n!} \int_0^\beta \mathrm{d}\tau_1 \cdots \int_0^\beta \mathrm{d}\tau_n \, \langle \mathcal{T}_\tau \hat{V}^I(\tau_1) \cdots \hat{V}^I(\tau_n)\rangle_0. \tag{2.45}$$

Each term inside $\langle\rangle_0$ is evaluated by applying Wick's theorem [88]. For example, in the numerator, the second order term is

$$\begin{aligned}
&\langle \mathcal{T}_\tau A^I(\mathbf{q},\tau) \hat{V}^I(\tau_1) \hat{V}^I(\tau_2) A^I(-\mathbf{q},0)\rangle_0 \\
&= \sum_{\mathbf{k}_1,\sigma_1,\mathbf{k}_2,\sigma_2,\mathbf{q}_1,\mathbf{q}_2} \frac{M_{\mathbf{q}_1} M_{\mathbf{q}_2}}{\mathcal{V}} \langle \mathcal{T}_\tau A^I(\mathbf{q},\tau) A^I(\mathbf{q}_1,\tau_1) A^I(\mathbf{q}_2,\tau_2) A^I(-\mathbf{q},0)\rangle_0 \\
&\quad \times \langle \mathcal{T}_\tau c^\dagger_{\mathbf{k}_1+\mathbf{q}_1\sigma_1}(\tau_1) c_{\mathbf{k}_1\sigma_1}(\tau_1) c^\dagger_{\mathbf{k}_2+\mathbf{q}_2\sigma_2}(\tau_2) c_{\mathbf{k}_2\sigma_2}(\tau_2)\rangle_0,
\end{aligned} \tag{2.46}$$

and we apply Wick's theorem to the first angle bracket to get

$$\begin{aligned}
&\langle \mathcal{T}_\tau A^I(\mathbf{q},\tau) A^I(\mathbf{q}_1,\tau_1) A^I(\mathbf{q}_2,\tau_2) A^I(-\mathbf{q},0)\rangle_0 \\
=&\langle \mathcal{T}_\tau A^I(\mathbf{q},\tau) A^I(\mathbf{q}_1,\tau_1)\rangle_0 \langle \mathcal{T}_\tau A^I(\mathbf{q}_2,\tau_2) A^I(-\mathbf{q},0)\rangle_0 \\
&+ \langle \mathcal{T}_\tau A^I(\mathbf{q},\tau) A^I(\mathbf{q}_2,\tau_2)\rangle_0 + \langle \mathcal{T}_\tau A^I(\mathbf{q}_1,\tau_1) A^I(-\mathbf{q},0)\rangle_0 \\
&+ \langle \mathcal{T}_\tau A^I(\mathbf{q},\tau) A^I(-\mathbf{q},0)\rangle_0 \langle \mathcal{T}_\tau A^I(\mathbf{q}_1,\tau_1) A^I(\mathbf{q}_2,\tau_2)\rangle_0
\end{aligned} \tag{2.47}$$

$$\begin{aligned}
=&D^{(0)}(\mathbf{q},\tau-\tau_1) D^{(0)}(\mathbf{q},\tau_2) \delta_{\mathbf{q},-\mathbf{q}_1} \delta_{\mathbf{q},\mathbf{q}_2} + D^{(0)}(\mathbf{q},\tau-\tau_2) D^{(0)}(\mathbf{q},\tau_1) \delta_{\mathbf{q},-\mathbf{q}_2} \delta_{\mathbf{q},\mathbf{q}_1} \\
&+ D^{(0)}(\mathbf{q},\tau) D^{(0)}(\mathbf{q}_1,\tau_1-\tau_2) \delta_{\mathbf{q}_1,-\mathbf{q}_2},
\end{aligned} \tag{2.48}$$

and we do the same for the second angle bracket to get

$$\begin{aligned}
&\langle \mathcal{T}_\tau c^\dagger_{\mathbf{k}_1+\mathbf{q}_1\sigma_1}(\tau_1) c_{\mathbf{k}_1\sigma_1}(\tau_1) c^\dagger_{\mathbf{k}_2+\mathbf{q}_2\sigma_2}(\tau_2) c_{\mathbf{k}_2\sigma_2}(\tau_2)\rangle_0 \\
=&n_{\mathbf{k}_1\sigma_1}(\tau_1) n_{\mathbf{k}_2\sigma_2}(\tau_2) \delta_{\mathbf{q}_2,0} \delta_{\mathbf{q}_1,0} \\
&- G^{(0)}(\mathbf{k}_1+\mathbf{q}_1\sigma_1,\tau_2-\tau_1) G^{(0)}(\mathbf{k}_1\sigma_1,\tau_1) \delta_{\sigma_1,\sigma_2} \delta_{\mathbf{k}_1,\mathbf{k}_2+\mathbf{q}_2} \delta_{\mathbf{q}_1,-\mathbf{q}_2}.
\end{aligned} \tag{2.49}$$

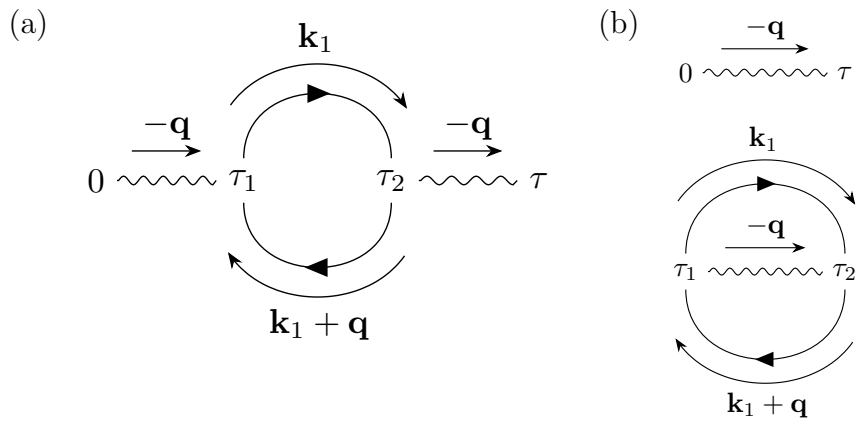


Figure 2.1: Examples of Feynman diagrams for second order corrections to the bosonic Green's function. (a) depicts a connected diagram, whereas (b) depicts a disconnected diagram.

We see that the perturbed single-particle Green's function is expressed as an expansion in terms of unperturbed single-particle Green's functions, which we know exactly. More specifically, the higher order terms (correlators) from the expansions of the numerator and the denominator in Eq. (2.40) are broken down into products of unperturbed single-particle Green's functions.

These products can be more straightforwardly visualised with the help of diagrams. For instance, the product between the second term from Eq. (2.48) and the second term from Eq. (2.49) gives the diagram in Fig. 2.1(a), where the zigzag lines represent unperturbed bosonic Green's functions, the solid lines represent unperturbed fermionic Green's functions, the labels for the imaginary time are at the nodes, and the arrows represent direction of imaginary time propagation. We read this diagram from left to right, following the direction of imaginary time. At first, we have a bosonic excitation in momentum mode $-\mathbf{q}$. Due to interactions between the fermions and the bosonic mode, the bosonic excitation causes a particle-hole excitation at τ_1, which then recombines at later imaginary time τ_2 to return the bosonic excitation.

Diagrams like Fig. 2.1(a) are called *connected* diagrams, in contrast to, e.g., Fig. 2.1(b), a *disconnected* diagram which represents the product between the third term from Eq. (2.48) and the second term from Eq. (2.49). We do not need to include disconnected diagrams in calculations because they are cancelled out by the denominator $\langle \mathcal{T}_\tau U(\beta) \rangle_0$. This fact is referred to as linked-cluster theorem [88].

We will now work in Matsubara frequency space so that we can use analytic continuation to get retarded correlations in the end. Thus, using Eq. (2.29) and

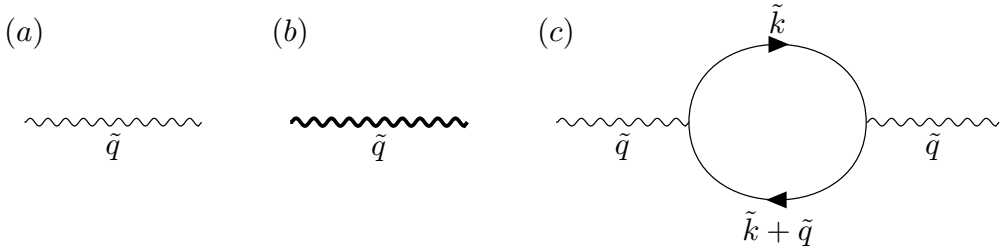


Figure 2.2: Feynman diagram notations for Green's functions. (a) Unperturbed bosonic Green's functions. (b) Perturbed bosonic Green's functions. (c) First correction to the unperturbed bosonic Green's functions in a system of interacting fermions and bosons.

(2.34), we get the expansion in Matsubara frequency space

$$D(\mathbf{q}, \mathrm{i}\nu_n) = D^{(0)}(\mathbf{q}, \mathrm{i}\nu_n) + D^{(0)}(\mathbf{q}, \mathrm{i}\nu_n) \left(\frac{M_{\mathbf{q}}^2}{\beta \mathcal{V}} \sum_{\mathbf{k},\sigma,\mathrm{i}p_n} G^{(0)}(\mathbf{k}+\mathbf{q}\sigma, \mathrm{i}p_n + \mathrm{i}\nu_n) G^{(0)}(\mathbf{k}\sigma, \mathrm{i}p_n) \right) D^{(0)}(\mathbf{q}, \mathrm{i}\nu_n) + \ldots \tag{2.50}$$

Terms in this series can be formally collected together (it is like summing a geometric series) into the Dyson equation [88],

$$D(\mathbf{q}, \mathrm{i}\nu_n) = \frac{D^{(0)}(\mathbf{q}, \mathrm{i}\nu_n)}{1 - D^{(0)}(\mathbf{q}, \mathrm{i}\nu_n)\Pi(\mathbf{q}, \mathrm{i}\nu_n)}, \tag{2.51}$$

where Π denotes the self-energy of the bosons, which becomes more significant with increasing boson-fermion interaction strength. The leading order term of the self-energy is given by the expression inside the large bracket in Eq. (2.50); we can interpret it as a second order correction to the energy of the bosonic excitation due to interactions with the electrons.

In order to avoid large clusters of equations like we have seen above, we use Feynman diagrams whenever possible. For the rest of the thesis, we use thin zigzag lines to represent unperturbed bosonic Green's functions, like in Fig. 2.2(a), thick zigzag lines to represent bosonic Green's functions of the perturbed system, like in Fig. 2.2(b), and thin solid lines with arrows for unperturbed electron Green's functions. We also use the 4-vector representation, $\tilde{q} \equiv (\mathbf{q}, \mathrm{i}\nu_n)$, for ease of notation.

It is, in general, impossible to compute the series expansions like Eq. (2.50) exactly. However, one commonly uses an approximation called the *random-phase approximation* (RPA), which includes diagrams from all orders in the infinite series that we

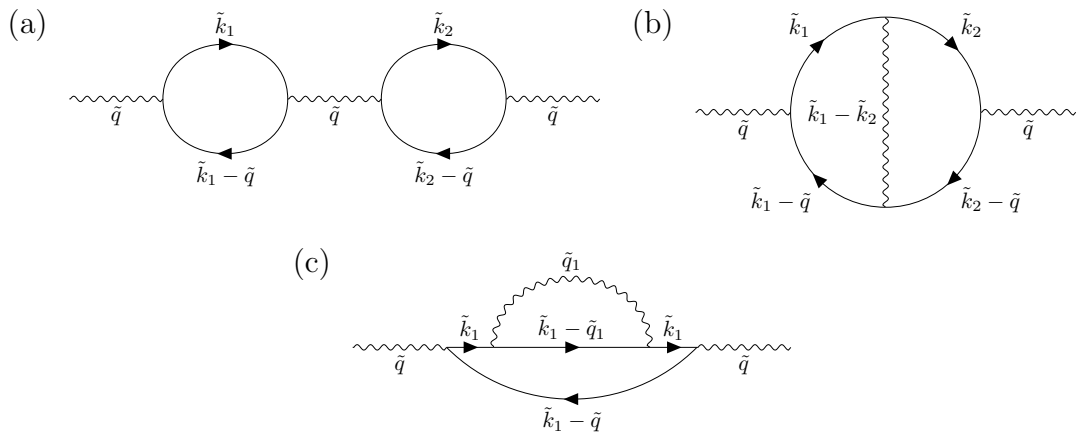


Figure 2.3: Second correction to the unperturbed bosonic Green's functions in the system of interacting fermions and bosons.

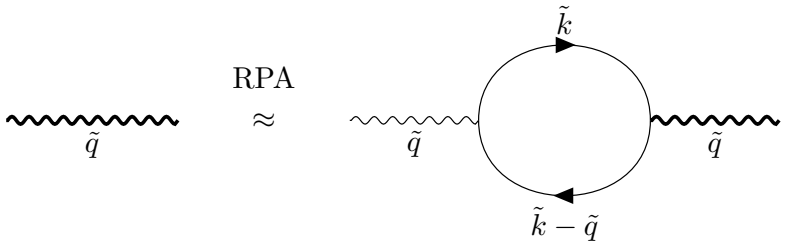


Figure 2.4: Representation of the Dyson equation for bosonic Green's functions under the random-phase approximation.

get from perturbative expansion. This approximation corresponds to summing only the diagrams involving simple "bubbles", such as Fig. 2.2(c) and Fig. 2.3(a), but not crossed bubbles, such as Fig. 2.3(b) and (c). The physical interpretation of this approximation is that the dynamic potential due to fermions' response averages out for all modes other than $\tilde{q}$.

Relating it to the Dyson equation Eq. (2.51), RPA means replacing Π with its leading order term, which is expressed inside the large bracket in Eq. (2.50). The Feynman diagram visualisation of this is shown in Fig. 2.4.

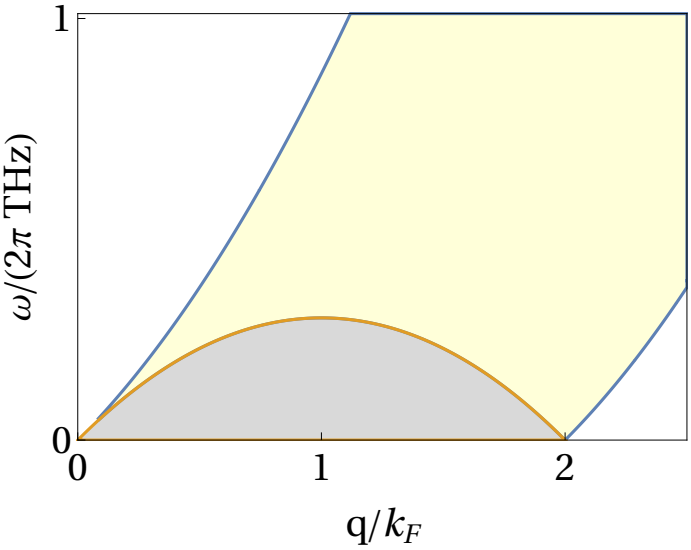


Figure 2.5: Phase space diagram. Inside the colored area, the electron polarizability χ_0 is complex. The yellow area denotes the region where only particle excitations are possible, whereas in the gray area both particle and hole excitations are possible. We used electron density $n_e = 10^{12}$ cm^{-2}, and the electron effective mass equals twice the bare electron mass for this plot.

Under this approximation we have

$$D(\mathbf{q}, \mathrm{i}\nu_n) = \frac{D^{(0)}(\mathbf{q}, \mathrm{i}\nu_n)}{1 - M_{\mathbf{q}}^2 D^{(0)}(\mathbf{q}, \mathrm{i}\nu_n)\chi_0(\mathbf{q}, \mathrm{i}\nu_n)}, \text{ where} \tag{2.52}$$

$$\begin{aligned}\chi_0(\mathbf{q}, \mathrm{i}\nu_n) =& \frac{1}{\beta\mathcal{V}} \sum_{\mathbf{k},\sigma,\mathrm{i}p_n} G^{(0)}(\mathbf{k}+\mathbf{q}\sigma, \mathrm{i}p_n + \mathrm{i}\nu_n) G^{(0)}(\mathbf{k}\sigma, \mathrm{i}p_n) \\ =& \frac{2}{\mathcal{V}} \sum_{\mathbf{k}} \frac{n_F(\xi_{\mathbf{k}}) - n_F(\xi_{\mathbf{k}+\mathbf{q}})}{\mathrm{i}\hbar\nu_n + \xi_{\mathbf{k}} - \xi_{\mathbf{k}+\mathbf{q}}}.\end{aligned} \tag{2.53}$$

χ_0 is the simple bubble depicted in Fig. 2.2(c). We can get the density response function defined in Eq. (2.22) by analytic continuation of $\chi_0(\mathbf{q}, \mathrm{i}\nu_n \to \omega + \mathrm{i}\eta)$, followed by a Fourier transform into the real time domain. From Eq. (2.53), we see that $\chi_0(\mathbf{q}, \omega)$ (the retarded electron polarizability) is a complex quantity when $\hbar\omega = \xi_{\mathbf{k}+\mathbf{q}} - \xi_{\mathbf{k}}$ for some $\mathbf{k}$. Physically, this condition means that the phase space coordinate $(\mathbf{q}, \omega)$ is inside the single-particle excitation continuum (i.e., particle-hole excitations are possible), which is shown as the colored areas in Fig. 2.5.

Expressions for the simple bubble, χ_0, of electron gases have been found in the low temperature limit (where the Fermi-Dirac distribution is approximately a step function) for 3D [87] as well as for 2D [89]. Since this thesis concerns 2D systems, here we only quote the 2D electron gas polarizability result from Refs. [90, 89], which

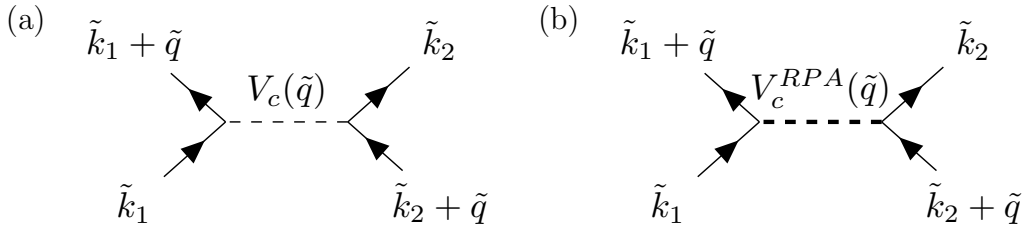


Figure 2.6: Feynman diagrams showing electrons interacting via the (a) bare and (b) RPA screened Coulomb interactions.

we will use in Chapter. 3,

$$\mathrm{Re}\{\chi_0(q,\hbar\omega)\} = \frac{k_F^2 r_\omega}{\hbar\omega\pi}[-2r_q + C_-\sqrt{(r_q - r_\omega)^2 - 1} + C_+\sqrt{(r_q + r_\omega)^2 - 1}] \quad (2.54a)$$

$$\mathrm{Im}\{\chi_0(q,\hbar\omega)\} = \frac{k_F^2 r_\omega}{\hbar\omega\pi}[D_-\sqrt{1 - (r_q - r_\omega)^2} - D_+\sqrt{1 - (r_q + r_\omega)^2}], \quad (2.54b)$$

where $r_q = \frac{q}{2k_F}$, $r_\omega = \frac{\omega}{qv_F}$, $C_\pm = \mathrm{sign}(r_q \pm r_\omega)$ and $D_\pm = 0$ for $|r_q \pm r_\omega| > 1$, and $C_\pm = 0$ and $D_\pm = 1$ for $|r_q \pm r_\omega| < 1$.

In the following, we present two examples utilising this formalism. First, we discuss the screening of interactions between electrons, taking Coulomb interactions as the example. Second, we discuss the spectral function and how to calculate the occupation of a bosonic mode.

2.2.3.1 Example: Coulomb interactions and plasma resonance

Having demonstrated the Matsubara Green's function formalism, Feynman diagrams, the random-phase approximation, and their application to a system of interacting electrons and bosons, it is now straightforward to modify them to address the classic problem of screened Coulomb interactions.

In Coulomb gauge, the bare Coulomb interactions are treated as being instantaneous. This can be seen in the form of the interaction potential $V_c(\mathbf{q})$, which has no dependence on (Matsubara) frequency: for electrons in 3D materials, $V_c(\mathbf{q}) = e^2/\epsilon_0\epsilon_r q^2$, while in 2D, $V_c(\mathbf{q}) = e^2/2\epsilon_0\epsilon_r q$. Here $q = |\mathbf{q}|$. However, the screened Coulomb interactions are dynamic and retarded because the electron response to changes of the electric potential is a dynamic and retarded process. Thus, we expect the screened Coulomb interactions to have (Matsubara) frequency dependence.

To obtain the expression for the screened Coulomb interactions, we recognise that the Coulomb interactions are bosonic in nature, as they involve an even number of fermionic operators. This way, they can be treated like bosonic Green's functions.

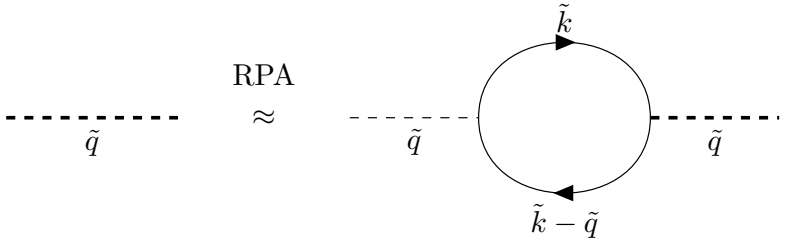


Figure 2.7: Representation of the Dyson equation for screened Coulomb interaction under the random-phase approximation.

This means that all the formalism of a system of interacting electrons (also called jellium) is the same as the one we presented earlier once we replace $M_{\mathbf{q}}^2 D^{(0)}(\mathbf{q}, \mathrm{i}\nu_n)$ with $V_c(\mathbf{q})$, which is the matrix element for bare Coulomb interaction in momentum space, see Fig. 2.6(a). The screened Coulomb interaction matrix within RPA [see Fig. 2.6(b)] is thus [88],

$$V_c^{\mathrm{RPA}}(\mathbf{q}, \mathrm{i}\nu_n) = \frac{V_c(\mathbf{q})}{1 - V_c(\mathbf{q})\chi_0(\mathbf{q}, \mathrm{i}\nu_n)}, \tag{2.55}$$

which has a pictorial representation (Fig. 2.7) which is analogous to Fig. 2.4.

In this example, we consider a 2D electron gas and focus on the region of phase space with small momentum and look into both the static and high frequency limits using the results in Eq. (2.54).

In the static limit, $\chi_0 = k_F/\hbar\pi$ is a real constant. After substitution into Eq. (2.55), we get that $V_c^{\mathrm{RPA}}(\mathbf{q}, 0) \propto 1/(q + q_{\mathrm{TF}})$, where $q_{\mathrm{TF}} = e^2 k_F/2\hbar\epsilon_0\epsilon_r v_F$ is the Thomas-Fermi wavevector [88]. This ensures the static screened Coulomb interactions is short-range, and has a length scale set by q_{TF}.

In the high frequency limit, for sufficiently small momenta, χ_0 is a real quantity and

$$\mathrm{Re}\{\chi_0\} = \frac{k_F^2 r_\omega}{\hbar\omega\pi}\left(-2r_q + \sqrt{(r_q + r_\omega)^2 - 1} - \sqrt{(r_q - r_\omega)^2 - 1}\right) \tag{2.56}$$

$$\approx \frac{k_F^2 r_\omega}{\hbar\omega\pi}\frac{r_q}{r_\omega^2 - r_q^2} \approx \frac{k_F^2 r_q}{\hbar\omega\pi r_\omega} = \frac{k_F v_F q^2}{\hbar\omega^2 2\pi}. \tag{2.57}$$

χ_0's dependence on q and ω means that the electron gas reacts less to density perturbations of higher frequencies and longer wavelengths. Intuitively, this means that the electron gas is too slow to react to potentials that change too fast.

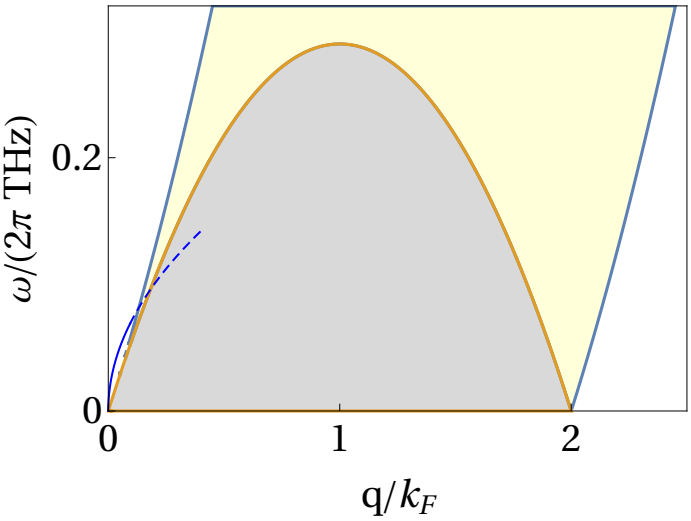


Figure 2.8: Phase space diagram. The blue line represent the 2D plasmon dispersion given in Eq. (2.57). The dashed part indicates that the dispersion enters into the single-particle excitation continuum, where the plasma oscillations are Laudau damped [88]. We used an artificial number for relative permittivity $\epsilon_r = 10^3$ in order to make the small momentum behaviour of the plasmon dispersion curve more visible.

Using Eq. (2.57), we get

$$V_c^{\mathrm{RPA}}(\mathbf{q},\omega) \approx \frac{V_c(\mathbf{q})}{1-\frac{\omega_{\mathrm{pl}}^2}{\omega^2}}, \text{ where} \tag{2.58}$$

$$\omega_{\mathrm{pl}}^2(\mathbf{q}) = \frac{e^2}{4\pi\hbar\epsilon_0 c}\frac{k_F v_F q c}{\epsilon_r} = \alpha\frac{k_F v_F q c}{\epsilon_r} \tag{2.59}$$

gives the plasma resonance of the 2D electron system. Plasma are electron density fluctuations, thus they can be excited by coupling to electromagnetic radiations; Hamiltonian terms such as Eq. (2.13) excites plasma oscillations. The denominator in Eq. (2.58) has the same form as in the Drude model [1]. In Eq. (2.59), α is the fine-structure constant. We see that in 2D, the plasma resonance scales with $\sqrt{q}$ for small q, rather than being a constant as is the case in 3D. We plot the plasmon dispersion in Fig. 2.8. For larger q, the plasma oscillations are Landau damped by single-particle excitations [88].

2.2.3.2 Spectral function

Another important quantity one can get out of Matsubara Green's function formalism is the spectral function, which is given by the imaginary part of a retarded Green's

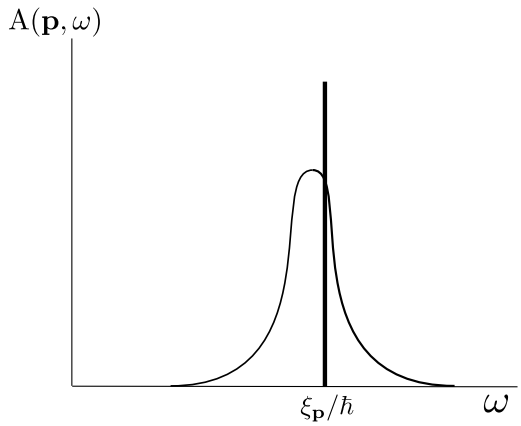


Figure 2.9: A sketch of single electron spectral functions. The thick vertical line denotes a delta peak and corresponds to a non-interacting electron. The thin curve is for an interacting electron; it shows that the spectrum is broadened by the interactions.

function [88],

$$\mathrm{A}(\mathbf{p},\omega) = -\,2 * \mathrm{Im}\{G_{\mathrm{ret}}(\mathbf{p},\omega)\} \tag{2.60a}$$

$$\mathrm{B}(\mathbf{q},\omega) = -\,2 * \mathrm{Im}\{D_{\mathrm{ret}}(\mathbf{q},\omega)\}, \tag{2.60b}$$

where A and B are the spectral functions for electrons and bosons respectively.

It is best to demonstrate how they are useful by looking at an example. Let's consider the unperturbed electron Green's function $G^{(0)}_{\mathrm{ret}}(\mathbf{p},\omega) = 1/(\hbar\omega - \xi_{\mathbf{p}} + \mathrm{i}\eta)$, in this case

$$\mathrm{A}^{(0)}(\mathbf{p},\omega) = 2\pi\ \delta(\hbar\omega - \xi_{\mathbf{p}}), \tag{2.61}$$

i.e., it is a delta function peaked at the energy of the unperturbed electron state, indicating the state is well-defined and not decaying. This is shown in Fig. 2.9. When interactions are switched on, there is a contribution from the self-energy, which as we have seen in the case for bosons, can also gain an imaginary part. Qualitatively speaking, the real part of the self-energy shifts the peak of the spectrum (i.e., alters the excitation's dispersion), while the imaginary part broadens the spectrum (i.e., reduces the excitation's lifetime). We show this in Fig. 2.9.

For the unperturbed Green's function, it is easy to see that

$$1 = \int_{\infty}^{\infty} \frac{\hbar\,\mathrm{d}\omega}{2\pi} \mathrm{A}^{(0)}(\mathbf{p},\omega), \text{ and} \tag{2.62}$$

$$n_{\mathbf{p}} = \int_{\infty}^{\infty} \frac{\hbar\,\mathrm{d}\omega}{2\pi} n_F(\hbar\omega)\mathrm{A}^{(0)}(\mathbf{p},\omega). \tag{2.63}$$

These relations are also true for interacting electrons (substituting $\mathrm{A}^{(0)}$ with A). The proof uses the Lehmann representation described in Appendix. A, and can be found in Ref. [88].

Analogous to electrons, the bosonic mode occupation, $N_{\mathbf{q}}$, is given by integrating the bosonic spectral function multiplied by the Bose-Einstein distribution, $n_B(E) = (\exp\{\beta E\} - 1)^{-1}$ [88],

$$2N_{\mathbf{q}} + 1 = \int_{\infty}^{\infty} \frac{\hbar \, \mathrm{d}\omega}{2\pi} n_B(\hbar\omega) \mathrm{B}(\mathbf{q}, \omega). \tag{2.64}$$

This can be easily verified for non-interacting bosons, which have spectral function

$$\mathrm{B}^{(0)}(\mathbf{q}, \omega) = 2\pi[\delta(\hbar\omega - \hbar\omega_{\mathbf{q}}) - \delta(\hbar\omega + \hbar\omega_{\mathbf{q}})]. \tag{2.65}$$

Notice that the bosonic spectral functions are always positive for $\omega > 0$ and negative for $\omega < 0$.

2.3 Conclusion

In this chapter, we have derived a general Hamiltonian describing a system of interacting electrons and light modes (both classical and quantum). We have also introduced the Matsubara Green's function formalism and Feynman diagrams for describing an interacting systems, and shown how these Green's functions (or correlators) relate to physical quantities such as density responses and mode occupation numbers. In addition, we have explained how the random-phase approximation is used to carry out calculations within this formalism. In the next chapter, we apply the techniques covered in this chapter to study a system of weakly interacting 2D electrons coupled to a driven cavity.

Chapter 3

Photoinduced electron pairing in a driven cavity

Most of the results presented in this chapter were published as H. Gao, F. Schlawin, M. Buzzi, A. Cavalleri, and D. Jaksch, Photoinduced Electron Pairing in a Driven Cavity, *Phys. Rev. Lett.* **125**, 053602 (2020). HG performed all the calculations apart from the results regarding substrate heating, which was obtained by M. Buzzi, who wrote that section for the publication (this section is presented in Appendix. B). HG also made substantial contributions to the manuscript.

In the previous chapter, we derived a general light-matter Hamiltonian which includes both a classical light field, which describes the light from a laser, and quantum light fields which describe the vacua. We also introduced the Green's function method, which is useful for calculating properties of quantum many-body systems.

We are now in the position to present the first major set of results of this thesis, which contributes to the ongoing effort to achieve quantum materials on demand [91].

In this chapter, we study a system in which a two-dimensional solid state material is coupled to the quantum lights of a terahertz cavity as well as a strong classical driving. The system considered here is partly inspired by Ref. [70], in which a 2D electron gas is coupled to an empty cavity. In Ref. [70], the cavity mediates current-current interactions between the electrons due to paramagnetic coupling between the cavity field and the electrons. The cavity-mediated interactions could lead to Amperean pairing at observable temperatures. A significant drawback of the proposal of Ref. [70] is the lack of external dynamical experimental controllability of the properties of the interaction potential. In our setup, in contrast, the additional adjustable external driving combined with the cavity's shaped vacuum fluctuations enable us to create a novel type of controllable long-range density-density electron interactions in 2D materials. Importantly, these interactions are manipulated by the parameters

of the driving laser: their strength is proportional to the laser intensity I_d and inversely proportional to the detuning $\delta_c = \omega_c - \omega_L$ (ω_c is the cavity frequency and ω_L is the driving frequency), which allows us to tune them to be attractive or repulsive by changing δ_c. Intuitively they can be thought of as the result of inelastic scattering processes in which the intermediate state is dressed by the cavity. Strong coherent driving is essential to ensure that the two-photon diamagnetic scattering from which the interactions arise dominates over other (one-photon paramagnetic) processes, while the strong coupling to the cavity field is needed to enhance these interactions but not laser-induced heating processes. Another advantage of interactions arising from two-photon diamagnetic processes is that they can be induced in a wide range of materials. Here, we consider a 2D electron gas as a prototypical system. We use parameters consistent with semiconductor quantum wells, gated bilayer graphene (BLG) [92] and the interface between lanthanum aluminate and strontium titanate (LAO/STO) [93] in the normal phase. The latter two are tunable 2D electron gases that can be adjusted arbitrarily close to a spontaneous superconducting instability and exhibit correlated electron phenomena, potentially making the physics even richer. Using these examples, we show that the interactions are long-ranged and not effectively screened by the electrons. In the attractive regime, we find that they induce an instability in the Cooper channel at experimentally observable temperatures.

Our results provide a novel route for engineering electron interactions in a wide range of two-dimensional materials. Later, in Chapter. 5, we discuss a possible application of this scheme to a BCS superconductor.

3.1 Setup

We consider the setup shown in Fig. 3.1(a). A 2D electron system lies in the xy-plane inside a substrate material with relative permittivity ϵ_r. It is coupled to the evanescent field of a complementary split-ring cavity which sits on top of the substrate material, as e.g. in Ref. [49]. This type of cavity is well described by a single-mode light field[1] and has been reported to exhibit strong vacuum fluctuations [94] due to its small cavity mode volume, $\mathcal{V}_c = \Lambda\lambda^3$, where λ is the wavelength of the light mode in the substrate material, and Λ is the mode volume compression factor. Values of $\Lambda = 2.5/8\times10^{-5}$ or even smaller have been reached in experiments and simulations [49, 95], and the narrower the gap in the split-ring, the stronger the mode volume compression.

[1]The next higher mode has a frequency of roughly $4\omega_c$ and is more lossy [49].

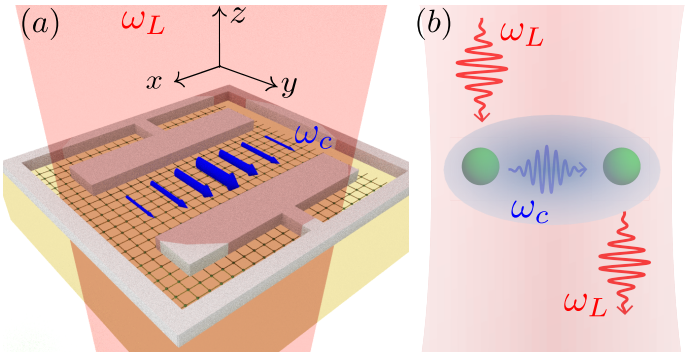


Figure 3.1: (a) Setup: a 2D material (indicated by the square lattice) on a substrate (yellow) is coupled to a complementary split-ring cavity (gray) [49], whose electric field is represented by the blue arrows with thickness proportional to the field strength. The coupled system is driven by a laser field (schematically shown by the red shading) with wavevector $\mathbf{q}_L \parallel z$-axis and frequency ω_L detuned from the cavity frequency ω_c. (b) The mechanism of inducing interactions between two electrons (green spheres). Laser(cavity) photons are represented by red(blue) wavy arrows and the green balls are electrons. The red(blue) shading symbolizes the laser(cavity) field.

The strong mode volume compression can leads to ultrastrong coupling between two-dimensional electron gas's cyclotron transitions and vacuum field fluctuation, where the Rabi frequency is a significant fraction of the transition frequency [49]. We note that due to the small sizes of available bilayer graphene samples, LAO/STO may be more straightforwardly integrated into a cavity that extends several hundred microns in size. Furthermore, because LAO/STO structures are insulating at frequencies above the plasma frequency, dissipation may be managed better in these systems than in the graphene structures.

For simplicity, we thus model the cavity as supporting a single mode with resonance frequency ω_c. While in principle one can choose whichever gauge to carry out the calculations, we work in the Coulomb gauge (like in the previous chapter), which is arguably the most conventional and convenient choice for studying condensed matter systems. This gauge choice provides a clearer description of the main process of interest. It is most likely to be appropriate for calculations for our scheme thanks to the off-resonance nature of the energy levels involved, though a more thorough investigation of the effect of gauge choice should be carried out in the future. In this gauge, the cavity field is described by a vector potential $\mathbf{A}_c(\mathbf{r}) = 2\mathbf{e}_y\sqrt{\hbar/\mathcal{V}_c\epsilon_0\epsilon_r\omega_c}\cos(q_0 x)\left(b + b^\dagger\right)$, where $\mathbf{e}_y$ is the unit vector in y-direction, $q_0 = \omega_c\sqrt{\epsilon_r}/c$ with c the speed of light in vacuum, ϵ_0 the vacuum permittivity and b the bosonic annihilation operator for the cavity photon. We further require the cavity linewidth to be small compared to the

detuning between the cavity resonance and the driving frequency discussed below.

The cavity-matter system is driven by a strong laser that we describe by an oscillating classical field with vector potential $\mathbf{A}_d(t) \propto \mathbf{e}_y\sqrt{I_\mathrm{d}}\sin(|\mathbf{q}_L|z - \omega_L t)$, where $\mathbf{q}_L$ is the laser photon wavevector and t is the time. The laser frequency $\omega_L = \omega_c - \delta_c$ is out-of-resonance from the cavity. The propagation direction of the laser mode is perpendicular to the cavity mode, akin to transversally pumped-cavity-setups with cold atoms [96]. This way the driving field interacts directly with the electronic system and not directly with the cavity mode.

3.2 The light-matter interaction Hamiltonian in Coulomb gauge

It is clear that the cavity modes are only a small fraction of all the light modes inside the periodic box of 3D space we used to define the light modes. Most of the other modes don't 'see' the cavity as they are of different frequencies from the cavity modes or they are travelling at such large angles from cavity axis. We treat them as the environment modes. We use complex mode functions $\mathbf{u}_{q_e\equiv\{\mathbf{q}_e,s\}}$ (with $\mathbf{u}^*_{q_e} = \mathbf{u}_{-q_e}$) that describe travelling plane waves for the environment modes whose indices can be interpreted as momentum ($\mathbf{q}_e$) and polarization labels (s) for the modes. In Sec. 3.3.3, we verify that for the parameters we consider their main influence—inelastic scattering of laser photons into the environment—does not heat the electrons significantly. Thus, we do not include these environment modes into our system Hamiltonian from now on.

We substitute the vector potentials of the cavity and the driving fields described above into Eq. (2.12) to obtain the Hamiltonian

$$H = \sum_j \frac{[\boldsymbol{p}_j + e\mathbf{A}_{\mathrm{tot}}(\boldsymbol{r}_j, t)]^2}{2m} + V_{bg}(\boldsymbol{r}_j) + H_{Coul} + H_{cav} \tag{3.1}$$

with $\mathbf{A}_{\mathrm{tot}}(\boldsymbol{r}_j, t) = \mathbf{A}_c(\boldsymbol{r}_j) + \mathbf{A}_d(\boldsymbol{r}_j, t)$. Just to recap, here $\boldsymbol{p}_j$ and $\boldsymbol{r}_j$ are the momentum and position operators of electron j with bare mass m, V_{bg} is the static potential due to the positive background, $H_{Coul} = 1/2 \sum_{j\neq k,\ j,k\in e^-} e^2/\left(4\pi\epsilon_0\epsilon_r|\boldsymbol{r}_j - \boldsymbol{r}_k|\right)$ is the Coulomb interaction between the electrons and $H_{cav} = \hbar\omega_c b^\dagger b$ is the unperturbed cavity Hamiltonian. We assume that the single-electron physics arising from the first part of the Hamiltonian [Eq. (3.1)] is described by a single band, and higher bands are far detuned from the driving and the cavity frequencies considered here ($\lesssim$

10 THz) such that dynamical Stark effects are negligible.

In the next section, we discuss the various interactions between the electrons and the transverse fields and identify the diamagnetic interactions involving both the cavity and the driving modes as the most dominant.

3.3 Light-matter interaction

In this section, we discuss the different interactions between the electrons, the cavity and the laser light modes. we proceed to consider the light-matter interactions without the environment modes. We justify this in Sec. 3.3.3, where we discuss the inelastic scattering of the laser photons into the environment modes. The scattering heats the electrons but the effect is insignificant due to the small detuning to cavity frequency ratio and the strong cavity mode volume compression.

By expanding out Eq. (3.1), we obtain the different transverse light field-matter interactions: paramagnetic interactions,

$$H_{para-c} = \sum_{j\in e^-} \frac{e}{m}\boldsymbol{p}_j \cdot \hat{\boldsymbol{e}}_y \sqrt{\frac{\hbar}{\mathcal{V}_c\epsilon_0\epsilon_r\omega_c}} 2\cos(q_0 x_j)\left(b + b^\dagger\right) \tag{3.2}$$

$$H_{para-d} = \sum_{j\in e^-} \frac{e}{m}\boldsymbol{p}_j \cdot \mathbf{A}_d \cos(\omega_L t) \tag{3.3}$$

and diamagnetic interactions,

$$H_{dia-c} = \sum_{j\in e^-} \frac{e^2}{2m}\frac{\hbar}{\mathcal{V}_c\epsilon_0\epsilon_r\omega_c} 4\cos^2(q_0 x_j)\left(b + b^\dagger\right)^2 \tag{3.4}$$

$$H_{dia-d} = \sum_{j\in e^-} \frac{e^2}{2m}\mathbf{A}_d \cos(\omega_L t)\cdot\mathbf{A}_d \cos(\omega_L t) \tag{3.5}$$

$$H_{dia-cd} = \sum_{j\in e^-} \frac{e^2}{m}\sqrt{\frac{\hbar}{\mathcal{V}_c\epsilon_0\epsilon_r\omega_c}} 2\cos(q_0 x_j)|\mathbf{A}_d|\cos(\omega_L t)\left(b + b^\dagger\right) \tag{3.6}$$

We examine them individually in Sec. 3.3.1 and 3.3.2, and we explain the conditions for H_{dia-cd} (which is the term that gives rise to the effect we discuss in this chapter) to dominate over the others.

3.3.1 Paramagnetic interactions

H_{para-c} describes the paramagnetic interactions between the electrons and the cavity modes. After second quantize the electronic operators as explained in Sec. 2.1.1, we

get the interaction Hamiltonian of the form

$$H_{para-c} = \sum_{\mathbf{k},\sigma,\mathbf{q}} g_{\mathbf{k}}^{para-c}/\sqrt{\mathcal{S}} c_{\mathbf{k},\sigma}^{\dagger} c_{\mathbf{k}-\mathbf{q},\sigma}(b + b^{\dagger}),$$

where $\mathbf{q} = \pm q_0 \mathbf{e}_x$. $\mathcal{S} \propto 1/\omega_c^2$ is the cavity area in the xy-plane. The proportionality constant is obtained using values of electron density and number of electrons from Ref. [49]. The matrix elements evaluate to $g_{\mathbf{k}}^{para-c}/\sqrt{\mathcal{S}} \sim (\hbar|\mathbf{k}|e/m^*)\sqrt{\hbar/\Lambda \mathcal{V}_c \epsilon_r \epsilon_0 \omega_c}$ for $|\mathbf{k}| \gg q_0$.

We'd like to draw attention to the fact that the paramagnetic coupling strength is inversely proportional to the effective mass rather than the bare electron mass [97][2]. We thus learn that this interaction is weaker for less mobile electrons.

In Ref. [70], it is shown that the strength of the effective (current-current) interactions between electrons due to the paramagnetic interactions are $\sim g_{\mathbf{k}}^{para-c} g_{\mathbf{k}'}^{para-c}/\hbar\omega_c \mathcal{S}$. We compare these paramagnetic interactions to the stimulated diamagnetic scatterings discussed below, and note that the two interaction terms in Eq. (3.2) and Eq. (3.6) coincide once one switches $\mathbf{p}$ with $e\mathbf{A}_d$. Hence, we obtain an expression for the critical intensity for the driving laser, $I_{c,1}$ (corresponding to a critical magnitude for vector potential for the driving field, $|\mathbf{A}_d|_{c,1}$), $e|\mathbf{A}_d|_{c,1} \sim |\langle \mathbf{k}_F|\mathbf{p}e^{-i\mathbf{q}\cdot\boldsymbol{r}}|\mathbf{k}_F + \mathbf{q}\rangle| \sim (m/m^*)\hbar k_F$ for $|\mathbf{q}| \ll k_F$. This gives

$$I_{c,1} \sim \left(\frac{m}{m^*}\right)^2 \frac{\hbar\omega_L^2 \sqrt{\epsilon_r} n_e}{2\alpha},$$

where α is the fine structure constant and n_e is the electron density per unit area. Beyond this intensity the paramagnetic interactions are weaker than the stimulated diamagnetic interactions.

H_{para-d} does not cause electron scatterings for a one-band system since the driving field carries no momentum in the xy-plane. When there are strongly detuned electronic bands, H_{para-d} gives rise to vertical (interband) virtual transitions and the electronic bands gain momentum-dependent shifts known as dynamical Stark shifts, whose magnitudes are inversely proportional to the detunings between the driving frequency and the electronic band gap [98]. We here assume that this detuning is sufficiently large for us to neglect the change to the electronic band of interest. We note that one implication with this assumption is that it could limit the range of materials in superconducting states to which application of the scheme discussed in this chapter is possible. The reason is that we require the driving and cavity frequency to be greater than the superconducting gap, but the quasiparticle continuum of a

[2]One can convince themselves using the $k \cdot p$ theory.

superconductor typically has a bandwidth wider than the energy scales of a terahertz photon. In this case, many interband quasiparticle excitations will occur due to the driving, and they can be a significant source of heating through Auger scattering [99] or excitation of phonons [100]. Further investigation of these effect and how it affects the superconducting critical temperatures should be studied in the future. The dynamic localisation effect of the oscillating field from this term on the mobility of electrons [101], which is independent from the other electronic bands, is also negligibly small for realistic systems, e.g., in Ref. [102] the fractional change due to this effect is less than 10^{-4}.

3.3.2 Diamagnetic interactions

H_{dia-c} describes the diamagnetic interactions involving only the cavity modes. These interactions scatter electrons and also shift the electron dispersions due to the term proportional to $(e^2/m)(\hbar/\mathcal{V}_c\epsilon_0\epsilon_r\omega_c)\left(2b^\dagger b+1\right)\sum_{\mathbf{k}} n_{\mathbf{k}}$. The other terms involves operators like $b^\dagger b^\dagger$ and bb, so they rotate rapidly (at $\pm 2\omega_L$) in the co-rotating frame of the driving laser and contribute terms of the order $\mathcal{O}(1/2\omega_L)$ to the electron dynamics.

In order to neglect this diamagnetic interaction term when the cavity is not populated (shown later), the cavity field's vacuum fluctuations shouldn't be larger than the driving field. Thus, we can estimate another critical intensity, $I_{c,2}$ (corresponding to a critical magnitude for vector potential for the driving field, $|\mathbf{A}_d|_{c,2}$) beyond which we can neglect the diamagnetic scatterings between only cavity photons: $|\mathbf{A}_d|_{c,2} \sim \sqrt{\hbar/\Lambda\lambda^3\epsilon_0\epsilon_r\omega_c}$

$$\implies I_{c,2} \sim \frac{\hbar\omega_L^2 c}{\Lambda\sqrt{\epsilon_r}\omega_c\lambda^3}.$$

H_{dia-d} is a sinusoidally oscillating constant and does not alter the electronic or the photonic states because the laser photons carry no in-plane momentum. We have again assumed that other electronic bands are so far detuned that we can neglect vertical transitions.

H_{dia-cd} describes stimulated diamagnetic scatterings involving both the laser and the cavity modes. These scatterings include near-resonant processes [schematically shown in Fig. 3.1(b)]. In contrast, the single-photon processes of paramagnetic scatterings which normally dominate the optical response of materials are far off-resonant within the single electronic band. Thus, when the driving is strong (specified below), these two-photon processes become the principal coupling mechanism of the electrons

to the cavity field fluctuations and dominate the dynamics. In the present chapter, we focus on this situation.

The discussion is clearer when we move into a frame co-rotating with the laser frequency ω_L using the unitary transformation $U(t) = \exp\big(-i\omega_L t b^\dagger b\big)$, see Fig. 3.2(a). This transformation does not affect the electronic Hamiltonian but changes ω_c in H_{cav} to δ_c ($|\delta_c| \ll \omega_c$) and removes the explicit time dependence of the near-resonant two-photon diamagnetic interactions. In the rotating frame, all the one-photon interaction terms oscillate rapidly at ω_L, thus their effect on the electrons is proportional to $\sim 1/\omega_L$. In contrast, the effect of two-photon diamagnetic interactions (apart from an irrelevant energy shift) is proportional to $\sim 1/\delta_c \gg 1/\omega_L$. Note that we ignore the rapidly rotating (at $\pm 2\omega_L$) terms from the diamagnetic interactions.

In this rotating frame, the near-resonant part of the two-photon diamagnetic interactions is given by

$$H_{\text{light-matter}} = \sum_{\mathbf{q}=\pm q_0 \mathbf{e}_x} \frac{g_0}{\sqrt{\mathcal{S}}} \varrho_{\mathbf{q}} (b + b^\dagger) \ , \tag{3.7}$$

where the interaction vertex reads $g_0 = \alpha \sqrt{I_{\text{d}} \hbar^3 \omega_c^2 \mathcal{S}/(2\pi m^2 \Lambda \omega_L^2 c^2)}$.

The stimulated diamagnetic interactions compete with paramagnetic scatterings with the cavity photons as well as with diamagnetic scatterings involving only the cavity fields; the stimulated diamagnetic processes can be estimated to dominate above a critical field intensity

$$I_{cr} \sim \max\Big\{I_{c,1}, I_{c,2}\Big\} = \max\Big\{ \Big(\frac{m}{m^*}\Big)^2 \frac{\hbar \omega_L^2 \sqrt{\epsilon_r} n_e}{2\alpha}, \frac{\hbar \omega_L^2 c}{\Lambda \sqrt{\epsilon_r} \omega_c \lambda_0^3} \Big\}.$$

In low-terahertz frequency range (~ 0.1THz), the critical intensity is ~ 50 kWcm^{-2} [the parameters used are given in the caption for Fig. 3.2(b)]. The critical intensity, I_{cr} is almost always $I_{c,1}$, given by the paramagnetic scattering strength with the cavity modes. For materials with higher electron density and lower effective mass, the critical intensity increases.

3.3.3 Effect of the environment modes

The main effect of the environment light modes is the heating of the electrons through inelastic diamagnetic scatterings. We denote the corresponding interaction vertex strength $\eta_{\mathbf{q}_e}$ (its evaluation is the same as diamagnetic scattering involving the laser field and the cavity field). In this process a laser photon scatters with an electron which transitions from quasi-momentum state $|\mathbf{k}\rangle \rightarrow \big|\mathbf{k} + \mathbf{q}_\parallel\big\rangle$, into the outgoing

photon is in the environment mode whose in-plane momentum is $-\mathbf{q}_\parallel$ and energy is $\big(\hbar\omega_L + \epsilon(\mathbf{k}) - \epsilon(\mathbf{k}+\mathbf{q}_\parallel)\big)$. Since the photon momenta are very small, $\epsilon(\mathbf{k}) - \epsilon(\mathbf{k}+\mathbf{q}_\parallel) \ll \hbar\omega_L$. Fermi's golden rule gives us the total scattering rate of an electron in state $|\mathbf{k}\rangle$ by this process,

$$\begin{aligned}\Gamma_{\mathbf{k}} &= \frac{2\pi}{\hbar}\sum_{\mathbf{q}_e=(\mathbf{q}_\parallel,q_z)} |\eta_{\mathbf{q}_e}|^2\delta(\epsilon(\mathbf{k}-\mathbf{q}_\parallel)+\hbar\omega_{\mathbf{q}_e}-\epsilon(\mathbf{k})-\hbar\omega_L)\\ &\approx \frac{2\pi}{\hbar}\sum_{\mathbf{q}_e}\left(\frac{e^2}{m}|\mathbf{A}_d|\sqrt{\frac{\hbar}{\mathcal{V}\epsilon_0\epsilon_r\omega_L}}\cos\theta_{\mathbf{q}_e}\right)^2\delta(\hbar\omega_{\mathbf{q}_e}-\hbar\omega_L)\\ &= \frac{64\pi^3}{3}\frac{1}{\lambda_L^2}\frac{1}{\omega_L}\frac{\alpha^2\hbar I_d}{\epsilon_r m^2\omega_L^2}.\end{aligned} \tag{3.8}$$

Here, $\theta_{\mathbf{q}_e}$ is the polar angle of $\mathbf{q}_e$. In our setup, the ratio of the inelastic scattering rate to the cavit-mediated interaction strength, $\hbar\Gamma_{\mathbf{k}}/(V^{(0)}/\mathcal{S}) \sim \Lambda\delta_c/\omega_L$. $V^{(0)}/\mathcal{S}$ is defined in Eq. (3.9). Therefore, when the cavity mode volume compression is significant, this inelastic scattering is much weaker than the coherent electron interactions. We can further reduce the heating effect from inelastic scattering by increasing ω_L while keeping δ_c constant.

3.4 Cavity-mediated interactions

The light-matter coupling given by Eq. (3.7) yields effective electron interactions through the process depicted in Fig. 3.1(b): a laser photon scatters virtually off an electron into the cavity, where it gets rescattered by a second electron back into the laser beam. The fact that the two-photon diamagnetic interactions couple to the electron density [see Eq. (3.7)] allows us to apply some of the intuition from other boson-exchange interactions [103]. Specifically, it means the exchange of virtual cavity photons (with an effective frequency δ_c in the rotating frame) mediates density-density interactions between the electrons. The interactions will be attractive(repulsive) when $\delta_c > 0 (< 0)$, *i.e.* the driving laser is red(blue)-detuned from the cavity.

The bare retarded interaction created by the exchange of cavity photons reads $V_{\text{ret}}^{\text{bare}}(\mathbf{q},\omega+i\eta) = |g_0|^2 D^{(0)}(\mathbf{q},\omega+i\eta)$, where $\eta = 0^+$ and $D^{(0)}$ is the bare cavity photon Green's function in the rotating frame. We plot this in Fig. 3.2(b). In the static limit $\omega = 0$, we recover the effective interaction Hamiltonian obtained using a Schrieffer-Wolff transformation, $H_{\text{int}} = \frac{1}{2\mathcal{S}}\sum_{\mathbf{q}} V^{(0)}(\mathbf{q})\varrho_{\mathbf{q}}\varrho_{-\mathbf{q}}$, where the expression for the bare interaction potential,

$$\frac{V^{(0)}(\mathbf{q})}{\mathcal{S}} = \frac{\alpha^2\hbar^2}{\pi c^2 m^2}\frac{\omega_c^2}{\omega_L^2}\frac{I_{\text{d}}}{\Lambda\delta_c}\delta_{\pm\mathbf{q},q_0\mathbf{e}_x}, \tag{3.9}$$

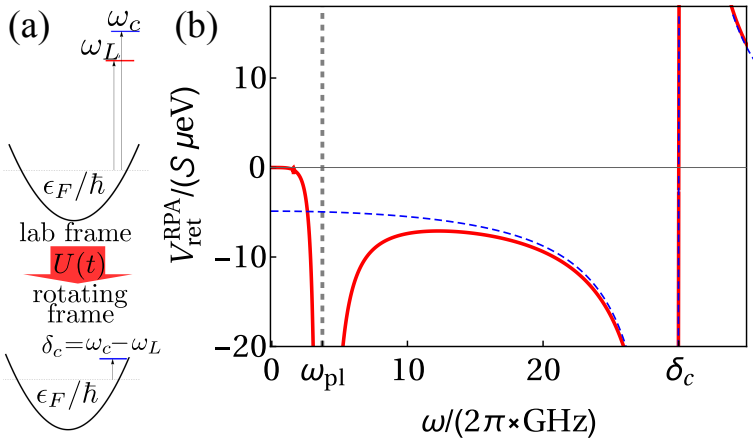


Figure 3.2: (a) Relevant energy levels for the two-photon diamagnetic interactions involving the driving (red) and cavity (blue) fields in the lab frame (top) and in a rotating frame (bottom). The electron dispersion is plotted in black. ϵ_F is the Fermi level. (b) The real part of the screened interaction potential $V_{\rm ret}^{\rm RPA}/\mathcal{S}$ is shown in red. The real part of $V_{\rm ret}^{\rm bare}/\mathcal{S}$ (blue dashed line) is shown for comparison. The plasmon resonance $\omega_{pl}(q_0)$ is indicated by the grey vertical dashed line. The small irregularity below ω_{pl} comes from the discontinuity of the 2D electron polarizability given in Ref. [90]. The cavity parameters used are $\omega_c = 2\pi\times 0.3$ THz, $\delta_c = 0.1\omega_c$, quality factor $Q = 500$ and $\Lambda = 2.5/8\times 10^{-5}$. We set $\mathcal{S}\approx 2.1\times 10^{-5}\lambda^2$, where the proportionality constant is obtained from Ref. [49]. The driving intensity is $I_{\rm d} = 3{\rm MWcm}^{-2}$. We use an electron density $n_e = 10^{12}{\rm cm}^{-2}$ and $m^* = 2m$ consistent with various 2D materials such at (gated) LAO/STO and monolayer TMDs [104, 105, 106]. The plasmon damping rate is set to 10% of plasmon frequency [107]. We consider a $SrTiO_3$ substrate with a large $\epsilon_r \sim 10^4$ at low temperatures [108].

confirms our intuition that the interaction strength is proportional to the driving intensity and can be tuned to be attractive or repulsive by the detuning. We note that this potential only depends on the momentum transferred between the two electrons and does not depend on the electron dispersion. Moreover, $V^{(0)}(\mathbf{q})$ is very localized in momentum space because the photon momenta are much smaller than electronic ones. Hence, these electron interactions are long-ranged in real space. In the following section, we will investigate how they are screened by the two-dimensional electron gas.

3.5 Screening

Previously in Chapter. 2, we have discussed how Coulomb interactions are screened by electrons within the random phase approximation (RPA): they are screened due to electron polarizability. In this section, we discuss how the cavity-mediated interactions are screened by the polarizability of the electrons, which also interact via

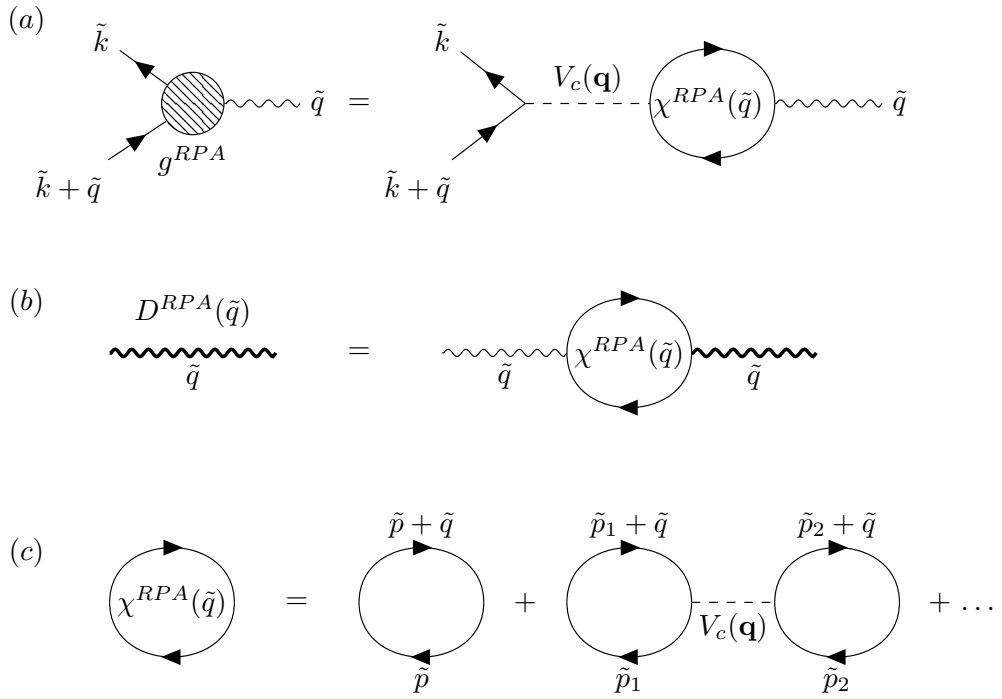


Figure 3.3: (a) RPA screened electron-photon interaction vertex. (b) RPA-renormalised photon Green's function. (c) χ^{RPA} represents the infinite sum of simple bubble diagrams.

Coulomb interactions. We first state the result, before explaining it with the help of Feynman diagrams.

Within the random phase approximation (RPA), the screened interaction potential in imaginary time formalism reads [87],

$$V^{\mathrm{RPA}}(\tilde{q}) = \left|g^{\mathrm{RPA}}(\tilde{q})\right|^2 D^{\mathrm{RPA}}(\tilde{q}) \tag{3.10}$$

$$D^{\mathrm{RPA}}(\tilde{q}) = \frac{D^{(0)}(\tilde{q})}{1 - |g_0|^2\, 2\chi^{\mathrm{RPA}}(\tilde{q}) D^{(0)}(\tilde{q})}, \tag{3.11}$$

where we have used the four-vector notation with $\tilde{q} \equiv \{\mathbf{q}, i\nu_n\}$ at momentum $\mathbf{q}$ and the bosonic Matsubara frequency, $\nu_n = 2\pi n k_{\mathrm{B}} T/\hbar$, $n \in \mathbb{Z}$. k_{B} is the Boltzmann constant, and T is the temperature. χ^{RPA} is the screened polarizability of the two-dimensional electron gas, and g^{RPA} is the screened vertex of Eq. (3.7),

$$g^{\mathrm{RPA}}(\mathbf{q}, i\nu_n) = \frac{g_0}{1 - V_c(\mathbf{q})\chi_0(\mathbf{q}, i\nu_n)} \tag{3.12}$$

$$\chi^{\mathrm{RPA}}(\mathbf{q}, i\nu_n) = \frac{\chi_0(\mathbf{q}, i\nu_n)}{1 - V_c(\mathbf{q})\chi_0(\mathbf{q}, i\nu_n)}. \tag{3.13}$$

Again, $V_c(\mathbf{q}) = \frac{e^2}{2\epsilon_0\epsilon_r q}$ is the Coulomb interaction in momentum space, and χ_0 is the polarizability due to the mobility of the two-dimensional electron gas.

The meaning of these expressions are conveyed more clearly with the Feynman diagrams shown in Fig. 3.3. g^{RPA} describes how the interaction vertex is screened due to electron polarizability and the Coulomb interactions, while D^{RPA} describes how the photon Green's function is renormalised by both the Coulomb interactions and the electron-photon interactions. Note that Eq. (3.11) differs from the definition in Ref. [87] by a factor of 2 in the denominator in front of χ^{RPA}. This is because the scatterings with the cavity mode do not conserve total electron and photon momenta and the simple polarization bubbles connected by Coulomb interactions (which conserve total electron momentum) can be carrying $+/-\hbar\mathbf{q}$ of momentum.

The bare cavity photon Green's function in the rotating frame is

$$D^{(0)}(\mathbf{e}_x q_0, i\nu_n) = \frac{-2\delta_c/\hbar}{\nu_n^2 + \delta_c^2}. \tag{3.14}$$

Notice δ_c replaces ω_c because of the change of frame. We account for the cavity decay rate by including it as a self-energy that is imaginary in real frequency space (which broadens the spectral function) in the bare photon Green's function

$$D^{(0)}(\mathbf{e}_x q_0, i\nu_n) \to \frac{-2\delta_c/\hbar}{\nu_n^2 + \delta_c^2 + 2\delta_c\kappa\ \mathrm{sgn}[\nu_n]}. \tag{3.15}$$

Here, we define the cavity decay rate $\kappa = \omega_c/2Q$, where Q is the cavity quality factor. The decay rate does not have a strong effect on the cavity mediated interaction as long as κ is sufficiently small compared to δ_c.

Since $q_0 \ll k_F$, we are interested in the region of the phase space to the left of the red line in Fig. 3.4. This means we can focus on the small r_q and large r_ω limit that we already discussed in Chapter. 2 for a parabolic band, see Eq. (2.54) and (2.57). In this limit, $\mathrm{Im}\{\chi_0\} = 0$ and $\mathrm{Re}\{\chi_0\} = k_F v_F q^2/\left(\hbar\omega^2 2\pi\right)$, which means

$$g^{\mathrm{RPA}}(\mathbf{q}, \hbar\omega) = \frac{g_0}{1 - \frac{\omega_{\mathrm{pl}}^2(\mathbf{q})}{\omega^2}} \text{ and} \tag{3.16}$$

$$D^{\mathrm{RPA}}(\mathbf{q}, \hbar\omega) = \frac{D^{(0)}}{1 - |g_0|^2 D^{(0)} \frac{2k_F v_F q^2}{\hbar\omega^2 2\pi} / \left(1 - \frac{\omega_{\mathrm{pl}}^2(\mathbf{q})}{\omega^2}\right)}, \tag{3.17}$$

where $\omega_{\mathrm{pl}}(\mathbf{q}) = \sqrt{\alpha k_F v_F q c/\epsilon_r}$ is the plasmon frequency at momentum $(\mathbf{q})$ given in Eq. (2.59). We note that in this long-wavelength limit, only electrons near the Fermi

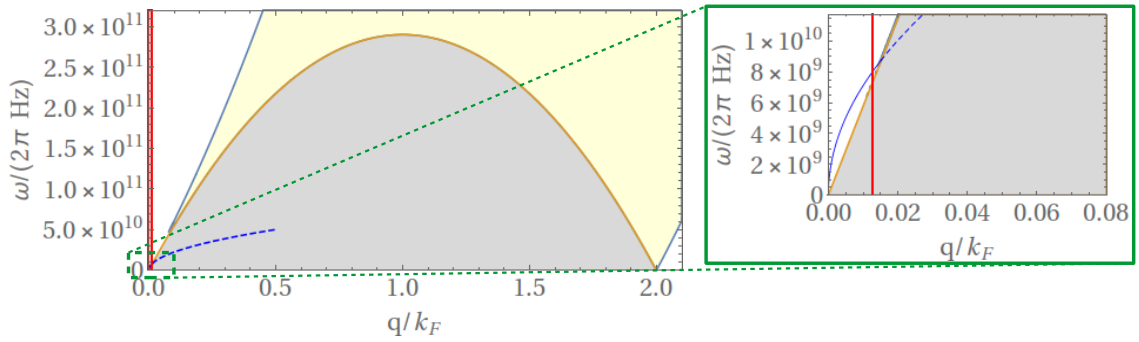


Figure 3.4: Phase space plot. The right figure magnifies the small dashed green box in the left figure. The mobile electron polarizability χ_0 is complex inside the shaded regions. The yellow(grey) region is where one(both) of $|r_q \pm r_\omega| < 1$. Inside both shaded regions energy can be dissipated into the electron systems through single-particle excitations. The part of phase space most relevant for the dynamics we describe is to the left of the red line. Its position corresponds to the momentum of a $\approx$ 1.5THz photon (which is roughly the highest cavity frequency we consider). The blue line is the 2D plasmon dispersion. Where it's dotted means the plasmons are Landau-damped. For the cavity frequencies we consider here, the bare plasmons coupled to the photons are not Landau-damped. We use the same electron parameters as those in Fig. 3.2(b).

surface contribute to screening. Thus, the above results are valid in this limit for other single band dispersions [109].

We plot the plasmon dispersion in Fig. 3.4 for a given electron density. Note that for sufficiently large momenta the plasmons are Landau-damped. However, for the parameters considered in this chapter, we are not in that regime. We found that we would need cavity frequency greater than $\sim$ 2THz in order to couple to Landau-damped plasmons. Yet, this does not affect the stimulated electron interactions we describe in this chapter.

The retarded interaction is obtained from Eq. (3.10) (a function in imaginary frequency) by analytic continuation to real frequencies [88]: $V^{\rm RPA}_{\rm ret}(\omega) = V^{\rm RPA}(\pm q_0 \mathbf{e}_x, i\nu_n \to \omega + i\eta)$. We show an example of the real part of the screened retarded interaction potential as a function of frequency in Fig. 3.2(b). Here, we also included a Drude-like electron damping rate [110, 1] by modifying the electron response function such that $1 - \omega^2_{\rm pl}(\mathbf{q})/\omega^2 \to 1 - \omega^2_{\rm pl}(\mathbf{q})/(\omega^2 + {\rm i}\omega\gamma)$. Evidently, contributions to the interaction at small frequencies are strongly screened. The precise choice of the damping rates alters only the size of the dips at $\omega = \omega_{\rm pl}$ and δ_c but not the interaction potential in the broad region of frequency in between, thus it has little effect on the physics. In the present case where $\delta_c > 0$ the attractive cavity-mediated interaction softens

the plasmons and the cavity frequency is weakly blue-shifted. This effect only becomes appreciable at very large laser intensities, and cannot be seen in Fig. 3.2(b). Crucially, however, for frequencies between the plasmon resonance and the detuning δ_c, the interaction remains attractive (repulsive for $\delta_c < 0$) and is hardly affected by screening.

We can understand this behaviour by realising that in the long-wavelength limit, $\chi^{\mathrm{RPA}} \propto q_0^2$. Physically this means the electrons are too slow to screen the fast oscillating electromagnetic fields and hence the cavity-mediated interactions can only be screened weakly. Corrections to the bare interaction become appreciable when ω approaches the plasmon resonance of the system in the range $\omega_{pl}/2\pi \sim 4$ GHz [for the parameters of Fig. 3.2(b)]. Hence, it is only relevant at temperatures below $T \simeq 30$mK, as we will see in Fig. 3.8. At higher temperatures, the Matsubara frequencies will not cover this low-frequency region and the cavity-mediated interactions cannot be screened effectively by the electron gas. They remain long-ranged interactions that can be imposed externally on the two-dimensional electronic system.

Before we move on to discuss the physical effect of these long-range interactions, we show an example of a repulsive interaction potential achieved with blue-detuned driving in Fig. 3.5.

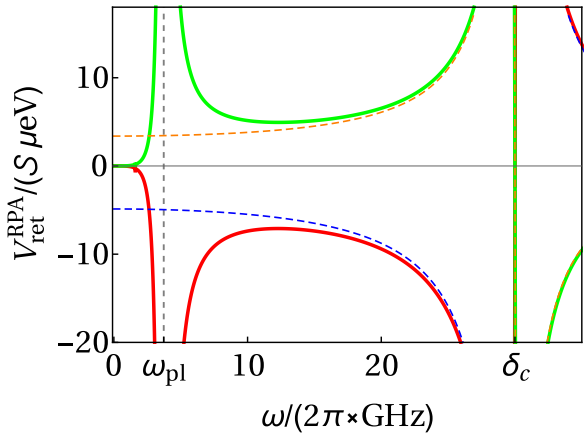


Figure 3.5: The real parts of the screened retarded interaction potentials for red- and blue-detuned driving are shown as red and green solid lines. The corresponding bare interaction potentials are shown with dashed curves. The vertically dashed line represents the plasmon resonance. The attractive potential curves are obtained using the same parameters as those used in Fig. 3.2(b). The repulsive potential curves are obtained with the same parameters except the detuning has the opposite sign.

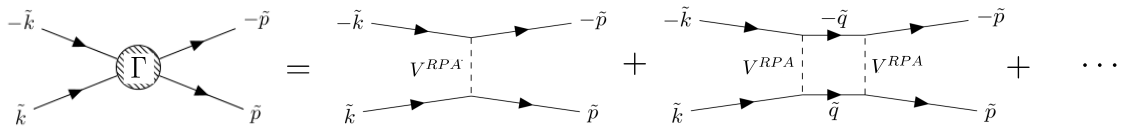


Figure 3.6: The pair scattering vertex Γ is given by an infinite sum of ladder diagrams of an electron pair scattering with each other repeatedly. We consider the Cooper channel, where the electrons have opposite momenta and Matsubara frequencies. The Cooper instability is signified by the divergence of this infinite sum.

3.6 Cooper channel instability

To gauge the strength of the cavity-mediated interactions that could be achieved experimentally, we consider the case of attractive interactions and study the Cooper instability they induce. For now, we ignore the sources of heating discussed in Sec. 3.3 and Appendix. B, though they should be accounted for in order to obtain a more accurate estimate of the critical temperature. This pairing instability occurs when a pair of electrons with opposite momenta and frequencies attract and repeatedly scatter off one another to cause a divergence of the pair scattering vertex $\Gamma(\tilde{k};\tilde{p})$, where $\tilde{k}$ ($\tilde{p}$) is the incoming (outgoing) electron four-momentum [87, 111]. The instability could potentially be detected with techniques such as transport or magnetisation measurements [112, 79, 102]. $\Gamma(\tilde{k};\tilde{p})$ is obtained by solving a Dyson equation that comes from summing an infinite series of ladder diagrams (see Fig. 3.6) [87, 111] using the RPA screened interaction potential,

$$\Gamma(\tilde{k};\tilde{p}) = -V^{\mathrm{RPA}}(\tilde{k}-\tilde{p}) + \frac{1}{\mathcal{S}\beta}\sum_{\tilde{q}}[-V^{\mathrm{RPA}}(\tilde{k}-\tilde{q})]G^{(0)}(\tilde{q})G^{(0)}(-\tilde{q})\Gamma(\tilde{q};\tilde{p}) \ , \quad (3.18)$$

where, again, $\beta = 1/k_B T$, $G^{(0)} = 1/(i\nu_n\hbar - \xi_{\mathbf{q}})$ is the unperturbed electron Matsubara Green's function.

As the photon momentum is very small compared to electronic momenta, we approximate the exact interaction by a δ-function potential in k-space, $V^{\mathrm{RPA}}(\tilde{q}) \propto \delta(\mathbf{q})$, which simplifies the internal summations in the pair scattering ladder diagrams, yielding a matrix equation

$$\Gamma(ik_n;ip_n) = -V^{\mathrm{RPA}}(ik_n - ip_n) + \mathcal{M}(ik_n;i\nu_n)\Gamma(i\nu_n;ip_n), \quad (3.19)$$

where $\mathcal{M}(ik_n;i\nu_n) = -2V^{\mathrm{RPA}}(ik_n - i\nu_n)G^{(0)}(i\nu_n)G^{(0)}(-i\nu_n)/(\mathcal{S}\beta)$. We then numerically compute the temperature T_c, at which $\det\left[\mathbb{1} - \mathcal{M}(\beta_c = 1/k_B T_c)\right] = 0$ and the pair scattering vertex diverges for different choices of driving and cavity parameters. The determinant tends to 1 at high temperatures and reduces as the temperature

lowers. In Fig. 3.7, we plot an example of the determinant as a function of temperature. Note that we introduced a cut-off for the Matsubara frequencies since high frequencies have little effect (due to $G^{(0)}$). We checked that our results do not vary when we alter the cut-off value. In fact, the factor of $G^{(0)}(i\nu_n)G^{(0)}(-i\nu_n) \propto \frac{1}{\nu_n^2}$ for fermionic Matsubara frequency $\nu_n = (2n+1)\pi k_B T/\hbar$ means that the terms in the sum with $n = -1, 0$ are almost a magnitude larger than the terms with $n = -2, 1$. Hence, a numerically quicker and still reasonably accurate way that we used to compute the critical temperatures in Fig. 3.8 is to limit the Matsubara frequencies to just $\pm\pi k_B T/\hbar$, then Eq. (3.19) turns into an algebraic equation to solve:

$$1 = -\frac{2}{\mathcal{S}\beta_c} V^{RPA}(\mathbf{e}_x q_0, 2\mathrm{i}\pi/\hbar\beta_c)\frac{\beta_c^2}{\pi^2} \ . \tag{3.20}$$

This method underestimate T_c only by a few percent compared to more accurate results using a higher cut-off.

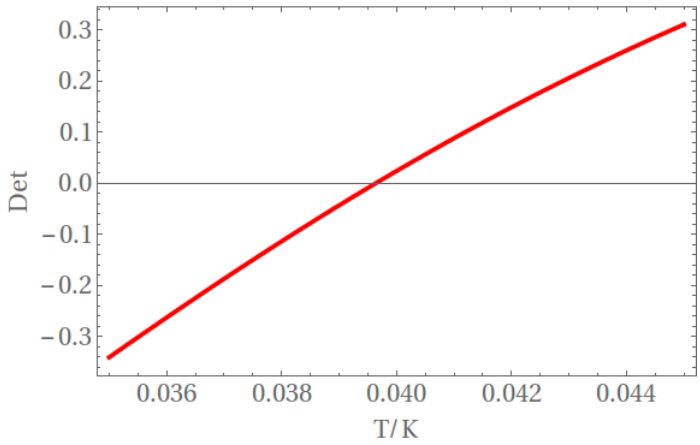


Figure 3.7: Determinant of $(\mathbb{1} - \mathcal{M})$ plotted as a function of temperature using the following parameters: $I_{\mathrm{dr}} \approx 6\mathrm{MWcm}^{-2}$, $\omega_c \approx 2\pi \times 0.1\mathrm{THz}$, $\delta_c \approx 0.05\ \omega_c$ and the same electron system parameters as in Fig. 3.2(b). The point where it crosses zero is the Cooper instability critical temperature.

T_c depends on the driving intensity, the cavity frequency and the detuning. In the following, we vary the detuning to obtain the highest critical temperature for fixed intensities. The results are shown in Fig. 3.8, where the highest T_c, $T_c^{\max}$ (top panel), and the corresponding detuning δ_c^{op} (bottom panel) are plotted against the intensity for four sets of electron and substrate parameters. We find that provided $\omega_c \gg \delta_c$ and δ_c is well above the plasmon resonance T_c depends very weakly on ω_c once we fix δ_c: a smaller ω_c raises T_c very slightly. We remark that the necessary intensities to induce $T_c \sim 1$ K are experimentally achievable with pulsed THz light

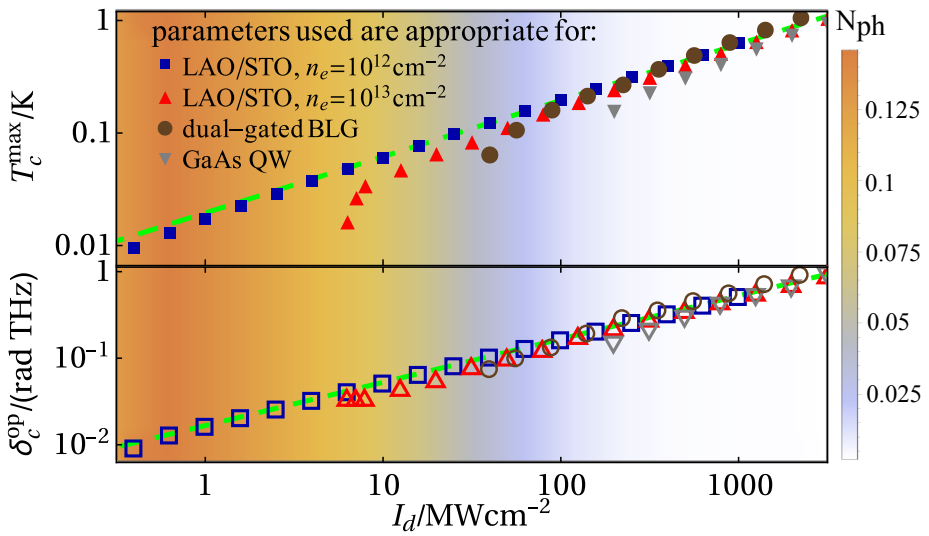


Figure 3.8: Maximum T_c's (w.r.t. driving and cavity parameters) for the Cooper channel instability (top panel) and the optimal detunings, $\delta_c^{\rm op}$, (bottom panel) are plotted for a range of driving intensities. We calculate them for four sets of electron parameters. All of them follow the dashed green line (same in both panels) representing Eq. (3.21) at large enough driving intensities. The colour map shows the cavity photon number $\mathrm{N_{ph}}$ for different $I_{\rm d}$ with the optimal driving and cavity parameters at $T_c^{\max}$ using electron and substrate parameters appropriate for gated LAO/STO [same as those used in Fig. 3.2(b)]. We used $n_e = 3\times10^{11}$, $5\times10^{10}\mathrm{cm}^{-2}$, $\epsilon_r = 10$, 13 for dual-gated BLG and GaAs based quantum well (QW) respectively [113, 114, 115]; $m^* = 0.07m$ for GaAs QW [115]. AB-stacked BLG dispersion is calculated as in Ref. [116] with a gate-induced band gap of 50meV. We used $\omega_c = 10\ \delta_c^{\rm op}$.

sources [117, 118, 119, 21, 120, 121]. At these high intensities, laser-induced heating of the substrate material becomes relevant (see Appendix. B), such that a pulse driving protocol might become necessary. The green dashed line represents a function $\propto \sqrt{I_{\rm d}}$ and it fits the $T_c^{\max}$ and the $\delta_c^{\rm op}$ points very well at high driving intensities,

$$T_c^{\max}/\mathrm{K} \approx \delta_c^{\rm op}\ \mathrm{ps/rad} \approx 10^{-4.5}\sqrt{I_{\rm d}/(\Lambda\ \mathrm{MWcm^{-2}})}. \tag{3.21}$$

The numerical constants depend only on fundamental constants. The deviations of our numerical results in Fig. 3.8 from Eq. (3.21) at smaller intensities are caused by the screening due to plasmons which reduces $T_c^{\max}$. Consequently, the onset of this deviation is determined by the plasmon frequency and hence the substrate dielectric constant, the 2D electron density and the Fermi velocity. The materials with fewer data points in Fig. 3.8 have higher plasmon resonances, so the screening is stronger for them, causing $T_c^{\max}$ to drop quickly to 0 at higher intensities than materials with lower plasmon resonances.

Fig. 3.8 shows that in order to achieve the highest critical temperature at a given driving intensity, one must choose an appropriate detuning (and hence cavity and driving frequencies). We understand this by inspecting the analytic expression we obtained above [Eq. (3.20)]: $k_B T_c \approx -2\pi^{-2} V^{\mathrm{RPA}}(q_0 \mathbf{e}_x, 2\mathrm{i}\pi k_B T_c/\hbar)/\mathcal{S}$ and realising that above the plasmon resonance, the interaction is effectively unscreened. Thus, for a perfect cavity $V^{\mathrm{RPA}} \propto I_{\mathrm{d}}\delta_c/((2\pi k_B T_c/\hbar)^2 + \delta_c^2)$. For all values of T_c, this is maximised when we choose $\delta_c^{\mathrm{op}} = 2\pi k_B T_c/\hbar$. We substitute the two relations above back into the approximate equation for the critical temperature to obtain $T_c^{\max} \propto \sqrt{I_{\mathrm{d}}}$ consistent with Fig. 3.8 and Eq. (3.21). We note that a finite cavity decay rate reduces δ_c^{op} only slightly.

We furthermore calculated the cavity photon population $\mathrm{N_{ph}}$ (see colorbar in Fig. 3.8) using the optimal cavity and driving parameters. In Chapter. 2, we have discussed that in the non-rotating frame, the equilibrium population of bosons $N_{\mathbf{p}}$ is given by Bose-Einstein distribution, $n_B(\omega) = 1/(e^{\beta\hbar\omega} - 1)$, and the imaginary part of the retarded bosonic Green's function in the non-rotating (the lab) frame, $D^{\mathrm{lab}}_{\mathrm{ret}}(\mathbf{p}, \omega)$, see Eq. (2.64).

In our case, since we work in the rotating frame of the laser and the unperturbed bosonic Green's functions we use is defined in the rotating frame, we need an adjusted Bose-Einstein distribution,

$$n_B^{'}(\omega) = \frac{1}{\exp\left(\beta\hbar(\omega + \mathrm{sgn}[\omega]\omega_L)\right) - 1} \tag{3.22}$$

to reflect that we are in the co-rotating frame. Thus, the cavity photon population is given by

$$2N_{\mathbf{p}} + 1 = \int_{-\infty}^{\infty} \frac{\mathrm{d}\omega\hbar}{2\pi} n_B^{'}(\omega)(-2\,\mathrm{Im}\{D^{\mathrm{RPA}}_{\mathrm{ret}}(\mathbf{p}, \omega)\}) \tag{3.23}$$

The result in Fig. 3.8 verifies that the cavity photon population $\mathrm{N_{ph}}$ remains low and justifies neglecting two-photon diamagnetic interactions involving only the cavity modes ($\mathbf{A}_c^2$ terms). The decrease of $\mathrm{N_{ph}}$ with higher driving intensity is due to the fact the cavity resonance is higher in frequency. In particular, at higher driving frequencies the plasmon resonance and the cavity detuning are further separated in energy, reducing the effect of plasmons on the cavity (see the discussion above). If the cavity frequency were kept constant, higher driving intensity would have resulted in higher cavity population. Finally, we note that keeping δ_c well above the cavity linewidth and the plasmon frequency suppresses the effect of cavity-induced heating or cooling [122].

3.7 Conclusion

In this chapter, we showed that the combination of external driving and strong coupling to a cavity induces controllable long-range electron interactions in single-band 2D materials. Provided that the driving is detuned from the cavity further than the plasmon frequencies at the relevant wavevectors, the interactions cannot be effectively screened. The interactions are generated by two-photon diamagnetic processes. Therefore, they are largely independent of the electron band dispersion and can be induced on top of existing interactions. These induced interactions could be used to control or enhance existing instabilities or give rise to different quantum states through competition with other short-range interactions [123, 124, 125, 126]. To date, engineered long-range quantum fluctuation-mediated interactions have mainly been studied in the context of ultracold atoms [127, 128, 129, 96, 130, 123, 131, 132, 133, 134, 135, 136, 137]. Our proposal potentially opens the possibility to explore a vast range of novel physics related to unscreened controllable long-range interactions in condensed matter setups.

In Chapter. 5, we study the effect of these long-range interactions on BCS superconductors. Before that, we first review the BCS theory of superconductivity [138] in the next chapter.

Chapter 4

A brief review of the BCS theory

In Chapter. 5, we will consider an application of the induced long-range interactions introduced in Chapter. 3 in enhancing BCS superconductivity and stabilizing the Higgs mode in a s-wave superconductor. We will apply the BCS theory to the study the effect of the long-range interactions. Therefore, in this chapter, we briefly review the BCS theory [138]. Specifically, we present the mean-field approximation made and the self-consistency condition known also as the "gap equation", which yields quantities such as the superconducting critical temperature. We also present Anderson's pseudospin representation of the BCS theory, which provides an easier way to visualisation, and it is useful towards describing collective excitations on top of the superconducting ground state. Though we start with a general framework, for concreteness and for preparation for the next chapter, in this chapter we provide examples for conventional electron-phonon superconductors in which the electron attractions are local.

4.1 BCS mean field theory

4.1.1 Mean fields

We consider the following general BCS reduced Hamiltonian describing electrons with a pairing potential in momentum space,

$$H_{\mathrm{BCS}} = \sum_{\mathbf{k}\sigma} \xi_{\mathbf{k},\sigma} c^{\dagger}_{\mathbf{k},\sigma} c_{\mathbf{k},\sigma} + \frac{1}{2} \sum_{\mathbf{k}_1,\mathbf{k}_2,\sigma_1,\sigma_2,\sigma_3,\sigma_4} V_{\sigma_1,\sigma_2,\sigma_3,\sigma_4}(\mathbf{k}_1,\mathbf{k}_2) c^{\dagger}_{-\mathbf{k}_1,\sigma_1} c^{\dagger}_{\mathbf{k}_1,\sigma_2} c_{\mathbf{k}_2,\sigma_3} c_{-\mathbf{k}_2,\sigma_4}. \tag{4.1}$$

$\xi_{\mathbf{k},\sigma}$ is the dispersion of the electrons measured from the Fermi surface. $V_{\sigma_1,\sigma_2,\sigma_3,\sigma_4}(\mathbf{k}_1,\mathbf{k}_2)$ denotes the electron interaction matrix element, which satisfies $V_{\sigma_1,\sigma_2,\sigma_3,\sigma_4}(\mathbf{k}_1,\mathbf{k}_2) = -V_{\sigma_2,\sigma_1,\sigma_3,\sigma_4}(-\mathbf{k}_1,\mathbf{k}_2) = -V_{\sigma_1,\sigma_2,\sigma_4,\sigma_3}(\mathbf{k}_1,-\mathbf{k}_2) = V_{\sigma_4,\sigma_3,\sigma_2,\sigma_1}(\mathbf{k}_2,\mathbf{k}_1)$ due to the fermionic

anticommutation relation. Notice that we have kept only interactions between electron pairs in the Cooper channel in the second term as the instability is strongest in this channel [3].

The BCS mean fields (MF) are defined as

$$\Delta_{\sigma_1,\sigma_2}(\mathbf{k}) \equiv -\sum_{\mathbf{k}',\sigma_3,\sigma_4} V_{\sigma_2,\sigma_1,\sigma_3,\sigma_4}(\mathbf{k},\mathbf{k}')\langle c_{\mathbf{k}',\sigma_3} c_{-\mathbf{k}',\sigma_4}\rangle \tag{4.2a}$$

$$\Delta^*_{\sigma_1,\sigma_2}(-\mathbf{k}) \equiv \sum_{\mathbf{k}',\sigma_3,\sigma_4} V_{\sigma_3,\sigma_4,\sigma_2,\sigma_1}(\mathbf{k}',\mathbf{k})\langle c^\dagger_{-\mathbf{k}',\sigma_3} c^\dagger_{\mathbf{k}',\sigma_4}\rangle, \tag{4.2b}$$

where $\langle ... \rangle$ means thermodynamic averaging at temperature $T = 1/k_B\beta$. Due to fermionic statistics, these mean fields satisfy

$$\hat{\Delta}_{\mathbf{k}} = \begin{bmatrix} \Delta_{\mathbf{k}\uparrow\uparrow} & \Delta_{\mathbf{k}\uparrow\downarrow} \\ \Delta_{\mathbf{k}\downarrow\uparrow} & \Delta_{\mathbf{k}\downarrow\downarrow} \end{bmatrix} = -\begin{bmatrix} \Delta_{-\mathbf{k}\uparrow\uparrow} & \Delta_{-\mathbf{k}\downarrow\uparrow} \\ \Delta_{-\mathbf{k}\uparrow\downarrow} & \Delta_{-\mathbf{k}\downarrow\downarrow} \end{bmatrix} = -\hat{\Delta}^T_{-\mathbf{k}}. \tag{4.3}$$

4.1.2 Mean-field Hamiltonian and the gap equation

The BCS MF theory proceeds by assuming the fluctuations around the MF values are small and can be ignored. This way, H_{BCS} is approximated by a one-particle Hamiltonian,

$$H_{\mathrm{MF}} = \sum_{\mathbf{k}\sigma} \xi_{\mathbf{k},\sigma} c^\dagger_{\mathbf{k},\sigma} c_{\mathbf{k},\sigma} + \frac{1}{2}\sum_{\mathbf{k},\sigma_1,\sigma_2} \Big[\Delta_{\sigma_1,\sigma_2}(\mathbf{k}) c^\dagger_{\mathbf{k},\sigma_1} c^\dagger_{-\mathbf{k},\sigma_2} - \Delta^*_{\sigma_1,\sigma_2}(-\mathbf{k}) c_{-\mathbf{k},\sigma_1} c_{\mathbf{k},\sigma_2}\Big]. \tag{4.4}$$

We dropped the terms containing only the MF since they only shift the ground state energy [138]. The structure of this Hamiltonian is clearer when rewritten using the four-component notation

$$\mathbf{c}_{\mathbf{k}} \equiv (c_{\mathbf{k},\uparrow}, c_{\mathbf{k},\downarrow}, c^\dagger_{-\mathbf{k},\uparrow}, c^\dagger_{-\mathbf{k},\downarrow}). \tag{4.5}$$

The Hamiltonian matrix is

$$H_{\mathrm{MF}} = \sum_{\mathbf{k}} \frac{1}{2}\mathbf{c}^\dagger_{\mathbf{k}} \mathcal{H}_{\mathbf{k}} \mathbf{c}_{\mathbf{k}} + \text{const.} \tag{4.6}$$

$$\mathcal{H}_{\mathbf{k}} = \begin{bmatrix} \xi_{\mathbf{k}\uparrow} & 0 & \Delta_{\mathbf{k}\uparrow\uparrow} & \Delta_{\mathbf{k}\uparrow\downarrow} \\ 0 & \xi_{\mathbf{k}\downarrow} & \Delta_{\mathbf{k}\downarrow\uparrow} & \Delta_{\mathbf{k}\downarrow\downarrow} \\ \Delta^*_{-\mathbf{k}\uparrow\uparrow} & \Delta^*_{\mathbf{k}\uparrow\downarrow} & -\xi_{-\mathbf{k}\uparrow} & 0 \\ \Delta^*_{-\mathbf{k}\downarrow\uparrow} & \Delta^*_{\mathbf{k}\downarrow\downarrow} & 0 & -\xi_{-\mathbf{k}\downarrow} \end{bmatrix} \tag{4.7}$$

The diagonalisation of the Hamiltonian matrix is achieved by applying a unitary transformation

$$\mathcal{U}_{\mathbf{k}} = \begin{bmatrix} u_{\mathbf{k}\uparrow\uparrow} & u_{\mathbf{k}\uparrow\downarrow} & v_{\mathbf{k}\uparrow\uparrow} & v_{\mathbf{k}\uparrow\downarrow} \\ u_{\mathbf{k}\downarrow\uparrow} & u_{\mathbf{k}\downarrow\downarrow} & v_{\mathbf{k}\downarrow\uparrow} & v_{\mathbf{k}\downarrow\downarrow} \\ v^*_{-\mathbf{k}\uparrow\uparrow} & v^*_{-\mathbf{k}\uparrow\downarrow} & u^*_{-\mathbf{k}\uparrow\uparrow} & u^*_{-\mathbf{k}\uparrow\downarrow} \\ v^*_{-\mathbf{k}\downarrow\uparrow} & v^*_{-\mathbf{k}\downarrow\downarrow} & u^*_{-\mathbf{k}\downarrow\uparrow} & u^*_{-\mathbf{k}\downarrow\downarrow} \end{bmatrix} \tag{4.8}$$

to $\mathcal{H}_{\mathbf{k}}$,

$$\mathcal{E}_{\mathbf{k}} = \mathcal{U}_{\mathbf{k}}^{\dagger}\mathcal{H}_{\mathbf{k}}\mathcal{U}_{\mathbf{k}}, \text{ such that} \tag{4.9}$$

$$\mathcal{E}_{\mathbf{k}} = \text{diag}\left(E_{\mathbf{k}+}, E_{\mathbf{k}-}, -E_{-\mathbf{k}+}, -E_{-\mathbf{k}-},\right). \tag{4.10}$$

The diagonal elements of $\mathcal{E}_{\mathbf{k}}$ give the quasiparticle excitation spectrum of the system. Quasiparticles are charged fermionic excitations; their operators are linear combinations of the bare electron operators, e.g., $\gamma_{\mathbf{k}} = \mathcal{U}_{\mathbf{k}}^{\dagger}\mathbf{c}_{\mathbf{k}}$. They can be excited, e.g. linearly by light, thus making probing the quaiparticle dispersion by angle-resolved photoemission spectroscopy (ARPES) [139] possible.

For the purpose of this thesis, we limit ourselves to systems with time-reversal symmetry. In this case, the unitary transformation is given by [138]

$$\begin{bmatrix} u_{\mathbf{k}\uparrow\uparrow} & u_{\mathbf{k}\uparrow\downarrow} \\ u_{\mathbf{k}\downarrow\uparrow} & u_{\mathbf{k}\downarrow\downarrow} \end{bmatrix} = \frac{E_{\mathbf{k}} + \xi_{\mathbf{k}}}{\left[\left(E_{\mathbf{k}} + \xi_{\mathbf{k}}\right)^2 + \frac{1}{2}\,\text{Tr}\left\{\hat{\Delta}_{\mathbf{k}}\hat{\Delta}_{\mathbf{k}}^{\dagger}\right\}\right]^{\frac{1}{2}}} \begin{bmatrix} 1 & 0 \\ 0 & 1 \end{bmatrix} \tag{4.11a}$$

$$\begin{bmatrix} v_{\mathbf{k}\uparrow\uparrow} & v_{\mathbf{k}\uparrow\downarrow} \\ v_{\mathbf{k}\downarrow\uparrow} & v_{\mathbf{k}\downarrow\downarrow} \end{bmatrix} = \frac{-1}{\left[\left(E_{\mathbf{k}} + \xi_{\mathbf{k}}\right)^2 + \frac{1}{2}\,\text{Tr}\left\{\hat{\Delta}_{\mathbf{k}}\hat{\Delta}_{\mathbf{k}}^{\dagger}\right\}\right]^{\frac{1}{2}}} \begin{bmatrix} \Delta_{\mathbf{k}\uparrow\uparrow} & \Delta_{\mathbf{k}\uparrow\downarrow} \\ \Delta_{\mathbf{k}\downarrow\uparrow} & \Delta_{\mathbf{k}\downarrow\downarrow} \end{bmatrix} \tag{4.11b}$$

$$E_{\mathbf{k}+} = E_{\mathbf{k}-} = E_{\mathbf{k}} = \left[\xi_{\mathbf{k}}^2 + \frac{1}{2}\,\text{Tr}\left\{\hat{\Delta}_{\mathbf{k}}\hat{\Delta}_{\mathbf{k}}^{\dagger}\right\}\right]^{\frac{1}{2}}. \tag{4.11c}$$

These results allow us to derive a self-consistency equation for the MF defined in Eq. (4.2),

$$\Delta_{\sigma_1,\sigma_2}(\mathbf{k}) = -\sum_{\mathbf{k}',\sigma_3,\sigma_4} V_{\sigma_2,\sigma_1,\sigma_3,\sigma_4}(\mathbf{k},\mathbf{k}')\frac{\tanh\frac{\beta E_{\mathbf{k}'}}{2}}{2E_{\mathbf{k}'}}\Delta_{\sigma_3,\sigma_4}(\mathbf{k}'). \tag{4.12}$$

The gap equation is a central entity in BCS theory. We can obtain the MF by solving the gap equation at any specified temperature. The smallest β that gives a nonzero value for the MF (also know as the gap function), gives the superconducting critical temperature; and the symmetry of the gap function gives the symmetry of the superconducting state. We will show these with a concrete example of singlet s-wave superconductor later.

4.1.3 Structure of the spin sector

In this thesis, we restrict ourselves to systems without external magnetic fields or spin-orbit interactions for simplicity. Thus, the spin sector is separated from the orbital degrees of freedom, and there is a $SU(2)$ symmetry in the spin sector. This

allows us to block-diagonalise Eq. (4.12) into a spin-singlet subsector and a spin-triplet subsector with the orbital degrees of freedom in the two subsectors having opposite parities.

In other words, this means that for each $\mathbf{k}$, the 4-dimensional space spanned by

$$\{\Delta_{\uparrow,\uparrow}(\mathbf{k}), \Delta_{\uparrow,\downarrow}(\mathbf{k}), \Delta_{\downarrow,\uparrow}(\mathbf{k}), \Delta_{\downarrow,\downarrow}(\mathbf{k})\}$$

is divided into a one-dimensional singlet space of

$$\Delta_s(\mathbf{k}) = \frac{1}{\sqrt{2}} \left(\Delta_{\uparrow,\downarrow}(\mathbf{k}) - \Delta_{\downarrow,\uparrow}(\mathbf{k})\right) \tag{4.13}$$

and a three-dimensional triplet space spanned by

$$\Delta_{t,-1}(\mathbf{k}) = \Delta_{\downarrow,\downarrow}(\mathbf{k}) \tag{4.14a}$$

$$\Delta_{t,0}(\mathbf{k}) = \frac{1}{\sqrt{2}} \left(\Delta_{\uparrow,\downarrow}(\mathbf{k}) + \Delta_{\downarrow,\uparrow}(\mathbf{k})\right) \tag{4.14b}$$

$$\Delta_{t,1}(\mathbf{k}) = \Delta_{\uparrow,\uparrow}(\mathbf{k}). \tag{4.14c}$$

Combined with Eq. (4.3), we get that the singlet's orbital degrees of freedom has inversion symmetry, $\Delta_s(\mathbf{k}) = \Delta_s(-\mathbf{k})$, while for the triplets, they have antisymmetry upon inversion, $\Delta_t(\mathbf{k}) = -\Delta_t(-\mathbf{k})$. From this, we see that s- and d-wave superconductors have spin-singlets, whereas p-wave superconductors have spin-triplets.

In the next chapter, we consider a superconductor with a s-wave ground state. Thus, here we show how to apply BCS theory using a simple example of an s-wave phonon-mediated superconductor whose interactions are of density-density type and local in real space.

4.1.4 Example: s-wave electron-phonon superconductivity

To describes this type of conventional superconductor without external fields, the electron dispersion [from Eq. (4.1)] is spin-independent $\xi_{\mathbf{k},\sigma} = \xi_{\mathbf{k}}$ and the interaction matrix elements are $\mathbf{k}$-independent,

$$V_{\uparrow,\uparrow,\uparrow,\uparrow}(\mathbf{k}_1, \mathbf{k}_2) = V_{\uparrow,\downarrow,\downarrow,\uparrow}(\mathbf{k}_1, \mathbf{k}_2) = V_{\downarrow,\uparrow,\uparrow,\downarrow}(\mathbf{k}_1, \mathbf{k}_2) = V_{\downarrow,\downarrow,\downarrow,\downarrow}(\mathbf{k}_1, \mathbf{k}_2) = -V,\ V > 0, \tag{4.15}$$

for $\xi_{\mathbf{k}_{1,2}} < \epsilon_{\mathrm{D}}$. ϵ_{D} is the Debye energy, which sets the cutoff energy scale. The matrix elements for all other permutations of the spin indices and choices of $\mathbf{k}$'s are zero.

The gap-equation [Eq. (4.12)] after separation into spin-singlet (with gap function Δ_s) and spin-triplet (with gap function Δ_t) sectors becomes

$$\Delta_s(\mathbf{k}) = V \sum_{\mathbf{k}'} \frac{\tanh \frac{\beta E_{\mathbf{k}'}}{2}}{2E_{\mathbf{k}'}} \Delta_s(\mathbf{k}'), \text{ and} \tag{4.16}$$

$$\Delta_{t,i=-1,0,1}(\mathbf{k}) = V \sum_{\mathbf{k}'} \frac{\tanh \frac{\beta E_{\mathbf{k}'}}{2}}{2E_{\mathbf{k}'}} \Delta_{t,i}(\mathbf{k}') = 0. \tag{4.17}$$

The triplet gap function vanishes because of its anti-symmetry upon inversion of $\mathbf{k}$. We also see that for the singlet gap equation, only s-wave can be non-zero since the average over the momentum space results in zero for all gap functions with orbital angular momenta higher than 0. Therefore, we only need to consider the singlet s-wave gap, and we can drop the spin subscript of the gap function.

Additionally, when the dispersion has rotational symmetry near the Fermi surface, as we will assume here and in the next chapter, the gap function does not depend on the azimuthal angle. In this specific case where the interaction is momentum-independent, $\Delta(\mathbf{k}) = \Delta^{\text{in}}(T)$ is a constant in k-space (within the energy cutoff ϵ_{D}), and its value depends on the temperature.

4.1.4.1 Critical temperature

We obtain the critical temperature for this intrinsic s-wave superconductor T_c^{in} from Eq. (4.16) by realising that the gap function vanishes $\Delta^{\text{in}}(T) \approx 0$ as $T \to T_c^{\text{in}}$ from below. This way, the gap equation can be linearised.

$$\Delta^{\text{in}}(T_c^{\text{in}}) \approx V \sum_{\mathbf{k}'} \frac{\tanh \frac{\xi_{\mathbf{k}'}}{2k_{\text{B}}T_c^{\text{in}}}}{2\xi_{\mathbf{k}'}} \Delta^{\text{in}}(T_c^{\text{in}}). \tag{4.18}$$

We can cancel out the factor of Δ^{in} on both sides. We further assume that the normal state density of state per spin $N(\xi)$ does not vary much near the Fermi surface, $N(\xi) \approx N(0)$ for $|\xi| \lesssim \epsilon_{\text{D}}$ so that the sum over $\mathbf{k}'$ is turned into an integral

$$1 \approx N(0)V \int_{-\epsilon_{\text{D}}}^{\epsilon_{\text{D}}} \mathrm{d}\xi \, \frac{\tanh \frac{\xi}{2k_{\text{B}}T_c^{\text{in}}}}{2\xi} \approx N(0)V \ln\left(\frac{2\mathrm{e}^{\gamma}}{\pi} \frac{\epsilon_{\text{D}}}{k_{\text{B}}T_c^{\text{in}}}\right), \tag{4.19}$$

where $\gamma \approx 0.577$ is the Euler constant [3], and $2\mathrm{e}^{\gamma}/\pi \approx 1.13$. We rearrange to get

$$T_c^{\text{in}} \approx 1.13 \frac{\epsilon_{\text{D}}}{k_{\text{B}}} \mathrm{e}^{-\frac{1}{N(0)V}}. \tag{4.20}$$

Thus, the critical temperature scales proportionally to the Debye energy and depends exponentially on the inverse of the local attraction strength. This exponential dependence is characteristic of superconductors with local attractive interactions. For conventional superconductors, $N(0)V \lesssim 0.3$, so the exponential factor ensures that the energy scale of the superconducting gap is always much lower than the Debye energy, ϵ_{D}.

4.1.4.2 Zero-temperature gap function

The superconducting gap size grows as the temperature decreases; it is largest in the limit of $T = 0$K, where Eq. (4.16) becomes

$$\Delta^{\mathrm{in}}(T=0) = V \sum_{\mathbf{k}'} \frac{1}{2\sqrt{\xi_{\mathbf{k}}^2 + \left(\Delta^{\mathrm{in}}(T=0)\right)^2}} \Delta^{\mathrm{in}}(T=0). \tag{4.21}$$

We use the same procedure as in the previous part to get

$$\Delta^{\mathrm{in}}(T=0) = \frac{\epsilon_{\mathrm{D}}}{\sinh \frac{1}{N(0)V}} \approx 2\epsilon_{\mathrm{D}} \mathrm{e}^{-\frac{1}{N(0)V}}. \tag{4.22}$$

From the solution to the gap function, we have the dispersion of the Bogoliubov quasiparticles, which can be measured with ARPES [139]. In Fig. 4.1(a), we plot the zero-temperature dispersion of the quasiparticles. A gap is clearly visible. The gap size can also be measured in electron tunnelling experiments [140], which probes the quasiparticle density of state, $2g(E)$ as a function of energy E. The factor of 2 comes from two species of Bogoliubov quasiparticles (analogous of spin-up and spin-down electrons). Assuming again that the normal state density of state does not vary much close to the Fermi surface, we have

$$g(E)/N(0) = \begin{cases} \frac{E}{\sqrt{E^2 - (\Delta^{\mathrm{in}})^2}}, & \text{for } E > \Delta^{\mathrm{in}} \\ 0 & \text{otherwise.} \end{cases} \tag{4.23}$$

We plot this in Fig. 4.1(b). $g(E)$ has a square root divergence close to the superconducting gap [3].

4.2 Anderson's pseudospin representation

The BCS mean-field theory can be reformulated such that the electronic state and the mean fields are represented respectively by pseudospins and pseudofields [141] that are more visual.

As it is best to illustrate this with an example, we take the s-wave electron-phonon superconductor we studied above and look at it through the pseudospin formalism.

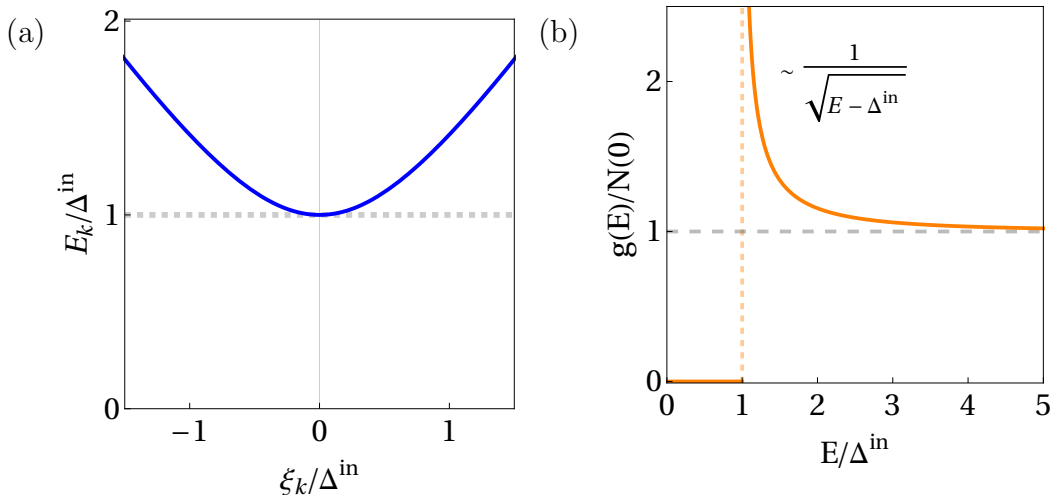


Figure 4.1: (a) The dispersion of Bogoliubov quasiparticle excitations normalised by the gap size. (b) Quasiparticle density of state normalised by the normal state density of state at the Fermi surface. Instead of plotting the dispersion in the usual way, i.e., $E_{\mathbf{k}}$ against $\mathbf{k}$, in (a), we rescale the x-axis by the Fermi velocity so the x-axis shows $\xi_{\mathbf{k}}$ instead. Both $\xi_{\mathbf{k}}$ and $E_{\mathbf{k}}$ are rescaled by the gap size.

4.2.1 Example cont'd: s-wave electron-phonon superconductivity

For a singlet superconductor, the components of the pseudospins in the pseudospin formalism are defined as follow,

$$S^z_{\mathbf{k}} = (c^\dagger_{\mathbf{k},\uparrow} c_{\mathbf{k},\uparrow} + c^\dagger_{-\mathbf{k},\downarrow} c_{-\mathbf{k},\downarrow} - 1)/2 \tag{4.24a}$$

$$S^+_{\mathbf{k}} = c^\dagger_{\mathbf{k},\uparrow} c^\dagger_{-\mathbf{k},\downarrow} \tag{4.24b}$$

$$S^-_{\mathbf{k}} = c_{-\mathbf{k},\downarrow} c_{\mathbf{k},\uparrow}. \tag{4.24c}$$

We see that the z-component of the pseudospin refers to the occupancy of a pair of single-electron states: it points up for an occupied pair of states, and down otherwise. The spin ladder operators represent pair creation and annihilation. The z-component of the pseudofield is given by the electron dispersion, and the x- and y-components correspond to the BCS mean-fields [see Eq. (4.2)]. Therefore, given the local interaction defined in Eq. (4.15), the pseudofield is defined as

$$\mathbf{B}_{\mathbf{k}} = -2\xi_{\mathbf{k}} \mathbf{e}_z + 2 \sum_{\mathbf{k}'} V \langle \mathbf{S}^\perp_{\mathbf{k}'} \rangle, \tag{4.25}$$

where $\mathbf{S}^\perp_{\mathbf{k}}$ refers to the component of $\mathbf{S}_{\mathbf{k}}$ in the xy-plane. The mean-field Hamiltonian is, therefore,

$$H_{\text{MF}} = -\sum_{\mathbf{k}} \mathbf{B}_{\mathbf{k}} \cdot \mathbf{S}_{\mathbf{k}}. \tag{4.26}$$

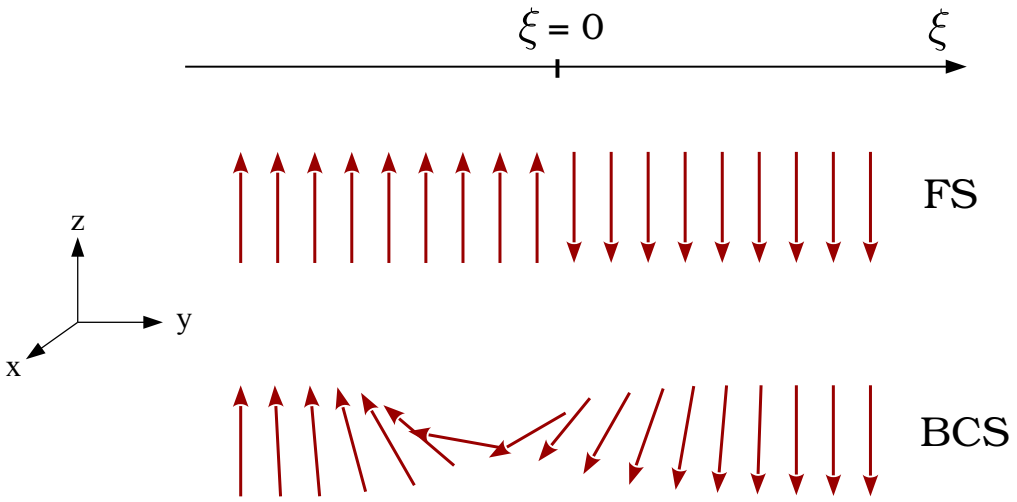


Figure 4.2: Sketches of the pseudospins for a Fermi sea and a BCS ground state. We

In the ground state, the pseudospins are aligned with $\mathbf{B}_\mathbf{k}$. Without loss of generality, we assume that the ground state pseudofield, $\mathbf{B}^0_\mathbf{k}$, lies in the xz-plane,

$$\mathbf{B}^0_\mathbf{k} = -2\xi_\mathbf{k}\mathbf{e}_z + 2\mathbf{e}_x\Delta^{\text{in}}(T=0), \tag{4.27}$$

and the self-consistency equation for $\Delta^{\text{in}}(T=0)$ is

$$\Delta^{\text{in}}(T=0) = \sum_{\mathbf{k}'} V\langle \mathbf{S}^\perp_{\mathbf{k}'}\rangle = \sum_{\mathbf{k}'} V \frac{\Delta^{\text{in}}(T=0)}{2\sqrt{\xi^2_{\mathbf{k}'} + \left(\Delta^{\text{in}}(T=0)\right)^2}}, \tag{4.28}$$

which is the zero-temperature gap equation that we have seen in Eq. (4.21).

Fig. 4.2 gives a visualisation of the BCS ground state compared with the Fermi sea represented by the pseudospins. For the Fermi sea, the pseudospins all point in the $+z$-direction below the Fermi surface and oppositely above the Fermi surface. This indicates that only states below the Fermi surface are occupied. In contrast, the BCS state shows a gradual twist within the xz-plane as we move across the Fermi surface. The pseudospins near the Fermi surface have greater projections in the x-direction, indicating that the Cooper instability is strongest closest to the Fermi surface.

In this picture, a pair of quasiparticle excitations corresponds to a pseudospin-flip. Flipping one $\mathbf{S}_\mathbf{k}$ costs $|\mathbf{B}^0_\mathbf{k}| = 2E_\mathbf{k}$ of energy as expected. On the other hand, collective excitations on top of the ground state are represented by collective precessions of the pseudospins. We study them in the section below by considering the equation of motion of the pseudospins.

4.2.1.1 Collective modes

We obtain the equation of motion for $\mathbf{S_k}$ from Eq. (4.26),

$$\hbar \frac{\mathrm{d}\mathbf{S_k}}{\mathrm{d}t} = \mathbf{S_k} \times \mathbf{B_k}. \tag{4.29}$$

To study the collective modes on top of the ground state, we consider a small perturbation $\delta\mathbf{S_k} = \mathbf{S_k} - \mathbf{S_k^0}$ of the ground state pseudospin alignment. Its time evolution is given by

$$\hbar \frac{\mathrm{d}\delta\mathbf{S_k}}{\mathrm{d}t} = \delta\mathbf{S_k} \times \mathbf{B_k^0} + \mathbf{S_k} \times \delta\mathbf{B_k}, \tag{4.30}$$

where $\delta\mathbf{B_k} = \mathbf{B_k} - \mathbf{B_k^0}$. This is obtained through linearising Eq. (4.29).

To solve for the collective excitations, we take the Fourier transform of Eq. (4.30), and re-formulate it as an eigenvalue problem:

$$\begin{aligned}(\hbar\omega)^2 \phi_{\mathbf{k}} &= \sum_{\mathbf{k}'} \mathcal{M}_{\mathbf{k}\mathbf{k}'} \phi_{\mathbf{k}'} \\ &= \left(B_{\mathbf{k}}^0\right)^2 \phi_{\mathbf{k}} - B_{\mathbf{k}}^0 \sum_{\mathbf{k}'} V \phi_{\mathbf{k}'} - \cos\theta_{\mathbf{k}} \sum_{\mathbf{k}'} V B_{\mathbf{k}'}^0 \cos\theta_{\mathbf{k}'} \phi_{\mathbf{k}'} \\ &\quad + \cos\theta_{\mathbf{k}} \sum_{\mathbf{k}',\mathbf{k}''} V^2 \cos\theta_{\mathbf{k}'} \phi_{\mathbf{k}''},\end{aligned} \tag{4.31}$$

where $S_{\mathbf{k}}^y \propto \phi_{\mathbf{k}}$, $\tan\theta_{\mathbf{k}} = -\Delta^{\mathrm{in}}(T=0)/\xi_{\mathbf{k}}$, and $B_{\mathbf{k}}^0 = |\mathbf{B}_{\mathbf{k}}^0|$.

From the equation above, we see that properties of the collective modes of the superconductor depends on the interactions present. In the current model with only local attractions, the Nambu-Goldstone mode and the Higgs mode are solutions to the eigenvalue problem.

Before we continue with microscopic form of the collective modes within the pseudospin formalism, let us first describe what these collective modes are. To this end, the Laudau-Ginzburg theory perspective, where the superconducting gap Δ^{in} translates into the complex order parameter Ψ, offer a clearer picture. In Landau-Ginzburg theory, the free energy functional (without external static magnetic field) has the following form which satisfies particle-hole symmetry of the superconductor [142]

$$f = f_0 + a|\Psi(\mathbf{r})|^2 + b|\Psi(\mathbf{r})|^4 + \frac{1}{2m^*}|(-\mathrm{i}\boldsymbol{\nabla} - e^*\mathbf{A}(\mathbf{r})\Psi(\mathbf{r})|^2, \tag{4.32}$$

where $a < 0$ for $T < T_c$, $b > 0$ is some constant, and m^* and e^* are the effective mass and effective charge of the Cooper pair. We have given the order parameter an additional spatial degree of freedom that is linked to the centre of mass position of the Cooper pairs, though in this thesis we only focus on the long-wavelength, i.e., the zero

centre-of-mass-momentum limit. $\mathbf{A}$ is the vector potential of the electromagnetic field coupled to the Cooper pairs. When $T < T_c$ (and without spatial homogeneity and external driving), the system lowers its free energy by spontaneous $U(1)$ symmetry breaking: $\Psi(r) = \Psi_0 = |\Psi_0|\mathrm{e}^{\mathrm{i}\phi_0}$. The amplitude of the order parameter is lined to the density of the superconducting condensate, i.e., $|\Psi(\mathbf{r})|^2 = n_s(\mathbf{r})$, and phase is arbitrarily chosen as its choice (as long as it is a constant) does not impact the free energy. Linking with our microscopic theory discussion, choosing Δ^{in} to be real is the same as setting $\phi_0 = 0$.

The Nambu-Goldstone mode and the Higgs mode refer to the oscillation of the phase ϕ and amplitude $|\Psi|$ around their equilibrium values, ϕ_0 and $|\Psi_0|$ respectively. Let's denote them as $\theta(\mathbf{r})$ and $H(\mathbf{r})$ such that (after setting $\phi_0 = 0$, $\Psi(r) = [\Psi_0 + H(\mathbf{r})]\mathrm{e}^{i\theta}$. At this stage, we can already see that the Higgs mode has the same symmetry as the superconducting gap (s-wave in this case) and we can interpret the Higgs mode physically as modulation of the superconducting condensate density.

The change in free energy due to H and θ is

$$-aH(\mathbf{r})^2 + \frac{1}{2m^*}[\boldsymbol{\nabla} H(\mathbf{r})]^2 + \frac{(e^*)^2}{2m^*}[\mathbf{A} - \frac{1}{e^*}\boldsymbol{\nabla}\theta(\mathbf{r})]^2[\Psi_0 + H(\mathbf{r})]^2. \tag{4.33}$$

Recall that we can carry out a gauge transformation without changing the physics, a transformation on the vector potential $\mathbf{A} \to \mathbf{A} - \frac{1}{e^*}\boldsymbol{\nabla}\theta$ let the phase mode be absorbed into the longitudinal component of the electromagnetic field, hence the oscillations of θ manifest as plasma oscillations which can be excited by electron density perturbations as described in Chapter. 2. This is the Anderson-Higgs mechanism [143, 144]. In 3D, the plasma frequency is gapped and far above the superconducting gap. However, as we have seen in earlier chapters, the plasma frequency is not gapped in 2D (it has a square-root dispersion), and long wavelength plasmons can appear inside the superconducting gap [145]. This has indeed been observed in thin film $YBa_2Cu_3O_7$ [146]. After the gauge transformation, the last term in Eq. (4.33) gives the leading order coupling between the Higgs mode and the electromagnetic field $\frac{(e^*)^2}{m^*}\Psi_0\mathbf{A}^2H(\mathbf{r})$. This means that the Higgs mode only couples to light quadratically. The lack of linear coupling is due to particle-hole symmetry which makes the Higgs a charge neutral excitation. The Higgs' quadratic coupling to light means that it can be excited by strong periodic driving at half of its resonance [147] or Raman processes in which the incident and scattered photon polarizations are the same such that the s-wave symmetry is selected [148]. The electronic part of the operator that excites the Higgs mode has the form $\sum_{\mathbf{k}} \gamma_{\mathbf{k}}(c^\dagger_{\mathbf{k}+\mathbf{q}\uparrow}c^\dagger_{-\mathbf{k}+\mathbf{q}\downarrow}c_{-\mathbf{k}\downarrow}c_{\mathbf{k}\uparrow} + c^\dagger_{\mathbf{k}\uparrow}c^\dagger_{-\mathbf{k}\downarrow}c_{-\mathbf{k}-\mathbf{q}\downarrow}c_{\mathbf{k}-\mathbf{q}\uparrow})$, where $\gamma_{\mathbf{k}}$ obeys the symmetry of the superconducting gap, s-wave in this case.

Having described the Nambu-Goldstone mode and the Higgs mode, we can continue with the pseudospin perspective. The Nambu-Goldstone mode is given by $\phi_{\mathbf{k}} \propto |\sin\theta_{\mathbf{k}}|$. It arises due to the spontaneous $U(1)$ symmetry breaking when we choose the ground state pseudospins to lie in the xz-plane. This choice means $\Delta^{\text{in}}(T=0)$ is real. Had we chosen a different angle to the x-axis, $\Delta^{\text{in}}(T=0)$ would gain unitary a phase. The Nambu-Goldstone mode corresponds to variations of this phase, hence it is also commonly referred to as the phase mode. By inserting the form of $\phi_{\mathbf{k}}$ into Eq. (4.31), we see that this mode has zero energy as predicted by Goldstone's theorem [149]. However, once we include the coupling to electromagnetic fields, this mode is absorbed into the fields and manifest as plasma oscillations through the Anderson-Higgs mechanism [143, 144]. We will see in the next chapter that this mode is unaffected by the introduction of the long-range interactions.

The Higgs mode in this superconductor is given by $\phi_{\mathbf{k}} \propto \sin\theta_{\mathbf{k}} \tan\theta_{\mathbf{k}}$. It represents amplitude oscillations of $\Delta^{\text{in}}(T=0)$ which is perpendicular to the phase mode. The energy of the Higgs mode is $2\Delta^{\text{in}}(T=0)$, i.e., it is exactly on the edge of the quasiparticle excitation continuum. This means that the Higgs mode is unstable, as it can decay via quasiparticle excitations. Even when the temperature is low such that the Higgs mode is decoupled from the NG mode, thanks to the (approximate) particle-hole symmetry, the Higgs mode decay as $t^{-\frac{1}{2}}$ [150]. Here t denotes time. Together with the lack of linear coupling to light [142, 151], Higgs modes are difficult to observe experimentally. The weak coupling to light can be overcome by using intense terahertz (THz) light sources to couple quadratically, like in Ref. [152, 147, 153, 154], cryogenic near-field nano-optics [155], or Raman spectroscopy [156, 157, 158]. However, they do not resolve the difficulty associated with decay of the Higgs mode. So far, there are only two demonstrated exceptions where the Higgs mode in a superconductor is stable against decay through quasiparticle excitations. One of them is found in charge-density-wave superconductors [156, 157, 158], the other is found in strongly disordered superconductors [159]. In both cases, the energy of Higgs mode is below the superconducting gap so it cannot decay via quasiparticle excitations. We show in the next chapter that long-range interactions present another way to prevent the decay of the Higgs mode.

4.3 Conclusion

We have reviewed BCS theory of superconductivity and its representation in Anderson's pseudospin formalism. We have applied it to the classic example of a conven-

tional s-wave superconductor which only has local interactions (typically mediated by phonons). Specifically, we have shown how to calculate the critical temperature and the zero-temperature gap function. We have also discussed quasiparticle and collective excitations above the ground state. Importantly, we have learnt that the Higgs mode energy in this superconductor is on the edge of the quasiparticle excitation continuum. As a result, the Higgs is unstable against decay through the quasiparticles.

In the next chapter, we show a system in which the Higgs mode is stable without disorder or charge-density wave. We take advantage of the induced long-range interactions in the driven cavity setup discussed in the previous chapter, and show how the long-range nature of the induced interactions can qualitatively alter the properties of the conventional BCS superconductor discussed in this chapter.

Chapter 5

Higgs mode stabilization by photo-induced long-range interactions in a superconductor

Most of the results presented in this chapter were in the article H. Gao, F. Schlawin, and D. Jaksch, Higgs mode stabilization by photo-induced long-range interactions in a superconductor, *Phys. Rev. B* **104**, L140503 (2021). HG performed all the calculations and made substantial contributions to the manuscript.

In Chapter. 3, we introduced a method to induce long-range, essentially unscreened, density-density interactions between electrons in a range of two-dimensional materials. In this chapter, we consider using long-range interactions to manipulate BCS superconductors, with a focus on the low-lying excitations. It is worth noting that long-range nature of the interaction is characteristic of involvement of cavity field. For instance, cavity enhancement of electron-phonon interactions is only strong for forward scattering (i.e., small momentum transfer), thus the enhanced electron interactions are also long-ranged [53, 160]. For this reason, though the setup we consider in this chapter is based on the driven cavity setup introduced in Chapter. 3, the results could be more generally applicable to other setups involving cavities or system where long-range interactions are present.

Low-lying excitations in quantum systems are important as they play a major role in determining the macroscopic orders and the microscopic dynamics. Superconductors, in particular, host a range of quasiparticle and collective excitations. We have seen in the previous chapter that the Bogoliubov quasiparticle excitations in a conventional superconductor determine its superconducting critical temperature. The low-lying excitations also dictate electromagnetic responses [161, 151] and topological order [162, 163], carry information on the ground state gap properties

[164, 165], as well as govern the out-of-equilibrium dynamics of the superconductors [166, 167, 168, 152, 147, 169, 170, 153].

In additional to the Nambu-Goldstone mode, that manifests as plasma oscillations, and the usually damped Higgs mode, which we have introduced in the previous chapter, superconductors with more complicated interactions exhibit another type of collective excitations termed excitonic/Bardasis-Schrieffer (BS) modes [171]. They are fluctuations of superconducting order parameters in the subdominant channels [172, 151]. For s-wave superconductors, these modes appear because of the Cooper pair excitations from s-wave pair bound state to higher angular momentum bound states, usually a d-wave bound state. Excitonic modes are stable collective excitations with energies below the quasiparticle excitation continuum and decreasing to zero as the subdominant pairing strengths approach the dominant one.

The excitonic and, to an even larger extent, the Higgs modes have received considerable interest since their theoretical predictions. The interest not only stems from their direct link to spontaneous symmetry breaking, but is also due to the fact that measurements on them can reveal ground state gap symmetry and multiplicity [165, 164], couplings to other collective modes [173], and information on the electronic interactions present [174, 175, 176, 177]. However, these collective modes have proven to be rather elusive to experimental detection. This is partly due to the fact that they don't couple strongly to the electromagnetic fields [151]: particle-hole symmetry prevents linear coupling to the Higgs mode [142, 178], while the lack of a dipole moment and the optical selection rules forbids far-field optical excitations of the excitonic modes [151]. Theories have suggested inducing linear coupling by applying supercurrent [172, 179], or detecting these modes with cryogenic near-field nano-optics [155, 180, 181, 182, 183].

Aside from the issue of weak coupling to light, the excitonic modes, though stable, also require a strong subdominant order to be well-separated from the continuum. As a result, they have been detected only recently by Raman spectroscopy in iron-based superconductors [175, 176, 177].

For the Higgs mode, whose energy, as we have seen in the previous chapter, lies on the edge of the quasiparticle continuum, there is the difficulty that it usually decays rapidly through quasiparticle excitations. This happens even in the low temperature limit where the electron relaxation is much slower than the dynamics of the superconductor [150, 184]. So far, exceptions to this have been found only in superconductors with strong disorder [159] or charge-density wave (CDW) superconductors

[156, 157, 158]. In both cases, the Higgs mode energies are "pushed" in gap, and thus the modes become much more stable [185, 186, 187, 188, 184, 189].

In this chapter, we show that long-range electron interactions in the superconductors present a way to manipulate these low-lying excitations and, in particular, to stabilise the Higgs mode. This proposal leverages the scheme to induce long-range, density-density electron interactions, which we explained in Chapter. 3. By choosing the laser to be red-detuned from the cavity resonance, we engineer long-range electron attractions on top of the intrinsic local attractions in a 2D BCS superconductor, which, for simplicity, we choose to be s-wave.

We show using BCS theory that the long-range interactions enlarges the superconducting gap and enhances the superconducting critical temperature. By studying the fluctuations on top of the BCS ground state using Anderson's pseudospin formalism, we show that the long-range nature of the induced interactions qualitatively affects the collective excitations in the superconductor. We show that the induced long-range attractions allow for excitonic modes in the s-wave superconductors without competing superconducting orders intrinsically. More generally, this means that the long-range attractions can enlarge the separation in energy between the quasiparticle continuum and all excitonic modes intrinsically present in the superconductor.

More importantly, the Higgs mode is pushed "in gap" by the long-range interactions; and the separation of its energy from the quasiparticle continuum depends linearly on the driving intensity. As a result, the Higgs mode no longer decays through the quasiparticle excitations and has a much longer lifetime, which makes it easier to detect regardless of the experimental method [189]. We demonstrate the Higgs mode stabilisation with numerical simulations, comparing the oscillations of the superconducting gap with and without the long-range interactions following an initial excitation of the Higgs mode. Our work presents a novel mechanism for the stabilisation of the Higgs mode, of which there are only a couple of known alternatives.

5.1 Setup

We consider the setup shown in Fig. 5.1(a), which closely resembles the setup considered in Chapter. 3 Fig. 3.1(a). The sole difference is that instead of a weakly interacting electron gas, the driving and the cavity are coupled to a 2D superconductor lies in the xy-plane inside a substrate material with relative permittivity ϵ_r. The laser frequency $\omega_L = \omega_c - \delta_c$ is red-detuned from the cavity resonance, ω_c, (i.e., $\delta > 0$) to induce attractive interactions. We require the driving and cavity frequencies to be

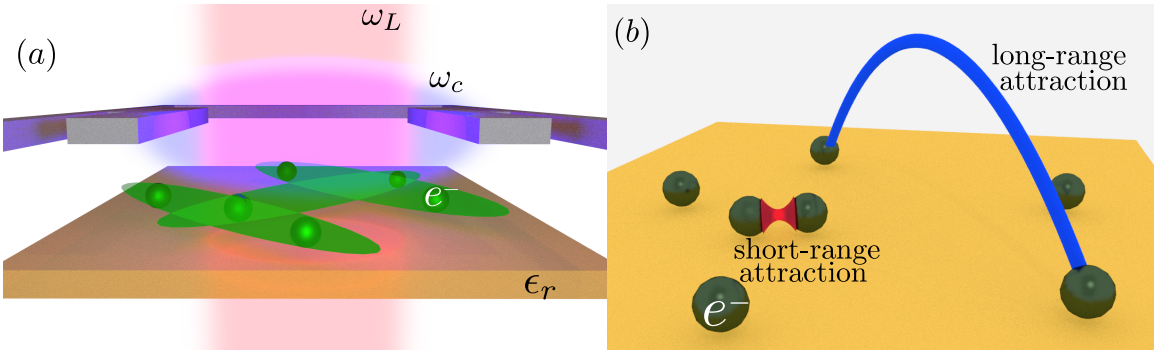


Figure 5.1: (a) Setup: electrons (spheres) in a 2D BCS superconductor (the green envelopes represent Cooper pairing) are evanescently coupled to a complementary split-ring cavity (the gray structure on top) [49]. The blue shading symbolizes the cavity field. The coupled system is driven by a laser field (schematically shown by the red shading) with wavevector $\mathbf{q}_L$ in the vertical direction and frequency ω_L red-detuned from the cavity frequency ω_c. This setup closely resembles Fig. 3.1(a). (b) The coupling to the cavity and the driving fields results in long-range attractive interactions (blue arc) being induced on top of preexisting short-range attractions (red link).

off-resonant from all transitions in the material and the substrate to minimise heating [190] (also see Appendix. B).

5.2 Model

In the Coulomb gauge, our BCS superconductor with local attractive interactions is described by

$$H_{\text{mat}} = \sum_{\mathbf{k},\sigma} \xi_{\mathbf{k}} c^\dagger_{\mathbf{k},\sigma} c_{\mathbf{k},\sigma} - \frac{V}{\mathcal{S}} \sum_{\mathbf{k}_1,\mathbf{k}_2,\mathbf{k}_3} c^\dagger_{\mathbf{k}_1\uparrow} c^\dagger_{\mathbf{k}_2\downarrow} c_{\mathbf{k}_3\downarrow} c_{\mathbf{k}_1+\mathbf{k}_2-\mathbf{k}_3\uparrow}, \tag{5.1}$$

where $\xi_{\mathbf{k}}$ is the dispersion measured from the chemical potential μ of an electron in quasimomentum state $\mathbf{k}$, which can be populated with a spin-σ electron by the action of $c^\dagger_{\mathbf{k},\sigma}$. $\mathcal{S}$ is the area as defined in Chapter. 3. For simplicity, we assume that the dispersion is rotational symmetric (i.e., it depends only on $|\mathbf{k}|$). $V > 0$ and is independent of $\mathbf{k}$, because the superconductor intrinsically has local attractive interactions. We also assume the usual cutoff energy for these interactions, ϵ_{D}, which, in the case of phonon-mediated superconductivity, is identified with the Debye energy.

In Chapter. 3, we have established that the coupling of the electrons to the cavity and the driving fields induces effective long-range density-density interactions between the electrons that are essentially unscreened. Moreover, we have shown that the

direct heating of the electrons in this setup is insignificant. In this work, we thus take an approach similar to that in Ref. [83] and model the effect of the cavity and the driving by the effective interaction Hamiltonian obtained from a Schrieffer-Wolff transformation [see Eq. (3.9)], $H_{\text{long}} = -\sum_{\mathbf{k}_1,\mathbf{k}_2,\mathbf{q}} U_{\mathbf{q}}/\mathcal{S} \quad c^\dagger_{\mathbf{k}_1+\mathbf{q},\uparrow} c^\dagger_{\mathbf{k}_2-\mathbf{q},\downarrow} c_{\mathbf{k}_2,\downarrow} c_{\mathbf{k}_1,\uparrow}$, where

$$\frac{U_{\mathbf{q}}}{\mathcal{S}} = \frac{\alpha^2\hbar^2}{\pi c^2 m^2} \frac{\omega_c^2}{\omega_L^2} \frac{I_{\text{d}}}{\Lambda\delta_c} \delta_{\pm\mathbf{q},q_0\mathbf{e}_x}. \tag{5.2}$$

We highlight the important features of the interactions considered here: they are stronger for higher driving intensities and smaller detunings; however, $\hbar\delta_c$ must be greater than relevant energy scales of the superconductor (the cavity-coupled plasmon energy discussed in Chapter. 3, and the superconducting gap size [190]) for us to ignore retardation in the induced interactions.

In the following, we show the enhancement of the BCS superconducting critical temperature by the long-range interactions before going on to study the zero-temperature properties of the model. For notational simplicity, we set the Boltzmann constant $k_B = 1$ and $\hbar = 1$ from here on.

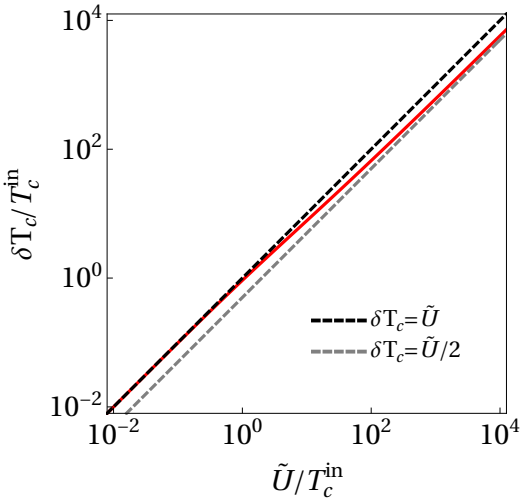


Figure 5.2: (Red solid line) Ratio of enhancement of the critical temperature as a function of the long-range interaction strength. The black and gray dashed lines represent the asymptotic behaviours in the limit of weak and strong long-range interactions respectively.

5.3 Critical temperature enhancement

Like we discussed in Chapter. 4, through the usual BCS reduction and mean-field (MF) decoupling of the interaction terms of the full system ($H_{\text{mat}} + H_{\text{long}}$), we obtain

a gap equation,

$$\Delta_{\mathbf{k}} = \frac{V}{\mathcal{S}} \sum_{\mathbf{k}'} \frac{\Delta_{\mathbf{k}'}}{2E_{\mathbf{k}'}} \tanh\left(\frac{E_{\mathbf{k}'}}{2T}\right) + \tilde{U} \frac{\Delta_{\mathbf{k}}}{E_{\mathbf{k}}} \tanh\left(\frac{E_{\mathbf{k}}}{2T}\right), \tag{5.3}$$

where $\tilde{V} = V/\mathcal{S}$, and $E_{\mathbf{k}} = \sqrt{\xi_{\mathbf{k}}^2 + \Delta_{\mathbf{k}}^2}$ gives the Bogoliubov quasiparticle dispersion, which is measurable with ARPES [139]. $\tilde{U} = U_{q_0 \mathbf{e}_x}/\mathcal{S}$ and $\Delta_{\mathbf{k}} \equiv \sum_{\mathbf{k}'} (\tilde{V} + 2\tilde{U}\delta_{\mathbf{k},\mathbf{k}'}) \langle c_{-\mathbf{k}'\downarrow} c_{\mathbf{k}'\uparrow} \rangle$ defines the MF. We note that we have also taken the $q_0 \to 0$ limit of $U_{\mathbf{q}}$ in the MF definition and in the gap equation Eq. (5.3) [126]. As described in Chapter. 4, the critical temperature is calculated by solving the gap equation after setting the gap to infinitesimal. Using the gap equation with gap function being infinitesimal, we further obtain an approximate relationship (see Appendix. C) between the superconducting critical temperature in the presence of the long-range interactions, T_c, and the intrinsic critical temperature of the superconductor itself $T_c^{\text{in}} \approx 1.13\hbar\omega_{\text{D}} \text{e}^{-1/N(0)V}$ [again, $N(0)$ is the electron density of states at the Fermi level] [87, 191],

$$\frac{1}{T_c^{\text{in}}} \approx \frac{2}{2T_c - \tilde{U}} \exp\Big[\frac{\tilde{U}}{2T_c - \tilde{U}}\Big]. \tag{5.4}$$

This equation embodies the nonlinear fashion in which the long-range interactions combine with the local attractions. We note that Eq. (5.4) is an implicit equation for T_c, and it is guaranteed that $2T_c > \tilde{U}$. In fact, $2T_c = \tilde{U}$ would be the BCS theory prediction if we had a 2D electron gas rather than a superconductor. This scenario is captured in the right half of Fig. 5.2. According to Eq. (5.4), we remark that, firstly, the absolute enhancement of the critical temperature $\delta T_c = T_c - T_c^{\text{in}}$ only depends on T_c^{in} and $\tilde{U}$, which embodies how strong the external driving is; and secondly, that the ratio of $\delta T_c/T_c^{\text{in}}$ depends only on the dimensionless parameter $\tilde{U}/T_c^{\text{in}}$. We plot the latter dependence in Fig. 5.2. We see that when $\tilde{U}/T_c^{\text{in}} < 1$, i.e. the short-range attractions dominate, $\delta T_c \approx \tilde{U}$. This starts to change when $\tilde{U}/T_c^{\text{in}} > 1$ and the long-range interactions dominate. As $\tilde{U}/T_c^{\text{in}} \to \infty$, $\delta T_c \to \tilde{U}/2$. The approximately linear dependence of δT_c on the induced interaction strength $\tilde{U}$ is characteristic of interactions that are long-range [192, 53]. The change in behaviour in the two limiting cases in Fig. 5.2 highlights the nonlinear effect of combining cavity-mediated long-range interactions with a material's intrinsic short-range interactions. An implication of this is that long-range attractions are twice better at enhancing superconductivity caused by short-range, as opposed to long-range, attractions.

In Appendix. C, we see that with realistic driving and cavity parameters the critical temperature could be enhanced by as much as five times for superconductors

with low T_c^{in}'s, such as overdoped (by gating) lanthanum aluminate-strontium titanate interface (LAO/STO) with $T_c^{\text{in}} \lesssim 200$mK [193]. However, the absolute enhancement of T_c due to the long-range interactions is limited to about 1K. Thus, experiments documented in [52] showing a 15K increase in the critical temperature is unlikely to be explained by a mechanism similar to ours.

5.4 Zero-temperature gap structure

As we have seen in Chapter. 4, the gap function, $\Delta_{\mathbf{k}}$, in a homogeneous s-wave BCS superconductor with only local electron attractions is a constant in k-space. This changes when the long-range interactions are present.

We obtain the zero-temperature gap function by solving the gap equation evaluated at $T = 0$K,

$$\Delta_{\mathbf{k}} = \tilde{V} \sum_{\mathbf{k}'} \frac{\Delta_{\mathbf{k}'}}{2E_{\mathbf{k}'}} + \tilde{U} \frac{\Delta_{\mathbf{k}}}{E_{\mathbf{k}}}. \tag{5.5}$$

We show in Fig. 5.3(a) the zero-temperature gap functions in the radial direction around the Fermi surface with and without the induced long-range attractive interactions. Recall from our example in Chapter. 4 that the gap function of a usual BCS s-wave superconductor with only local electron attraction, the gap function $\Delta^{\text{in}} = 2\epsilon_{\text{D}} \exp\{-1/N(0)V\}$ is a constant in k-space. In contrast, in Fig. 5.3(a) we see that the presence of the long-range interactions causes the gap function to gain a structure in the radial direction. As for the azimuthal direction, the rotational symmetry of the electron dispersion ensures that the s-wave gap function has rotational symmetry in k-space. The gap is greatest at the (original) Fermi surface and flattens out further away ($|\xi_{\mathbf{k}}| \gtrsim \Delta_{k_F}^{T=0}$) from the Fermi surface. Importantly, the gap is larger everywhere in the presence of the long-range attractive interactions. In fact, for $\tilde{U} \ll \Delta^{\text{in}}$, the gap increases linearly with $\tilde{U}$:

$$\Delta_{\mathbf{k}}^{T=0} = \Delta^{\text{in}} + \left(\frac{\pi}{4} + \frac{\Delta^{\text{in}}}{\sqrt{(\Delta^{\text{in}})^2 + \xi_{\mathbf{k}}^2}} \right) \tilde{U}, \tag{5.6}$$

where Δ^{in} is the gap size in the absence of the long-range interactions. This is in contrast to the case of superconductors with long-range interactions only [194]. There, the gap function vanishes away from the Fermi surface ($|\xi_{\mathbf{k}}| > \tilde{U}$), where the gap size is $\tilde{U}$. The fact that in our system the gap size enhancement at $|\mathbf{k}| = k_F$ is greater than $\tilde{U}$ highlights that the long-range interactions combine with the local interactions nonlinearly.

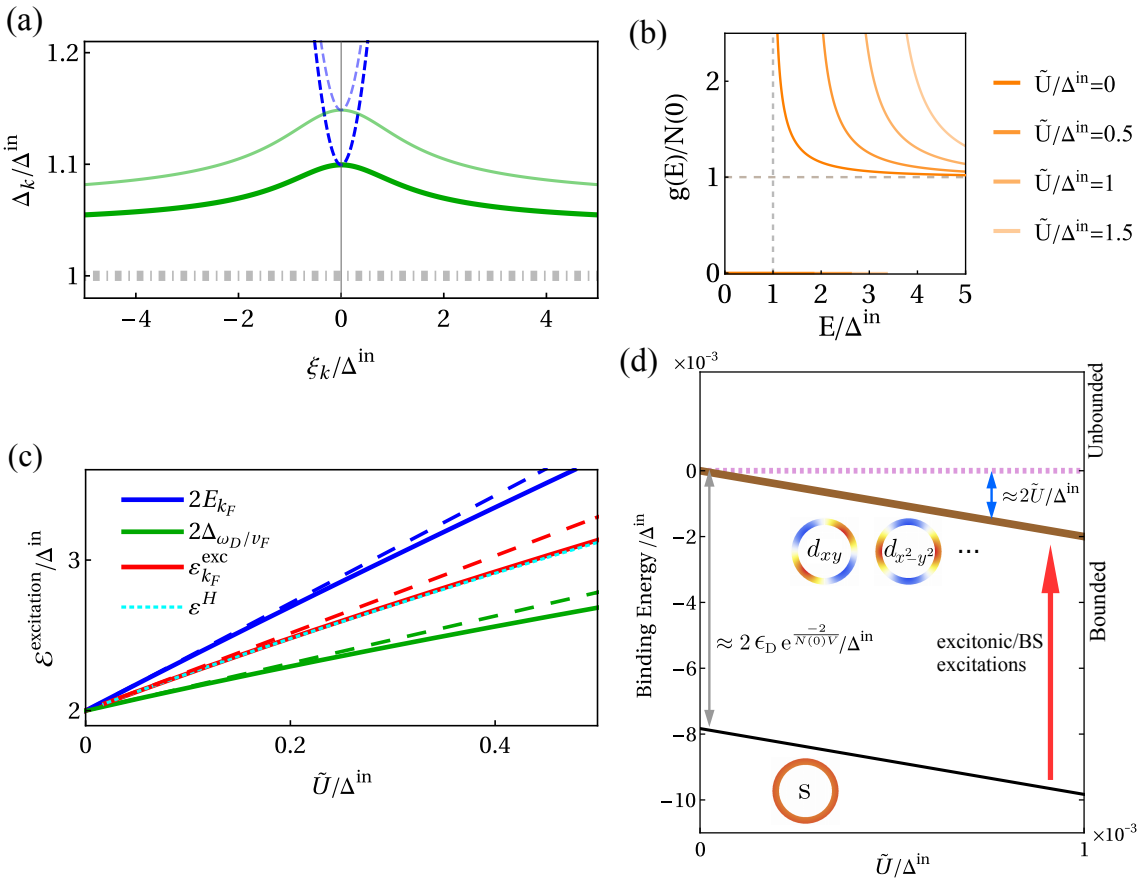


Figure 5.3: (a) The zero-temperature gap functions with two different long-range-interaction strengths are plotted along the radial direction in k-space with green lines. The x-axis is rescaled like in Fig. 4.1(a). Bogoliubov quasiparticle excitation energies for the system are plotted with dashed blue lines. The solid(semitransparent) lines use $\tilde{U}/\Delta^{\rm in} \approx 0.056 (\tilde{U}/\Delta^{\rm in} \approx 0.085)$. The gap function without the long-range interactions is plotted with a gray dash-dotted line. (b) Quasiparticle density of state evaluated at zero temperature for various values of $\tilde{U}/\Delta^{\rm in}$. (c) We plot the values of the various excitation energies of the system against $\tilde{U}$ with the solid lines. The dashed lines give the linear dependence of the corresponding energies on $\tilde{U}$ obtained from first-order perturbation theory. Note that $\varepsilon^{\rm H} < \varepsilon^{\rm exc}_{k_F}$ for finite $\tilde{U}$, but they are equal up to $\mathcal{O}(\tilde{U})$. The results are calculated for $T = 0$K. In (a)-(c) we have used $\epsilon_{\rm D}/\Delta^{\rm in} = 113$. (d) An energy diagram showing the electron-pair binding energy (from considering the Cooper problem) as a function of the long-range interaction strength. Without the long-range interactions (at $\tilde{U}/\Delta^{\rm in} = 0$), there is only one two-electron bound state in the s-wave channel. The long-range interactions increase all binding energies by $\approx 2\tilde{U}$ such that states with higher angular momenta (e.g., d-wave) become bound states. The Cooper pair condensate is still in the s-wave channel but Cooper pairs can be excited to higher energy bound states to excite excitonic (a.k.a. Bardasis-Schrieffer) modes.

The enlargement of the gap function implies that the Bogoliubov quasiparticle excitation continuum is "pushed" to higher energies. This is reflected in the quasiparticle density of state plotted in Fig. 5.3(b), which could be probed with electron tunneling experiments [140]. This increase of the gap size reflects the enhancement of BCS critical temperature discussed in the previous section. The mechanism at play here differs from the Eliashberg effect [56, 57, 58] and its quantum equivalent [55], which dynamically enhance the gap close to the critical temperature through quasiparticle redistribution [195], whereas in our case, the enhancement extends to zero temperature.

5.5 Collective modes

To study the collective modes at zero centre-of-mass momentum, we go beyond the BCS MF theory, using Anderson's pseudospin representation, which we discussed in the previous chapter. As a reminder, with this approach, the MF Hamiltonian is mapped to a system of pseudospins [see Eq. (4.24) for the definition] interacting with pseudofields [see Eq. (4.25)]; and the collective modes are represented as small pseudospin precessions around the ground state alignment which we fix to lie in the xz-plane without loss of generality. Again, by linearising the equation of motion of the pseudospins, we obtain an eigenvalue equation whose solution gives the collective modes,

$$\begin{aligned}
&\omega^2\phi_{\mathbf{k}} \\
&= \sum_{\mathbf{k}'} \mathcal{M}_{\mathbf{k}\mathbf{k}'}\phi_{\mathbf{k}'} \\
&= \left(B^0_{\mathbf{k}}\right)^2 \phi_{\mathbf{k}} - B^0_{\mathbf{k}} \sum_{\mathbf{k}'} (\tilde{V} + 2\tilde{U}\delta_{\mathbf{k},\mathbf{k}'})\phi_{\mathbf{k}'} \\
&- \cos\theta_{\mathbf{k}} \sum_{\mathbf{k}'} (\tilde{V} + 2\tilde{U}\delta_{\mathbf{k},\mathbf{k}'}) B^0_{\mathbf{k}'} \cos\theta_{\mathbf{k}'}\phi_{\mathbf{k}'} \\
&+ \cos\theta_{\mathbf{k}} \sum_{\mathbf{k}',\mathbf{k}''} (\tilde{V} + 2\tilde{U}\delta_{\mathbf{k},\mathbf{k}'})(\tilde{V} + 2\tilde{U}\delta_{\mathbf{k}',\mathbf{k}''}) \cos\theta_{\mathbf{k}'}\phi_{\mathbf{k}''}. \qquad (5.7)
\end{aligned}$$

The equation above differs from Eq. (4.31) in that the interaction matrix elements for the local interactions in Eq. (4.31) (V) are replaced by the sum of the local and long-range interaction matrix elements ($\tilde{V} + 2\tilde{U}\delta_{\mathbf{k},\mathbf{k}'}$).

We focus on two types of low-lying collective modes, the excitonic/Bardasis-Schrieffer modes and the Higgs mode, in the following.

5.5.1 Excitonic/Bardasis-Schrieffer modes

Unlike in a usual s-wave BCS superconductor, we find that excitonic excitations are supported. Their perturbations $\Phi_k^{\text{exc}} = (..., \phi_{\mathbf{k}}^{\text{exc}}, ...)$ are local in each energy shell. Φ_k^{exc} satisfies $\phi_{\mathbf{k}}^{\text{exc}} = 0 \quad \forall |\mathbf{k}| \neq k$ and $\sum_{|\mathbf{k}|=k} \phi_{\mathbf{k}}^{\text{exc}} = 0$. The energy of the excitonic modes indexed by $\mathbf{k}$ is thus

$$\varepsilon_{\mathbf{k}}^{\text{exc}} = \sqrt{\left(B_{\mathbf{k}}^0\right)^2 - 2B_{\mathbf{k}}^0 \tilde{U}\left(1 + \cos^2\theta_{\mathbf{k}}\right) + 4\tilde{U}^2 \cos^2\theta_{\mathbf{k}}}. \tag{5.8}$$

The energy is lowest on the Fermi surface, $\varepsilon_{k_F}^{\text{exc}} = 2\sqrt{\Delta_{k_F}^2 - \tilde{U}\Delta_{k_F}}$; and we plot this in 5.3(c). We see that the excitonic excitations appear in gap as expected. For $\tilde{U} \ll \Delta^{\text{in}}$, both the Bogoliubov and the excitonic excitation energies increase linearly in $\tilde{U}$. At $|\mathbf{k}| = k_F$,

$$2E_{k_F} \approx 2\Delta^{\text{in}} + (2 + \pi/2)\tilde{U}, \text{ and} \tag{5.9}$$

$$\varepsilon_{k_F}^{\text{exc}} \approx 2\Delta^{\text{in}} + (1 + \pi/2)\tilde{U}. \tag{5.10}$$

This means that the separation in energy between the excitonic excitations and the quasiparticle continuum can be tuned by the intensity of the external laser field. We also highlight that this energy is still higher than twice the superconducting gap without the long-range interactions.

The cause for the appearance of these excitonic excitations can be understood from a discussion of the Cooper problem. In superconductors with only the local attractions, there is only one two-electron bound state in the s-wave channel [3]. This is shown in Fig. 5.3(d) at $\tilde{U}/\Delta^{\text{in}} = 0$. However, as soon as the long-range interactions mediated by the cavity are imposed, more bound states, e.g., in d-wave channels, appear. This is shown on the right of Fig. 5.3(d). We note that the original s-wave state's binding energy also increases due to the long-range interactions, and the s-wave state remains the most tightly bound. Thus, the Cooper pairs still condense in the s-wave state. A Cooper pair from the condensate, whose constituents have quasimomenta $\pm\mathbf{k}$, can now be excited to one of these more loosely bound states as opposed to becoming unbound. In the former case, we have an excitonic excitation with energy $\varepsilon_{\mathbf{k}}^{\text{exc}}$, while in the latter, a pair of quasiparticle excitations are produced, costing $2E_{\mathbf{k}}$ of energy. In superconductors with only local (s-wave) interactions, the electron pairs have no other bound state to scatter into, and thus no excitonic excitations are present. In the opposite limit, where superconductors only have very long-range attractions, many excitonic modes are available, and the least energetic ones amongst them become gapless as the interaction range tends to infinity [194].

Cooper's problem.
The wavefunction of a singlet Cooper pair has the form [3]

$$|\Phi\rangle = \sum_{0<\xi_{\mathbf{k}}<\epsilon_{\mathrm{D}}} g(\mathbf{k}) c^{\dagger}_{\mathbf{k}\uparrow} c^{\dagger}_{-\mathbf{k}\downarrow} |\mathrm{FS}\rangle \,, \tag{5.11}$$

where $|\mathrm{FS}\rangle$ represents the Fermi sea at $T = 0$K. By substituting this into the full system Hamiltonian and take the $q_0 \to 0$ limit, we find that $g(\mathbf{k})$ satisfies

$$E g(\mathbf{k}) = 2\xi_{\mathbf{k}} g(\mathbf{k}) - \sum_{\mathbf{k}'} (\tilde{V} + 2\tilde{U}\delta_{\mathbf{k},\mathbf{k}'}) g(\mathbf{k}'), \tag{5.12}$$

where E is the two-electron state energy. We rearrange the terms to get

$$\left(E - 2\xi_{\mathbf{k}} + 2\tilde{U}\right) g(\mathbf{k}) = \tilde{V} \sum_{\mathbf{k}'} g(\mathbf{k}'), \tag{5.13}$$

where the RHS is independent from $\mathbf{k}$. For the s-wave two-electron state, the RHS is nonzero. We follow the usual procedure of cancelling out common factors from both sides and perform the integration in $\mathbf{k}$-space [3] to obtain the s-wave binding energy

$$E - 2\xi_{\mathbf{k}} \approx -2\tilde{U} - 2\epsilon_{\mathrm{D}} \mathrm{e}^{\frac{-2}{N(0)V}}. \tag{5.14}$$

For the two-electron states with higher angular momenta, the RHS is zero as the intrinsic attraction has no component in any higher angular momenta channels. Therefore, the binding energy in a higher momenta channel is $-2\tilde{U}$. These results are as shown in Fig. 5.3(d).

Experimentally, the excitonic modes can be accessed with a Raman process [175, 176, 177]; linear coupling to light is forbidden due to the fact that these excitonic modes have no electric dipole moment, unlike the particle-hole excitons in semiconductors. The electronic part of the operator for excitations into these modes has the form $\sum_{\mathbf{k}} \gamma_{\mathbf{k}} c^{\dagger}_{\mathbf{k}+\mathbf{q}\uparrow} c^{\dagger}_{-\mathbf{k}-\mathbf{q}\downarrow} c_{-\mathbf{k}\downarrow} c_{\mathbf{k}\uparrow}$, where $\gamma_{\mathbf{k}}$ has the symmetry of the excitonic mode (which is orthogonal to the superconducting gap and Higgs mode symmetry). For example, in refs. [175, 176, 177], excitonic modes with d-wave symmetry are selected using 2 photons with orthogonal polarizations such that $\gamma_{\mathbf{k}}$ overlaps with the required d-wave symmetry.

5.5.2 Stabilisation of the Higgs mode

Like in the case of the conventional BCS superconductor, the Higgs mode function here, Φ^{H}, is antisymmetric about the Fermi surface. We obtain its excitation en-

ergy numerically, using the antisymmetry of the mode function. Strikingly, the Higgs mode is in gap in the presence of the long-range interactions even though the superconductivity is still s-wave and there is no disorder or coexisting charge-density-wave phase. The Higgs mode excitation energy, ε^{H}, is close to but strictly below $\varepsilon^{\mathrm{exc}}_{k_F}$ for finite $\tilde{U}$. This means that, just like with the excitonic modes, the external laser intensity controls the energy separation between the Higgs mode and the quasiparticle continuum. We prove the inequality $\varepsilon^{\mathrm{H}} < \varepsilon^{\mathrm{exc}}_{k_F}$ by plugging an approximate mode function inspired by the Higgs mode function of a usual BCS superconductor given in Chapter. 4, $\phi^{\mathrm{ap}}_{\mathbf{k}} \propto \Delta_{\mathbf{k}}/[(E_{\mathbf{k}} - \tilde{U})\xi_{\mathbf{k}}]$ into Eq. (4.31),

$$\sum_{\mathbf{k}'} \mathcal{M}_{\mathbf{k}\mathbf{k}'} \phi^{\mathrm{ap}}_{\mathbf{k}'} = \left(4\Delta^2_{\mathbf{k}} - 4\tilde{U}\frac{\Delta^2_{\mathbf{k}}}{E_{\mathbf{k}}}\right)\phi^{\mathrm{ap}}_{\mathbf{k}} \leq (\varepsilon^{\mathrm{exc}}_{k_F})^2 \phi^{\mathrm{ap}}_{\mathbf{k}}. \tag{5.15}$$

Since we know that the Higgs mode is the lowest energy mode with rotational symmetry in k-space and antisymmetry about the Fermi surface, we conclude that the inequality holds for finite $\tilde{U}$. We also verified it numerically.

In Fig. 5.3(c), we show that for $\tilde{U} \ll \Delta^{\mathrm{in}}$,

$$\varepsilon^{\mathrm{H}} \approx \varepsilon^{\mathrm{exc}}_{k_F}. \tag{5.16}$$

Our numerical calculation show that the difference grows with the strength of the long-range interactions. In addition, we note that the range of the induced interactions is, though long, still finite in reality. The finite range slightly weakens the pairing in higher angular momentum channels relative to the s-wave channel [126], thus we should expect the separation between the Higgs mode and the excitonic modes to be still marginally larger.

This proximity in energy between the Higgs mode and the lowest excitonic mode in our relatively simple model is a general feature resulting from the long-range nature of the induced interactions. Therefore, it can serve as an indication that the superconductivity is supported by both short- and long-range interactions. We remark that in a more complicated model in which a subdominant superconducting channel is present, the excitonic modes corresponding to this channel can be lower in energy than the Higgs mode, as is the case in the absence of the long-range interactions. However, all other angular momentum channels which intrinsically do not sustain superconducting pairing support bound states in the presence of the long-range interactions. They give rise to a continuum of corresponding excitonic modes, and the edge of this continuum will be close to the Higgs mode energy.

An important consequence of the Higgs mode being in gap is that it can no longer decay through quasiparticle excitations, which usually dampen the Higgs mode such

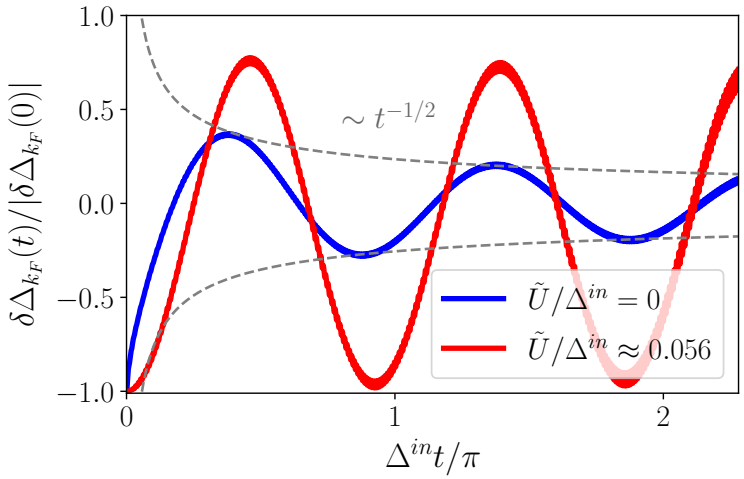


Figure 5.4: Normalised oscillations of the superconducting gap as a function of time following small perturbations in the Higgs mode of the superconductor with (in red) and without (in blue) the long-range interactions. Without the long-range interactions, the Higgs oscillation decays as $t^{-1/2}$ [189] as it is on the edge of the quasiparticle continuum. In contrast, in the presence of the long-range interactions, the Higgs oscillation does not decay. The intrinsic parameters for the superconductor used here are the same as in Fig. 5.3. The initial perturbations of the order parameters are about 2% of their equilibrium values. Due to the finite size of the initial perturbation, the gap oscillates around a value below the ground state value, hence the oscillations are offset by a small amount [196, 197, 164]. The offset vanishes when the perturbation strength tends to zero, when the pseudospin equation of motion can be linearised.

that it decays as $t^{-1/2}$, where t is time [150, 189, 147, 178]. To illustrate this point, we numerically simulate the order parameter oscillations following an excitation in the Higgs mode. We plot the time evolution of $\delta\Delta_{k_F}(t) = \Delta_{k_F}(t) - \Delta_{k_F}$, the deviation of the gap at the original Fermi surface from the ground state value, in Fig. 5.4. The numerics were performed by solving the equation of motion of the Anderson's pseudospins [Eq. (4.29)]. In an experiment, the Higgs mode could be excited by a strong THz pulse centred at half the Higgs mode frequency, and its subsequent oscillations could be observed by measuring the transmittance of time-delayed THz probe pulses [152, 147, 153, 154]. An alternative method to excite the superconductor is through a stimulated Raman process in the optical frequencies [198]. We see that without the long-range interactions, the oscillation decays quickly, in agreement with earlier studies [150, 189, 147, 178]. In contrast, in the presence of the long-range interactions, the gap shows clean oscillations. We see, more clearly from the red line, that the gap oscillates around a value below the ground state equilibrium value. This is due to the finite size of the initial perturbation and the nonlinear nature of the

equation of motion [196, 197, 164]. This offset vanishes as the perturbation strength tends to zero; the pseudospin equation of motion can be linearised in this limit.

Our study shows that the Higgs mode becomes a well-defined collective mode [189, 151] when the long-range interactions are switched on, making it easier to detect and distinguish in this system [142].

As a side note, because the Higgs mode and the excitonic modes have different symmetries, they could potentially be more clearly distinguished in Raman measurements despite their proximity in energy [158].

5.6 Conclusion

In this chapter, we have shown that the tunable cavity-mediated long-range interactions proposed in proposed in Chapter. 3 not only enhance BCS superconductivity, but also qualitatively alter the collective excitations in a superconductor which intrinsically only has short-range interactions. Two features are most notable. First, additional excitonic modes with finite energies appear in gap as the long-range interactions create extra electron-pair bound states. This also means that preexisting excitonic modes corresponding to intrinsic subdominant superconducting orders are further separated from the quasiparticle continuum, making them more distinguishable in experiments. Second, and more strikingly, the Higgs mode of the system is also pushed below the quasiparticle excitation gap, and below the aforementioned excitonic modes. As a result, the Higgs mode becomes stable and easier to observe experimentally regardless of the mechanism that makes it visible. We emphasise that what we present is one of the few known cases where the Higgs mode is below the quasiparticle continuum, and thus is a well-defined collective mode. Moreover, the imposition of the long-range interactions does not alter the other characteristics (symmetries, coupling to light, etc.) of the Higgs mode. This makes this driven cavity system a promising platform for studying Higgs modes in superconductors when they are normally damped by quasiparticle excitations. Studies on the collective excitations in such systems could help with experimental identification of superconductors with a similar superconducting mechanism, or help to identify the ground state gap symmetry [164]. These studies are also important towards understanding and controlling non-equilibrium dynamics of these coupled light-matter systems.

Recent theoretical studies on cavity-coupled electron systems pointed out that electron-phonon interactions can be increased by coupling to a cavity, and that due to the small momenta of light, the cavity only affects forward scattering strongly

[53, 160]. This means that the enhanced scattering is also long-range in nature, and thus they offer a possible alternative system which could host the unusual collective modes discussed in this work. The features presented in our work, along with the aforementioned references, bolster expectations of novel states of matter when quantum materials, which typically have only short-ranged interactions, are strongly coupled to cavities, which can strongly affect forward scattering.

More generally, our study is also relevant to cold atomic gases, where short-range interactions are controlled using Feshback resonance [199], and long-range interactions can be engineered by coupling to quantum vacua at optical frequencies [123, 124, 125, 126, 127, 128, 129, 96, 130, 131, 132, 133, 134, 135, 136, 137]. Specifically, a theory similar to ours could be applied to fermionic atomic gases [200] subject to additional long-range interactions, which should alter the collective modes of the superfluids [201, 202].

Chapter 6

Conclusions

We end by summarising the contributions of this thesis and discussing possible future directions of research in the area.

In the present thesis, we have explored using strong coupling to terahertz cavities and strong terahertz driving fields to engineer electronic systems. The work has been inspired by the remarkable progress in the technologies for intense terahertz laser sources as well as nanoplasmonic terahertz cavities which can achieve large vacuum field fluctuations.

Our first contribution is the formulation of a novel scheme which combines the two aforementioned photonic technologies. In Chapter. 3, we have shown that the combination of external driving and strong coupling to a cavity induces controllable long-range electron interactions in single-band 2D materials. Provided that the driving is detuned from the cavity further than the plasmon frequencies at the relevant wavevectors, the interactions cannot be effectively screened. When the interactions are attractive, we have found that they can cause an instability for the electrons in the Cooper channel at observable temperatures. The interactions are generated by two-photon diamagnetic processes. Therefore, they are largely independent of the electron band dispersion and can be induced on top of existing interactions. Our work opens the possibility of implementing and studying long-range interactions in electron systems as well as controlling quantum phases of matter through on-demand quantum systems engineering.

Building on this scheme and other related proposals, in Chapter. 5, we consider a general scenario where the long-range interactions are imposed upon a conventional superconductor which has local attractions intrinsically. We specifically focused on the low-lying excitations on top of the s-wave ground state at the zero-temperature limit. We have found that the Bogoliubov quasiparticle excitation energies increase when we impose long-range attractive interactions. This way, the superconducting

gap is enlarged. We have also seen that the long-range nature of the induced attractions leads to the appearance of additional collective excitations of the excitonic modes. More strikingly, the long-range attractions ''push" the Higgs mode "in gap", i.e., below the quasiparticle continuum. As a result, the Higgs mode is stabilised by the imposition of the long-range attractions. Our proposal, therefore, provides one of the few pathways for stabilising the Higgs mode in a superconductor. More generally, our work also boosts the expectation of unusual states of quantum matter when coupled to a quantum light field.

On the outlook, a thorough survey of the properties of the long-range-interaction-enhanced BCS superconductivity close to the critical temperature is yet to be carried out. A Ginzburg-Landau theory of the system (which might be derived from a path-integral formulation of the problem [203]) could yield measures, such as the coherence length, that characterise the superconductor [3]. Moreover, the effect of the long-range interactions on superconductors with different ground state symmetries, e.g., d-wave, remains to be investigated. In a d-wave superconductor, the Higgs mode is more heavily damped than in a s-wave superconductor [204]. It would be interesting to see whether the long-range attractions could also stabilise this Higgs mode.

The prospect of applying the long-range interactions to materials with strong correlations is even more exciting. It remains to be investigated whether the unconventional superconductivity of, e.g., cuprates or magic-angle twisted bilayer graphenes, could be enhanced by these long-range attractions; and if so, how strong the enhancement might be. Additionally, for the purpose of quantum state engineering, understanding the effect of the long-range interactions on quantum systems with competing phases is certainly desirable.

With the same setup considered in Chapter. 3, other interesting phenomena could arise in a different system parameter regime. In particular, instead of limiting the size of the detuning between the driving and the cavity frequencies to be much larger than the relevant plasma frequency, as we have done in this thesis, one could study the dynamics when the detuning and the plasma frequency are comparable. This could potentially lead to cooling of the electronic degrees of the freedom in a similar fashion as sideband cooling of atoms [84], solids [205] and superconducting phase difference across a Josephson junction [206].

Finally, strong light-matter coupling in a highly non-equilibrium setting could prove to be a fruitful area of research. Out-of-equilibrium quantum systems attained from, e.g., quenching, have already received a great deal of attention from both theoretical and experimental sides [207, 208, 209, 210, 211, 212, 213, 214]. In particular, it

has been pointed out that long-range interactions can keep quantum systems in some metastable state with long lifetimes [211, 212]. In the setup we studied, the long-range interaction strength is controlled by the external driving laser intensity, it is thus possible to tune the interactions dynamically. Another recent work [215] demonstrated the ability to drastically change the strong coupling between the cavity fields and the electrons within a time frame as short as 5 percent of the oscillation period. Given these possibilities to control light-matter coupling dynamically, it would be interesting to study the out-of-equilibrium dynamics upon quenching of the long-range interactions in this type of systems, which might have application in stabilising certain non-equilibrium states such as the superconducting-like states created by strong driving.

Appendix A

Proof: connection between Matsubara Green's function and retarded Green's functions

First, we recall the definitions of the two types of Green's functions

$$\mathcal{C}_{P,Q}(\tau_1,\tau_2) = -\frac{1}{\hbar}\langle \mathcal{T}_\tau P(\tau_1)Q(\tau_2)\rangle \tag{A.1}$$

$$\mathcal{C}^{\text{ret}}_{P,Q}(t_1,t_2) = -\frac{\mathrm{i}}{\hbar}\Theta(t_1-t_2)\langle [P(t_1),Q(t_2)]_{\text{B,F}}\rangle, \tag{A.2}$$

where the subscript 'B' and 'F' refer to boson and fermion respectively.

The Lehmann representation uses the complete set of eigenstates of $\hat{H}$, $\{|m\rangle\}$, such that $\hat{H}\,|m\rangle = E_m\,|m\rangle$. Substitute the complete set into the definition for retarded function above,

$$\mathcal{C}^{\text{ret}}_{P,Q}(t_1,t_2) = -\frac{\mathrm{i}}{\hbar}\Theta(t_1-t_2)\langle [P(t_1),Q(t_2)]_{\text{B,F}}\rangle \tag{A.3}$$

$$= -\frac{\mathrm{i}}{\hbar\mathcal{Z}}\Theta(t_1-t_2)\sum_{n,m}\mathrm{e}^{-\beta E_n}\Big\{\langle n|\,P(t_1)\,|m\rangle\langle m|\,Q(t_2)\,|n\rangle \pm \langle n|\,Q(t_2)\,|m\rangle\langle m|\,P(t_1)\,|n\rangle\Big\} \tag{A.4}$$

$$= -\frac{\mathrm{i}}{\hbar\mathcal{Z}}\Theta(t_1-t_2)\sum_{n,m}\langle n|\,P\,|m\rangle\langle m|\,Q\,|n\rangle\,\mathrm{e}^{\frac{\mathrm{i}}{\hbar}(t_1-t_2)(E_n-E_m)}\Big[\mathrm{e}^{-\beta E_n}-\mathrm{e}^{-\beta E_m}\Big] \tag{A.5}$$

Fourier transform gives

$$\mathcal{C}^{\mathrm{ret}}_{P,Q}(\omega) = -\frac{\mathrm{i}}{\hbar\mathcal{Z}}\int_0^\infty \mathrm{d}t\, \mathrm{e}^{\mathrm{i}(\omega+\mathrm{i}\eta)t}\sum_{n,m}\langle n|\, P\,|m\rangle\langle m|\, Q\,|n\rangle\, \mathrm{e}^{\frac{\mathrm{i}}{\hbar}t(E_n-E_m)}\left[\mathrm{e}^{-\beta E_n}-\mathrm{e}^{-\beta E_m}\right] \tag{A.6}$$

$$= \frac{1}{\hbar\mathcal{Z}}\sum_{n,m}\langle n|\, P\,|m\rangle\langle m|\, Q\,|n\rangle\, \frac{\mathrm{e}^{-\beta E_n}-\mathrm{e}^{-\beta E_m}}{\omega+\mathrm{i}\eta+E_n-E_m}, \tag{A.7}$$

where η is infinitesimal.

Similarly, the Matsubara Green's function gives

$$\mathcal{C}_{P,Q}(\tau,\tau') = -\frac{1}{\hbar}\langle \mathcal{T}_\tau P(\tau)Q(\tau')\rangle \tag{A.8}$$

$$= -\frac{1}{\hbar\mathcal{Z}}\sum_{n,m}\langle n|\, P\,|m\rangle\langle m|\, Q\,|n\rangle\, \mathrm{e}^{-\beta E_n}\mathrm{e}^{(\tau_1-\tau_2)(E_n-E_m)} \tag{A.9}$$

for $t_1 > t_2$. In the (corresponding) Matsubara frequency representation,

$$\mathcal{C}_{P,Q}(\mathrm{i}\omega_n) = -\frac{1}{\hbar\mathcal{Z}}\sum_{n,m}\langle n|\, P\,|m\rangle\langle m|\, Q\,|n\rangle\, \mathrm{e}^{-\beta E_n}\int_0^\beta \mathrm{d}\tau\, \mathrm{e}^{\tau(E_n-E_m)} \tag{A.10}$$

$$= \frac{1}{\hbar\mathcal{Z}}\sum_{n,m}\langle n|\, P\,|m\rangle\langle m|\, Q\,|n\rangle\, \frac{\mathrm{e}^{-\beta E_n}-\mathrm{e}^{-\beta E_m}}{\mathrm{i}\omega_n+E_n-E_m}. \tag{A.11}$$

Comparing Eq. (A.11) with Eq. (A.7), we see that the Matsubara Green's function is related to the retarded function by analytic continuation $\mathrm{i}\omega_n \to \omega + \mathrm{i}\eta$

Appendix B

Estimates of Laser Induced Heating

Results presented in this appendix were published in the Supplemental Materials of H. Gao, F. Schlawin, M. Buzzi, A. Cavalleri, and D. Jaksch, Photoinduced Electron Pairing in a Driven Cavity, *Phys. Rev. Lett.* **125**, 053602 (2020). Most content in this appendix is written by M. Buzzi, who performed the calculations related to substrate heating.

Two potential sources of heating can be distinguished, the direct heating of the two-dimensional electron gas, which we discuss in the main text, and the indirect heating through absorption in the underlying substrate structure.

The heating rate due to the former process is negligible. We can estimate this by considering the inelastic electron scattering rate due to the environmental modes that we considered above and the maximum energy gain of an intraband scattering event for an electron. At 10THz driving frequency, and $1\mathrm{GW/cm}^2$ intensity, the heating rate is of order pW.

To discuss the importance of the second process, we consider the case of the two-dimensional electron gas at the $LaAlO_3/SrTiO_3$ interface. Currently, no continuous wave THz sources are able to offer irradiances of $1\mathrm{GW/cm}^2$ at 10THz central frequency and an experimental realization of our proposal should consider a driving protocol based on short pulses where peak intensities exceeding $1\mathrm{GW/cm}^2$ can be easily obtained [17]. Importantly, even upon pulsed driving, changes in the transport properties of the two-dimensional electron gas could be tracked with on-chip time-resolved conductivity measurements [102].

In the following, we estimate the heating of a bulk $SrTiO_3$ substrate driven with 1ps long pulses at 10THz central frequency. We omit the absorption in the $LaAlO_3$ layer which is typically only few unit cells thick and model the energy deposited by

the drive as:

$$E(z) = (1 - R)\frac{\mathcal{F}}{d_{pump}} \exp\left\{-\frac{z}{d_{pump}}\right\}, \tag{B.1}$$

where $R = 0.995$ is the reflectivity of $SrTiO_3$ at the excitation frequency [216], $d_{pump} = 0.68\mu m$ is the intensity penetration depth of the pump, and $\mathcal{F}$ is the excitation energy density chosen to be 0.1 and 1mJ/cm^2 to reach peak intensities of 100MW/cm^2 and 1GW/cm^2 respectively.

The temperature profile $T_f(z)$ inside the sample is related to the deposited energy density $E(z)$ by the following integral equation:

$$E(z) = \int_{T_i}^{T_f(z)} C_p(T)\,\mathrm{d}T \tag{B.2}$$

where $T_i = 0.5\text{K}$ is the initial temperature of the sample and $C_p(T)$ is the specific heat of $SrTiO_3$ taken from an interpolation of an equilibrium measurement [217]. As heat diffusion, happens on much longer time scales [218] than the few picoseconds time interval in which an experiment would be performed, it was not included in these calculations.

Fig. B.1(a) shows the result of these estimates. We observe that at driving peak intensities of 1GW/cm^2 the final temperature at the surface of the $SrTiO_3$ substrate has increased to $\sim$ 15K. Reducing the driving strength to 100MW/cm^2 helps to contain the heating to no more than a few Kelvins. The final temperature could be lowered even further if substrates that offer more transparency at the driving frequency are chosen.

As an example, we repeat the same calculations on a substrate featuring a 50 times longer penetration depth . The results are shown in Fig. B.1(b). In this case the heating for both driving intensities is negligible. We envision that this setting could be achieved by exploiting two-dimensional electron gases at the interface with different substrate materials (as for example diamond or silicon) that offer complete transparency at the driving frequency.

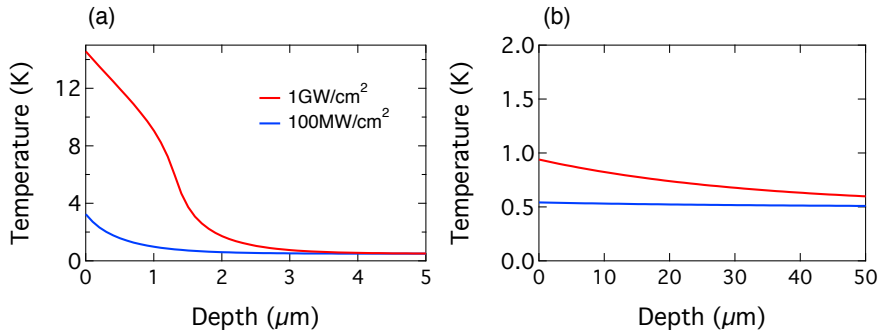


Figure B.1: (a) Depth resolved temperature profiles in the $SrTiO_3$ substrate after excitation with 1ps pulses at 10THz central frequency for two different peak intensities of 1GW/cm^2 (red curves) and 100MW/cm^2 (blue curves). (b) Same calculations performed for a substrate offering a 50 times longer light penetration depth at the driving frequency.

Appendix C

Enhancement of the critical temperature by long-range interactions

In this appendix, we explain the approximation made to obtain Eq. (5.4) and provide estimated ratio of enhancement of the critical temperature using realistic material, driving and cavity parameters.

we rearrange Eq. (5.3) to get,

$$\Delta_{\mathbf{k}}\Big[1-\frac{\tilde{U}}{\xi_{\mathbf{k}}}\tanh\left(\frac{\xi_{\mathbf{k}}}{2T}\right)\Big]=\tilde{V}\sum_{\mathbf{k}'}\frac{\Delta_{\mathbf{k}'}}{2\xi_{\mathbf{k}'}}\tanh\left(\frac{\xi_{\mathbf{k}'}}{2T}\right). \tag{C.1}$$

The RHS is independent of $\mathbf{k}$, we deduce from it that $\Delta_{\mathbf{k}} \propto \left[1-\frac{\tilde{U}}{\xi_{\mathbf{k}}}\tanh\left(\frac{\xi_{\mathbf{k}}}{2T}\right)\right]^{-1}$. Upon substituting this proportionality back into the gap equation, we have

$$1=N(0)V\int_0^{\epsilon_{\mathrm{D}}}\mathrm{d}\xi\,\frac{\frac{1}{\xi}\tanh\left(\frac{\xi}{2T_c}\right)}{1-\frac{\tilde{U}}{\xi}\tanh\left(\frac{\xi}{2T_c}\right)}. \tag{C.2}$$

This integral equation yields T_c.

We obtain the approximate ratio of enhancement of T_c [Eq. (5.4)] by breaking the above integral into two parts according to the value of ξ. For $\xi \leq 2T_c$, $\tanh(\xi/2T_c) \approx \xi/2T_c$ and for $\xi > 2T_c$, $\tanh(\xi/2T_c) \approx 1$. These approximations allow us to compute the integral analytically. We take the ratio of critical temperatures calculated with and without $\tilde{U}$ to obtain Eq. (5.4). We compare the results on δT_c with and without the approximation in Fig. C.1, and they show good agreement.

In Fig. C.2(a), we show the enhancement ratio T_c/T_c^{in} as a function of the driving intensity I_{d} and T_c^{in}. We see that for the same driving intensity, the enhancement

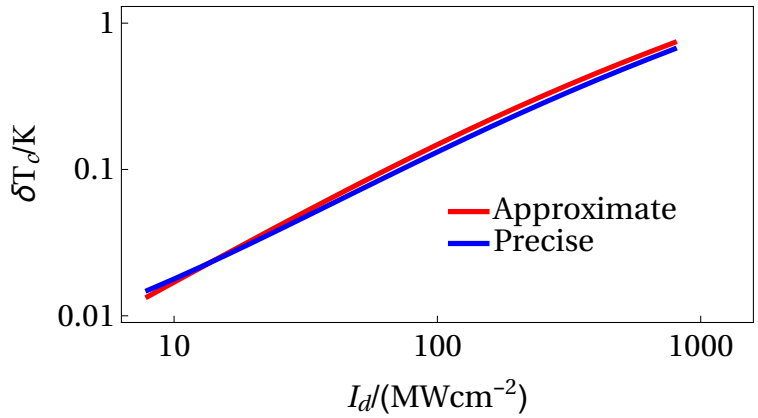


Figure C.1: We compare the predictions of enhancement of T_c using Eq. (5.4) and Eq. (C.2). The two sets of calculations agree excellently. Here we use $\hbar\omega_{\rm D}/k_B = 200$K and $T_c^{\rm in} = 1$K. the same material parameters as in Fig. 5.3 and the same cavity and driving parameters as in Fig. C.2.

ratio of the superconducting critical temperature is more pronounced for superconductors with lower $T_c^{\rm in}$'s: for superconductors such as overdoped (by gating) lanthanum aluminate-strontium titanate interface (LAO/STO) with $T_c^{\rm in} \lesssim 200$mK [193], the enhancement factor can be as high as 6 with realistic driving and cavity parameters. For superconductors with a higher $T_c^{\rm in}$'s, e.g. K_3C_{60} thin films [220], the enhancement factor achievable is lower. This can be understood by realising that the dimensionless parameter $\tilde{U}/T_c^{\rm in}$ is reduced for the following reasons: firstly, $T_c^{\rm in}$ takes a larger value; and secondly, the detuning δ_c needs to be larger at higher critical temperatures, and it forces $\tilde{U}$ to be smaller.

Fig. C.2(b) connects Fig. C.2(a) with Fig. 5.2. We show the range of enhancements achievable for the superconductors considered in Fig. C.2(a) by overlaying the red curve in Fig. 5.2 with correspondingly colored lines.

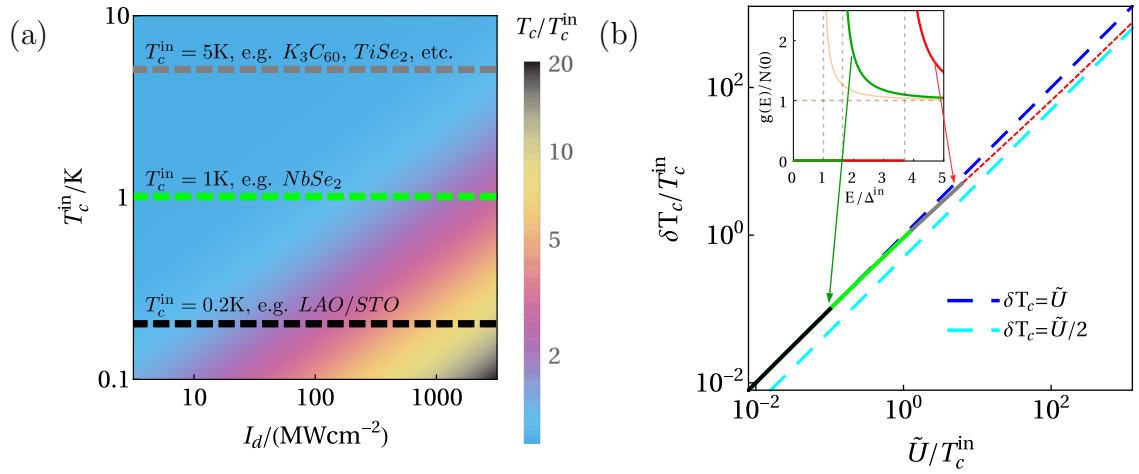


Figure C.2: (a) A color map showing the ratio of enhancement of the superconducting critical temperature as a function of the driving intensity, $I_{\rm d}$, and the intrinsic critical temperature, $T_c^{\rm in}$. (b) The ratio of enhancement of the superconducting critical temperature as a function of normalised long-range interaction strength, $\tilde{U}/T_c^{\rm in}$, is obtained by solving Eq. (5.4), and it is plotted as the red dotted line. The blue and cyan dashed lines give the asymptotic behaviours in the limits of weak induced long-range interactions and weak local intrinsic interactions, respectively. Inset: density of states of the Bogoliubov quasiparticles normalised by the density of state at the Fermi surface in the normal phase is shown for system without the long-range interactions (pale orange line), with mild long-range interactions (green line) and with strong long-range interactions (red line). The divergence of the density of state sharpens as the long-range attractions get stronger. For comparison, overdoped LAO/STO interfaces have $T_c \lesssim 200$mK [193], monolayer $NbSe_2$ has $T_c \approx 1$K [219], and K_3C_{60} thin films have $T_c \approx 5$K [220]. We show them, respectively, as the gray, green and black dashed lines in (a). The corresponding ranges of enhancement achievable as shown in (a) are indicated in (b) with solid lines of the same colors. Here we take $\Lambda = 2.5/8 \times 10^{-5}$, $\delta_c = 2\pi T_c$ and $\omega_c = 1.1\omega_L$, same as in Chapter. 3.

Bibliography

[1] C. Kittel, *Quantum theory of solids*. New York: John Wiley & Sons, 1987.

[2] P. W. Anderson, "More is different," *Science*, vol. 177, no. 4047, pp. 393–396, 1972.

[3] M. Tinkham, *Introduction to Superconductivity*. International series in pure and applied physics, McGraw Hill, 1996.

[4] H. Kamerlingh Onnes, "Further experiments with liquid helium. d. on the change of electric resistance of pure metals at very low temperatures," *Comm. Phys. Lab. Univ. Leiden*, vol. 122b, 1911.

[5] J. Hirsch, M. Maple, and F. Marsiglio, "Superconducting materials classes: Introduction and overview," *Physica C: Superconductivity and its Applications*, vol. 514, pp. 1–8, 2015. Superconducting Materials: Conventional, Unconventional and Undetermined.

[6] M. Somayazulu, M. Ahart, A. K. Mishra, Z. M. Geballe, M. Baldini, Y. Meng, V. V. Struzhkin, and R. J. Hemley, "Evidence for superconductivity above 260 k in lanthanum superhydride at megabar pressures," *Phys. Rev. Lett.*, vol. 122, p. 027001, Jan 2019.

[7] F. D. M. Haldane, "Luttinger liquid theory of one-dimensional quantum fluids. I. Properties of the Luttinger model and their extension to the general 1D interacting spinless Fermi gas," *J. Phys. C Solid State Phys.*, vol. 14, pp. 2585–2609, jul 1981.

[8] O. M. Auslaender, H. Steinberg, A. Yacoby, Y. Tserkovnyak, B. I. Halperin, K. W. Baldwin, L. N. Pfeiffer, and K. W. West, "Spin-charge separation and localization in one dimension," *Science*, vol. 308, no. 5718, pp. 88–92, 2005.

[9] Y. Jompol, C. J. B. Ford, J. P. Griffiths, I. Farrer, G. A. C. Jones, D. Anderson, D. A. Ritchie, T. W. Silk, and A. J. Schofield, "Probing spin-charge separation in a Tomonaga-Luttinger liquid," *Science*, vol. 325, no. 5940, pp. 597–601, 2009.

[10] Y. Ma, H. C. Diaz, J. Avila, C. Chen, V. Kalappattil, R. Das, M.-H. Phan, T. Čadež, J. M. P. Carmelo, M. C. Asensio, and M. Batzill, "Angle resolved photoemission spectroscopy reveals spin charge separation in metallic $MoSe_2$ grain boundary," *Nat. Commun.*, vol. 8, p. 14231, Feb. 2017.

[11] A. Zunger and O. I. Malyi, "Understanding doping of quantum materials," *Chem. Rev.*, Jan 2021.

[12] J. V. Badding, J. F. Meng, and D. A. Polvani, "Pressure tuning in the search for new and improved solid state materials," *Chem. Mater.*, vol. 10, no. 10, pp. 2889–2894, 1998.

[13] D. G. Schlom, L.-Q. Chen, C.-B. Eom, K. M. Rabe, S. K. Streiffer, and J.-M. Triscone, "Strain tuning of ferroelectric thin films," *Ann. Rev. Mater. Res.*, vol. 37, no. 1, pp. 589–626, 2007.

[14] P. Zubko, S. Gariglio, M. Gabay, P. Ghosez, and J.-M. Triscone, "Interface physics in complex oxide heterostructures," *Annu. Rev. Conden. Ma. P.*, vol. 2, no. 1, pp. 141–165, 2011.

[15] K. S. Novoselov, A. Mishchenko, A. Carvalho, and A. H. Castro Neto, "2d materials and van der waals heterostructures," *Science*, vol. 353, no. 6298, 2016.

[16] B. Green, S. Kovalev, V. Asgekar, G. Geloni, U. Lehnert, T. Golz, M. Kuntzsch, C. Bauer, J. Hauser, J. Voigtlaender, B. Wustmann, I. Koesterke, M. Schwarz, M. Freitag, A. Arnold, J. Teichert, M. Justus, W. Seidel, C. Ilgner, N. Awari, D. Nicoletti, S. Kaiser, Y. Laplace, S. Rajasekaran, L. Zhang, S. Winnerl, H. Schneider, G. Schay, I. Lorincz, A. A. Rauscher, I. Radu, S. Mährlein, T. H. Kim, J. S. Lee, T. Kampfrath, S. Wall, J. Heberle, A. Malnasi-Csizmadia, A. Steiger, A. S. Müller, M. Helm, U. Schramm, T. Cowan, P. Michel, A. Cavalleri, A. S. Fisher, N. Stojanovic, and M. Gensch, "High-field high-repetition-rate sources for the coherent THz control of matter," *Sci. Rep.*, vol. 6, no. 1, 2016.

[17] B. Liu, H. Bromberger, A. Cartella, T. Gebert, M. Först, and A. Cavalleri, "Generation of narrowband, high-intensity, carrier-envelope phase-stable pulses tunable between 4 and 18 THz," *Opt. Lett.*, vol. 42, no. 1, pp. 129–131, 2017.

[18] G. Scalari, C. Maissen, D. Turčinková, D. Hagenmüller, S. De Liberato, C. Ciuti, C. Reichl, D. Schuh, W. Wegscheider, M. Beck, and J. Faist, "Ultrastrong coupling of the cyclotron transition of a 2d electron gas to a thz metamaterial," *Science*, vol. 335, no. 6074, pp. 1323–1326, 2012.

[19] W. E. Lamb, "Anti-photon," *Applied Physics B*, vol. 60, pp. 77–84, Feb 1995.

[20] M. Rini, R. Tobey, N. Dean, J. Itatani, Y. Tomioka, Y. Tokura, R. W. Schoenlein, and A. Cavalleri, "Control of the electronic phase of a manganite by mode-selective vibrational excitation," *Nature*, vol. 449, p. 72, 2007.

[21] M. Liu, H. Y. Hwang, H. Tao, A. C. Strikwerda, K. Fan, G. R. Keiser, A. J. Sternbach, K. G. West, S. Kittiwatanakul, J. Lu, S. A. Wolf, F. G. Omenetto, X. Zhang, K. A. Nelson, and R. D. Averitt, "Terahertz-field-induced insulator-to-metal transition in vanadium dioxide metamaterial," *Nature*, vol. 487, p. 345, 2012.

[22] T. F. Nova, A. Cartella, A. Cantaluppi, M. Först, D. Bossini, R. V. Mikhaylovskiy, A. V. Kimel, R. Merlin, and A. Cavalleri, "An effective magnetic field from optically driven phonons," *Nat. Phys.*, vol. 13, p. 132, 2016.

[23] R. Mankowsky, A. von Hoegen, M. Först, and A. Cavalleri, "Ultrafast reversal of the ferroelectric polarization," *Phys. Rev. Lett.*, vol. 118, p. 197601, May 2017.

[24] T. F. Nova, A. S. Disa, M. Fechner, and A. Cavalleri, "Metastable ferroelectricity in optically strained srtio3," *Science*, vol. 364, no. 6445, pp. 1075–1079, 2019.

[25] D. Fausti, R. I. Tobey, N. Dean, S. Kaiser, A. Dienst, M. C. Hoffmann, S. Pyon, T. Takayama, H. Takagi, and A. Cavalleri, "Light-induced superconductivity in a stripe-ordered cuprate," *Science*, vol. 331, no. 6014, pp. 189–191, 2011.

[26] M. Först, R. I. Tobey, H. Bromberger, S. B. Wilkins, V. Khanna, A. D. Caviglia, Y.-D. Chuang, W. S. Lee, W. F. Schlotter, J. J. Turner, M. P. Minitti, O. Krupin, Z. J. Xu, J. S. Wen, G. D. Gu, S. S. Dhesi, A. Cavalleri, and

J. P. Hill, "Melting of charge stripes in vibrationally driven $la_{1.875}ba_{0.125}cuo_4$: Assessing the respective roles of electronic and lattice order in frustrated superconductors," *Phys. Rev. Lett.*, vol. 112, p. 157002, 2014.

[27] K. A. Cremin, J. Zhang, C. C. Homes, G. D. Gu, Z. Sun, M. M. Fogler, A. J. Millis, D. N. Basov, and R. D. Averitt, "Photoenhanced metastable c-axis electrodynamics in stripe-ordered cuprate la1.885ba0.115cuo4," *P. Natl. Acad. Sci.*, vol. 116, no. 40, pp. 19875–19879, 2019.

[28] M. Först, A. Frano, S. Kaiser, R. Mankowsky, C. R. Hunt, J. J. Turner, G. L. Dakovski, M. P. Minitti, J. Robinson, T. Loew, M. Le Tacon, B. Keimer, J. P. Hill, A. Cavalleri, and S. S. Dhesi, "Femtosecond x rays link melting of charge-density wave correlations and light-enhanced coherent transport in $YBa_2Cu_3o_{6.6}$," *Phys. Rev. B*, vol. 90, p. 184514, 2014.

[29] R. Mankowsky, B. Liu, S. Rajasekaran, H. Y. Liu, D. Mou, X. J. Zhou, R. Merlin, M. Först, and A. Cavalleri, "Dynamical stability limit for the charge density wave in $k_{0.3}moo_3$," *Phys. Rev. Lett.*, vol. 118, p. 116402, 2017.

[30] W. Hu, S. Kaiser, D. Nicoletti, C. R. Hunt, I. Gierz, M. C. Hoffmann, M. Le Tacon, T. Loew, B. Keimer, and A. Cavalleri, "Optically enhanced coherent transport in yba2cu3o6.5 by ultrafast redistribution of interlayer coupling," *Nat. Mater.*, vol. 13, p. 705, 2014.

[31] R. Mankowsky, A. Subedi, M. Först, S. O. Mariager, M. Chollet, H. T. Lemke, J. S. Robinson, J. M. Glownia, M. P. Minitti, A. Frano, M. Fechner, N. A. Spaldin, T. Loew, B. Keimer, A. Georges, and A. Cavalleri, "Nonlinear lattice dynamics as a basis for enhanced superconductivity in yba2cu3o6.5," *Nature*, vol. 516, p. 71, 2014.

[32] M. Mitrano, A. Cantaluppi, D. Nicoletti, S. Kaiser, A. Perucchi, S. Lupi, P. Di Pietro, D. Pontiroli, M. Ricco, S. R. Clark, D. Jaksch, and A. Cavalleri, "Possible light-induced superconductivity in k3c60 at high temperature," *Nature*, vol. 530, p. 461, 2016.

[33] M. Budden, T. Gebert, M. Buzzi, G. Jotzu, E. Wang, T. Matsuyama, G. Meier, Y. Laplace, D. Pontiroli, M. Riccò, F. Schlawin, D. Jaksch, and A. Cavalleri, "Evidence for metastable photo-induced superconductivity in K3C60," *Nat. Phys.*, vol. 17, pp. 611–618, May 2021.

[34] B. Buča, J. Tindall, and D. Jaksch, "Non-stationary coherent quantum many-body dynamics through dissipation," *Nat. Commun.*, vol. 10, p. 1730, Apr 2019.

[35] J. Tindall, F. Schlawin, M. Buzzi, D. Nicoletti, J. R. Coulthard, H. Gao, A. Cavalleri, M. A. Sentef, and D. Jaksch, "Dynamical order and superconductivity in a frustrated many-body system," *Phys. Rev. Lett.*, vol. 125, p. 137001, Sep 2020.

[36] E. M. Purcell, H. C. Torrey, and R. V. Pound, "Resonance absorption by nuclear magnetic moments in a solid," *Phys. Rev.*, vol. 69, pp. 37–38, Jan 1946.

[37] G. Rempe, H. Walther, and N. Klein, "Observation of quantum collapse and revival in a one-atom maser," *Phys. Rev. Lett.*, vol. 58, pp. 353–356, Jan 1987.

[38] G. Rempe, R. J. Thompson, R. J. Brecha, W. D. Lee, and H. J. Kimble, "Optical bistability and photon statistics in cavity quantum electrodynamics," *Phys. Rev. Lett.*, vol. 67, pp. 1727–1730, Sep 1991.

[39] M. G. Raizen, R. J. Thompson, R. J. Brecha, H. J. Kimble, and H. J. Carmichael, "Normal-mode splitting and linewidth averaging for two-state atoms in an optical cavity," *Phys. Rev. Lett.*, vol. 63, pp. 240–243, Jul 1989.

[40] H. J. Kimble, "Strong interactions of single atoms and photons in cavity QED," *Phys. Scr.*, vol. T76, no. 1, p. 127, 1998.

[41] P. A. Hobson, W. L. Barnes, D. G. Lidzey, G. A. Gehring, D. M. Whittaker, M. S. Skolnick, and S. Walker, "Strong exciton–photon coupling in a low-q all-metal mirror microcavity," *Appl. Phys. Lett.*, vol. 81, no. 19, pp. 3519–3521, 2002.

[42] T. Yoshie, A. Scherer, J. Hendrickson, G. Khitrova, H. M. Gibbs, G. Rupper, C. Ell, O. B. Shchekin, and D. G. Deppe, "Vacuum rabi splitting with a single quantum dot in a photonic crystal nanocavity," *Nature*, vol. 432, pp. 200–203, Nov 2004.

[43] J. P. Reithmaier, G. Sek, A. Löffler, C. Hofmann, S. Kuhn, S. Reitzenstein, L. V. Keldysh, V. D. Kulakovskii, T. L. Reinecke, and A. Forchel, "Strong coupling in a single quantum dot–semiconductor microcavity system," *Nature*, vol. 432, pp. 197–200, Nov 2004.

[44] E. Peter, P. Senellart, D. Martrou, A. Lemaître, J. Hours, J. M. Gérard, and J. Bloch, "Exciton-photon strong-coupling regime for a single quantum dot embedded in a microcavity," *Phys. Rev. Lett.*, vol. 95, p. 067401, Aug 2005.

[45] S. Kéna-Cohen and S. R. Forrest, "Room-temperature polariton lasing in an organic single-crystal microcavity," *Nat. Photonics*, vol. 4, pp. 371–375, Jun 2010.

[46] G. Khitrova, H. M. Gibbs, M. Kira, S. W. Koch, and A. Scherer, "Vacuum rabi splitting in semiconductors," *Nature Physics*, vol. 2, pp. 81–90, Feb 2006.

[47] X. Li, M. Bamba, Q. Zhang, S. Fallahi, G. C. Gardner, W. Gao, M. Lou, K. Yoshioka, M. J. Manfra, and J. Kono, "Vacuum bloch–siegert shift in landau polaritons with ultra-high cooperativity," *Nature Photonics*, vol. 12, pp. 324–329, Jun 2018.

[48] G. Scalari, C. Maissen, D. Hagenmüller, S. De Liberato, C. Ciuti, C. Reichl, W. Wegscheider, D. Schuh, M. Beck, and J. Faist, "Ultrastrong light-matter coupling at terahertz frequencies with split ring resonators and inter-landau level transitions," *J. Appl. Phys.*, vol. 113, no. 13, p. 136510, 2013.

[49] C. Maissen, G. Scalari, F. Valmorra, M. Beck, J. Faist, S. Cibella, R. Leoni, C. Reichl, C. Charpentier, and W. Wegscheider, "Ultrastrong coupling in the near field of complementary split-ring resonators," *Phys. Rev. B*, vol. 90, p. 205309, 2014.

[50] H. Hübener, U. De Giovannini, C. Schäfer, J. Andberger, M. Ruggenthaler, J. Faist, and A. Rubio, "Engineering quantum materials with chiral optical cavities," *Nature Materials*, vol. 20, no. 4, pp. 438–442, 2021.

[51] M. A. Sentef, J. Li, F. Künzel, and M. Eckstein, "Quantum to classical crossover of floquet engineering in correlated quantum systems," *Phys. Rev. Research*, vol. 2, p. 033033, Jul 2020.

[52] A. Thomas, E. Devaux, K. Nagarajan, T. Chervy, M. Seidel, D. Hagenmüller, S. Schütz, J. Schachenmayer, C. Genet, G. Pupillo, and T. W. Ebbesen, "Exploring superconductivity under strong coupling with the vacuum electromagnetic field," 2019. arXiv:1911.01459.

[53] M. A. Sentef, M. Ruggenthaler, and A. Rubio, "Cavity quantum-electrodynamical polaritonically enhanced electron-phonon coupling and its influence on superconductivity," *Sci. Adv.*, vol. 4, no. 11, 2018.

[54] D. Hagenmüller, J. Schachenmayer, C. Genet, T. W. Ebbesen, and G. Pupillo, "Enhancement of the electron–phonon scattering induced by intrinsic surface plasmon–phonon polaritons," *ACS Photonics*, vol. 6, no. 4, pp. 1073–1081, 2019.

[55] J. B. Curtis, Z. M. Raines, A. A. Allocca, M. Hafezi, and V. M. Galitski, "Cavity quantum eliashberg enhancement of superconductivity," *Phys. Rev. Lett.*, vol. 122, p. 167002, 2019.

[56] A. F. G. Wyatt, V. M. Dmitriev, W. S. Moore, and F. W. Sheard, "Microwave-enhanced critical supercurrents in constricted tin films," *Phys. Rev. Lett.*, vol. 16, pp. 1166–1169, Jun 1966.

[57] A. H. Dayem and J. J. Wiegand, "Behavior of thin-film superconducting bridges in a microwave field," *Phys. Rev.*, vol. 155, pp. 419–428, Mar 1967.

[58] B. I. Ivlev, S. G. Lisitsyn, and G. M. Eliashberg, "Nonequilibrium excitations in superconductors in high-frequency fields," *J. Low Temp. Phys.*, vol. 10, pp. 449–468, Feb 1973.

[59] J. H. Mentink, K. Balzer, and M. Eckstein, "Ultrafast and reversible control of the exchange interaction in Mott insulators," *Nat. Commun.*, vol. 6, no. 1, p. 6708, 2015.

[60] J. R. Coulthard, S. R. Clark, S. Al-Assam, A. Cavalleri, and D. Jaksch, "Enhancement of superexchange pairing in the periodically driven Hubbard model," *Phys. Rev. B*, vol. 96, no. 8, p. 085104, 2017.

[61] F. Görg, M. Messer, K. Sandholzer, G. Jotzu, R. Desbuquois, and T. Esslinger, "Enhancement and sign change of magnetic correlations in a driven quantum many-body system," *Nature*, vol. 553, no. 7689, pp. 481–485, 2018.

[62] M. Kiffner, J. R. Coulthard, F. Schlawin, A. Ardavan, and D. Jaksch, "Manipulating quantum materials with quantum light," *Phys. Rev. B*, vol. 99, p. 085116, 2019.

[63] J. Li and M. Eckstein, "Manipulating intertwined orders in solids with quantum light," *Phys. Rev. Lett.*, vol. 125, p. 217402, Nov 2020.

[64] B. Deveaud, "Exciton-polariton bose-einstein condensates," *Annu. Rev. Condens. Matter Phys.*, vol. 6, no. 1, pp. 155–175, 2015.

[65] N. Y. Kim and Y. Yamamoto, *Exciton-Polariton Quantum Simulators*, pp. 91–121. Cham: Springer International Publishing, 2017.

[66] S. Ghosh and T. C. H. Liew, "Quantum computing with exciton-polariton condensates," *npj Quantum Information*, vol. 6, p. 16, Feb 2020.

[67] F. P. Laussy, A. V. Kavokin, and I. A. Shelykh, "Exciton-polariton mediated superconductivity," *Phys. Rev. Lett.*, vol. 104, p. 106402, Mar 2010.

[68] O. Cotleţ, S. Zeytinoğlu, M. Sigrist, E. Demler, and A. Imamoğlu, "Superconductivity and other collective phenomena in a hybrid bose-fermi mixture formed by a polariton condensate and an electron system in two dimensions," *Phys. Rev. B*, vol. 93, p. 054510, 2016.

[69] A. Kavokin and P. Lagoudakis, "Exciton-mediated superconductivity," *Nat. Mater.*, vol. 15, no. 6, pp. 599–600, 2016.

[70] F. Schlawin, A. Cavalleri, and D. Jaksch, "Cavity-mediated electron-photon superconductivity," *Phys. Rev. Lett.*, vol. 122, p. 133602, 2019.

[71] A. Thomas, J. George, A. Shalabney, M. Dryzhakov, S. J. Varma, J. Moran, T. Chervy, X. Zhong, E. Devaux, C. Genet, J. A. Hutchison, and T. W. Ebbesen, "Ground-state chemical reactivity under vibrational coupling to the vacuum electromagnetic field," *Angew. Chem. Int. Edit.*, vol. 55, no. 38, pp. 11462–11466, 2016.

[72] A. Thomas, L. Lethuillier-Karl, K. Nagarajan, R. M. A. Vergauwe, J. George, T. Chervy, A. Shalabney, E. Devaux, C. Genet, J. Moran, and T. W. Ebbesen, "Tilting a ground-state reactivity landscape by vibrational strong coupling," *Science*, vol. 363, no. 6427, pp. 615–619, 2019.

[73] T. W. Ebbesen, "Hybrid light–matter states in a molecular and material science perspective," *Accounts Chem. Res.*, vol. 49, no. 11, pp. 2403–2412, 2016.

[74] J. Feist, J. Galego, and F. J. Garcia-Vidal, "Polaritonic chemistry with organic molecules," *ACS Photonics*, vol. 5, no. 1, pp. 205–216, 2018.

[75] M. Ruggenthaler, J. Flick, H. Appel, and A. Rubio, "From a quantum-electrodynamical light–matter description to novel spectroscopies," *Nat. Rev. Chem.*, vol. 2, p. 0118, 2018.

[76] E. Orgiu, J. George, J. A. Hutchison, E. Devaux, J. F. Dayen, B. Doudin, F. Stellacci, C. Genet, J. Schachenmayer, C. Genes, G. Pupillo, P. Samori, and T. W. Ebbesen, "Conductivity in organic semiconductors hybridized with the vacuum field," *Nat. Mater.*, vol. 14, p. 1123, 2015.

[77] J. Schachenmayer, C. Genes, E. Tignone, and G. Pupillo, "Cavity-enhanced transport of excitons," *Phys. Rev. Lett.*, vol. 114, p. 196403, 2015.

[78] D. Hagenmüller, J. Schachenmayer, S. Schütz, C. Genes, and G. Pupillo, "Cavity-enhanced transport of charge," *Phys. Rev. Lett.*, vol. 119, p. 223601, 2017.

[79] G. L. Paravicini-Bagliani, F. Appugliese, E. Richter, F. Valmorra, J. Keller, M. Beck, N. Bartolo, C. Rössler, T. Ihn, K. Ensslin, C. Ciuti, G. Scalari, and J. Faist, "Magneto-transport controlled by landau polariton states," *Nat. Phys.*, vol. 15, p. 186, 2019.

[80] N. Bartolo and C. Ciuti, "Vacuum-dressed cavity magnetotransport of a two-dimensional electron gas," *Phys. Rev. B*, vol. 98, p. 205301, Nov 2018.

[81] H. Gao, F. Schlawin, M. Buzzi, A. Cavalleri, and D. Jaksch, "Photoinduced electron pairing in a driven cavity," *Phys. Rev. Lett.*, vol. 125, p. 053602, Jul 2020.

[82] A. Chakraborty and F. Piazza, "Non-BCS-type enhancement of superconductivity from long-range photon fluctuations," 2020.

[83] A. Chiocchetta, D. Kiese, F. Piazza, and S. Diehl, "Cavity-induced quantum spin liquids," 2020.

[84] H. Ritsch, P. Domokos, F. Brennecke, and T. Esslinger, "Cold atoms in cavity-generated dynamical optical potentials," *Rev. Mod. Phys.*, vol. 85, pp. 553–601, Apr 2013.

[85] M. Kira and S. W. Koch, *Semiconductor Quantum Optics*. Cambridge University Press, 2011.

[86] J. Li, D. Golez, G. Mazza, A. J. Millis, A. Georges, and M. Eckstein, "Electromagnetic coupling in tight-binding models for strongly correlated light and matter," *Phys. Rev. B*, vol. 101, p. 205140, 2020.

[87] H. Bruus and K. Flensberg, *Many-body quantum theory in condensed matter physics - an introduction*. United States: Oxford University Press, 2004.

[88] G. Mahan, *Many-Particle Physics*. Physics of Solids and Liquids, Springer US, 2000.

[89] T. Ando, A. B. Fowler, and F. Stern, "Electronic properties of two-dimensional systems," *Rev. Mod. Phys.*, vol. 54, pp. 437–672, 1982.

[90] F. Stern, "Polarizability of a two-dimensional electron gas," *Phys. Rev. Lett.*, vol. 18, pp. 546–548, 1967.

[91] D. N. Basov, R. D. Averitt, and D. Hsieh, "Towards properties on demand in quantum materials," *Nat. Mater.*, vol. 16, p. 1077, 2017.

[92] Y. Cao, V. Fatemi, S. Fang, K. Watanabe, T. Taniguchi, E. Kaxiras, and P. Jarillo-Herrero, "Unconventional superconductivity in magic-angle graphene superlattices," *Nature*, vol. 556, no. 7699, pp. 43–50, 2018.

[93] A. D. Caviglia, S. Gariglio, N. Reyren, D. Jaccard, T. Schneider, M. Gabay, S. Thiel, G. Hammerl, J. Mannhart, and J.-M. Triscone, "Electric field control of the laalo3/srtio3 interface ground state," *Nature*, vol. 456, no. 7222, pp. 624–627, 2008.

[94] J. Keller, G. Scalari, S. Cibella, C. Maissen, F. Appugliese, E. Giovine, R. Leoni, M. Beck, and J. Faist, "Few-electron ultrastrong light-matter coupling at 300 ghz with nanogap hybrid lc microcavities," *Nano. Lett.*, vol. 17, no. 12, pp. 7410–7415, 2017.

[95] N. Kim, S. In, D. Lee, J. Rhie, J. Jeong, D.-S. Kim, and N. Park, "Colossal terahertz field enhancement using split-ring resonators with a sub-10 nm gap," *ACS Photonics*, vol. 5, no. 2, pp. 278–283, 2018.

[96] K. Baumann, C. Guerlin, F. Brennecke, and T. Esslinger, "Dicke quantum phase transition with a superfluid gas in an optical cavity," *Nature*, vol. 464, no. 7293, pp. 1301–1306, 2010.

[97] M. Kira and S. W. Koch, *Interactions in semiconductors*, p. 253–278. Cambridge University Press, 2011.

[98] E. J. Sie, J. W. McIver, Y.-H. Lee, L. Fu, J. Kong, and N. Gedik, "Optical stark effect in 2d semiconductors," *Proc. SPIE*, vol. 9835, 2016.

[99] B. Pasenow, S. W. Koch, J. Hader, J. V. Moloney, M. Sabathil, N. Linder, and S. Lutgen, "Auger losses in gan-based quantum wells: Microscopic theory," *physica status solidi c*, vol. 6, no. S2, pp. S864–S868, 2009.

[100] S. Sadasivam, M. K. Y. Chan, and P. Darancet, "Theory of thermal relaxation of electrons in semiconductors," *Phys. Rev. Lett.*, vol. 119, p. 136602, Sep 2017.

[101] D. H. Dunlap and V. M. Kenkre, "Dynamic localization of a charged particle moving under the influence of an electric field," *Phys. Rev. B*, vol. 34, pp. 3625–3633, 1986.

[102] J. W. McIver, B. Schulte, F.-U. Stein, T. Matsuyama, G. Jotzu, G. Meier, and A. Cavalleri, "Light-induced anomalous Hall effect in graphene," *Nat. Phys.*, vol. 16, no. 1, pp. 38–41, 2020.

[103] J. P. Carbotte, "Properties of boson-exchange superconductors," *Rev. Mod. Phys.*, vol. 62, pp. 1027–1157, 1990.

[104] A. McCollam, S. Wenderich, M. K. Kruize, V. K. Guduru, H. J. A. Molegraaf, M. Huijben, G. Koster, D. H. A. Blank, G. Rijnders, A. Brinkman, H. Hilgenkamp, U. Zeitler, and J. C. Maan, "Quantum oscillations and subband properties of the two-dimensional electron gas at the laalo3/srtio3 interface," *APL Materials*, vol. 2, no. 2, p. 022102, 2014.

[105] S. Thiel, G. Hammerl, A. Schmehl, C. W. Schneider, and J. Mannhart, "Tunable quasi-two-dimensional electron gases in oxide heterostructures," *Science*, vol. 313, no. 5795, pp. 1942–1945, 2006.

[106] F. A. Rasmussen and K. S. Thygesen, "Computational 2d materials database: Electronic structure of transition-metal dichalcogenides and oxides," *J. Phys. Chem. C*, vol. 119, no. 23, pp. 13169–13183, 2015.

[107] P. A. Gusikhin, V. M. Murav'ev, and I. V. Kukushkin, "Observation of plasma waves with anomalously weak damping in a two-dimensional electron system," *JETP Lett.*, vol. 100, no. 10, pp. 648–651, 2015.

[108] T. Sakudo and H. Unoki, "Dielectric properties of srtio$_3$ at low temperatures," *Phys. Rev. Lett.*, vol. 26, pp. 851–853, 1971.

[109] E. H. Hwang and S. Das Sarma, "Dielectric function, screening, and plasmons in two-dimensional graphene," *Phys. Rev. B*, vol. 75, p. 205418, 2007.

[110] M. Fox, *Optical properties of solids*, vol. Oxford master series in condensed matter physics. Oxford University Press, 2001.

[111] A. A. Abrikosov, *Methods of quantum field theory in statistical physics*. New York: Dover Publications, 1975.

[112] N. Reyren, S. Thiel, A. D. Caviglia, L. F. Kourkoutis, G. Hammerl, C. Richter, C. W. Schneider, T. Kopp, A.-S. Rüetschi, D. Jaccard, M. Gabay, D. A. Muller, J.-M. Triscone, and J. Mannhart, "Superconducting interfaces between insulating oxides," *Science*, vol. 317, no. 5842, pp. 1196–1199, 2007.

[113] Z. Yan, Z. Peng, Z. Sun, J. Yao, Y. Zhu, Z. Liu, P. M. Ajayan, and J. M. Tour, "Growth of bilayer graphene on insulating substrates," *ACS Nano*, vol. 5, no. 10, pp. 8187–8192, 2011. PMID: 21888396.

[114] Robertson, J., "High dielectric constant oxides," *Eur. Phys. J. Appl. Phys.*, vol. 28, no. 3, pp. 265–291, 2004.

[115] Q. Zhang, M. Lou, X. Li, J. L. Reno, W. Pan, J. D. Watson, M. J. Manfra, and J. Kono, "Collective non-perturbative coupling of 2d electrons with high-quality-factor terahertz cavity photons," *Nat. Phys.*, vol. 12, no. 11, pp. 1005–1011, 2016.

[116] E. McCann, D. S. L. Abergel, and V. I. Fal'ko, "The low energy electronic band structure of bilayer graphene," *Eur. Phys. J. Spec. Top.*, vol. 148, no. 1, pp. 91–103, 2007.

[117] H. A. Hafez, X. Chai, A. Ibrahim, S. Mondal, D. Férachou, X. Ropagnol, and T. Ozaki, "Intense terahertz radiation and their applications," *J. Opt.*, vol. 18, no. 9, p. 093004, 2016.

[118] K.-L. Yeh, M. C. Hoffmann, J. Hebling, and K. A. Nelson, "Generation of 10μj ultrashort terahertz pulses by optical rectification," *Appl. Phys. Lett.*, vol. 90, no. 17, p. 171121, 2007.

[119] M. C. Hoffmann, J. Hebling, H. Y. Hwang, K.-L. Yeh, and K. A. Nelson, "Thz-pump/thz-probe spectroscopy of semiconductors at high field strengths," *J. Opt. Soc. Am. B*, vol. 26, no. 9, pp. A29–A34, 2009.

[120] C. Vicario, C. Ruchert, F. Ardana-Lamas, P. M. Derlet, B. Tudu, J. Luning, and C. P. Hauri, "Off-resonant magnetization dynamics phase-locked to an intense phase-stable terahertz transient," *Nat. Photonics*, vol. 7, pp. 720–723, 2013.

[121] T. Kubacka, J. A. Johnson, M. C. Hoffmann, C. Vicario, S. de Jong, P. Beaud, S. Grübel, S.-W. Huang, L. Huber, L. Patthey, Y.-D. Chuang, J. J. Turner, G. L. Dakovski, W.-S. Lee, M. P. Minitti, W. Schlotter, R. G. Moore, C. P. Hauri, S. M. Koohpayeh, V. Scagnoli, G. Ingold, S. L. Johnson, and U. Staub, "Large-amplitude spin dynamics driven by a thz pulse in resonance with an electromagnon," *Science*, vol. 343, no. 6177, pp. 1333–1336, 2014.

[122] F. Piazza and P. Strack, "Quantum kinetics of ultracold fermions coupled to an optical resonator," *Phys. Rev. A*, vol. 90, p. 043823, 2014.

[123] R. Landig, L. Hruby, N. Dogra, M. Landini, R. Mottl, T. Donner, and T. Esslinger, "Quantum phases from competing short- and long-range interactions in an optical lattice," *Nature*, vol. 532, pp. 476–479, 2016.

[124] A. Camacho-Guardian, R. Paredes, and S. F. Caballero-Benítez, "Quantum simulation of competing orders with fermions in quantum optical lattices," *Phys. Rev. A*, vol. 96, p. 051602(R), 2017.

[125] J. Fan, X. Zhou, W. Zheng, W. Yi, G. Chen, and S. Jia, "Magnetic order in a fermi gas induced by cavity-field fluctuations," *Phys. Rev. A*, vol. 98, p. 043613, 2018.

[126] F. Schlawin and D. Jaksch, "Cavity-mediated unconventional pairing in ultracold fermionic atoms," *Phys. Rev. Lett.*, vol. 123, p. 133601, 2019.

[127] D. Jaksch, S. A. Gardiner, K. Schulze, J. I. Cirac, and P. Zoller, "Uniting bose-einstein condensates in optical resonators," *Phys. Rev. Lett.*, vol. 86, pp. 4733–4736, 2001.

[128] P. Münstermann, T. Fischer, P. Maunz, P. W. H. Pinkse, and G. Rempe, "Observation of cavity-mediated long-range light forces between strongly coupled atoms," *Phys. Rev. Lett.*, vol. 84, pp. 4068–4071, 2000.

[129] C. Maschler and H. Ritsch, "Cold atom dynamics in a quantum optical lattice potential," *Phys. Rev. Lett.*, vol. 95, p. 260401, 2005.

[130] R. Mottl, F. Brennecke, K. Baumann, R. Landig, T. Donner, and T. Esslinger, "Roton-type mode softening in a quantum gas with cavity-mediated long-range interactions," *Science*, vol. 336, no. 6088, pp. 1570–1573, 2012.

[131] S. Zeytinoğlu, A. m. c. İmamoğlu, and S. Huber, "Engineering matter interactions using squeezed vacuum," *Phys. Rev. X*, vol. 7, p. 021041, 2017.

[132] F. Mivehvar, H. Ritsch, and F. Piazza, "Superradiant topological peierls insulator inside an optical cavity," *Phys. Rev. Lett.*, vol. 118, p. 073602, 2017.

[133] R. M. Kroeze, Y. Guo, V. D. Vaidya, J. Keeling, and B. L. Lev, "Spinor self-ordering of a quantum gas in a cavity," *Phys. Rev. Lett.*, vol. 121, p. 163601, 2018.

[134] V. D. Vaidya, Y. Guo, R. M. Kroeze, K. E. Ballantine, A. J. Kollár, J. Keeling, and B. L. Lev, "Tunable-range, photon-mediated atomic interactions in multimode cavity qed," *Phys. Rev. X*, vol. 8, p. 011002, 2018.

[135] M. A. Norcia, R. J. Lewis-Swan, J. R. K. Cline, B. Zhu, A. M. Rey, and J. K. Thompson, "Cavity-mediated collective spin-exchange interactions in a strontium superradiant laser," *Science*, vol. 361, no. 6399, pp. 259–262, 2018.

[136] Y. Guo, R. M. Kroeze, V. D. Vaidya, J. Keeling, and B. L. Lev, "Sign-changing photon-mediated atom interactions in multimode cavity quantum electrodynamics," *Phys. Rev. Lett.*, vol. 122, p. 193601, 2019.

[137] F. Mivehvar, H. Ritsch, and F. Piazza, "Cavity-quantum-electrodynamical toolbox for quantum magnetism," *Phys. Rev. Lett.*, vol. 122, p. 113603, 2019.

[138] M. Sigrist and K. Ueda, "Phenomenological theory of unconventional superconductivity," *Rev. Mod. Phys.*, vol. 63, pp. 239–311, Apr 1991.

[139] A. Damascelli, Z. Hussain, and Z.-X. Shen, "Angle-resolved photoemission studies of the cuprate superconductors," *Rev. Mod. Phys.*, vol. 75, pp. 473–541, Apr 2003.

[140] I. Giaever, "Energy gap in superconductors measured by electron tunneling," *Phys. Rev. Lett.*, vol. 5, pp. 147–148, Aug 1960.

[141] P. W. Anderson, "Random-phase approximation in the theory of superconductivity," *Phys. Rev.*, vol. 112, pp. 1900–1916, Dec 1958.

[142] R. Shimano and N. Tsuji, "Higgs mode in superconductors," *Annu. Rev. Condens. Matter Phys.*, vol. 11, no. 1, pp. 103–124, 2020.

[143] P. W. Anderson, "Plasmons, gauge invariance, and mass," *Phys. Rev.*, vol. 130, pp. 439–442, Apr 1963.

[144] P. Higgs, "Broken symmetries, massless particles and gauge fields," *Physics Letters*, vol. 12, no. 2, pp. 132–133, 1964.

[145] H. A. Fertig and S. Das Sarma, "Collective modes in layered superconductors," *Phys. Rev. Lett.*, vol. 65, pp. 1482–1485, Sep 1990.

[146] F. J. Dunmore, D. Z. Liu, H. D. Drew, S. Das Sarma, Q. Li, and D. B. Fenner, "Observation of below-gap plasmon excitations in superconducting $YBa_2Cu_3O_7$ films," *Phys. Rev. B*, vol. 52, pp. R731–R734, Jul 1995.

[147] R. Matsunaga, N. Tsuji, H. Fujita, A. Sugioka, K. Makise, Y. Uzawa, H. Terai, Z. Wang, H. Aoki, and R. Shimano, "Light-induced collective pseudospin precession resonating with Higgs mode in a superconductor," *Science*, vol. 345, no. 6201, pp. 1145–1149, 2014.

[148] M. V. Klein and S. B. Dierker, "Theory of raman scattering in superconductors," *Phys. Rev. B*, vol. 29, pp. 4976–4991, May 1984.

[149] J. Goldstone, "Field theories with superconductor solutions," *Il Nuovo Cimento (1955-1965)*, vol. 19, pp. 154–164, Jan 1961.

[150] A. F. Volkov and S. M. Kogan, "Collisionless relaxation of the energy gap in superconductors," *J. Exp. Theor. Phys*, vol. 38, p. 1018, 1973.

[151] Z. Sun, M. M. Fogler, D. N. Basov, and A. J. Millis, "Collective modes and terahertz near-field response of superconductors," *Phys. Rev. Research*, vol. 2, p. 023413, Jun 2020.

[152] R. Matsunaga, Y. I. Hamada, K. Makise, Y. Uzawa, H. Terai, Z. Wang, and R. Shimano, "Higgs amplitude mode in the BCS superconductors $Nb_{1-x}Ti_xN$ induced by terahertz pulse excitation," *Phys. Rev. Lett.*, vol. 111, p. 057002, Jul 2013.

[153] C. Vaswani, J. H. Kang, M. Mootz, L. Luo, X. Yang, C. Sundahl, D. Cheng, C. Huang, R. H. J. Kim, Z. Liu, Y. G. Collantes, E. E. Hellstrom, I. E. Perakis, C. B. Eom, and J. Wang, "Light quantum control of persisting Higgs modes in iron-based superconductors," *Nat. Commun.*, vol. 12, p. 258, Jan 2021.

[154] M. Buzzi, G. Jotzu, A. Cavalleri, J. I. Cirac, E. A. Demler, B. I. Halperin, M. D. Lukin, T. Shi, Y. Wang, and D. Podolsky, 2019.

[155] D. N. Basov, M. M. Fogler, A. Lanzara, F. Wang, and Y. Zhang, "Colloquium: Graphene spectroscopy," *Rev. Mod. Phys.*, vol. 86, pp. 959–994, Jul 2014.

[156] R. Sooryakumar and M. V. Klein, "Raman scattering by superconducting-gap excitations and their coupling to charge-density waves," *Phys. Rev. Lett.*, vol. 45, pp. 660–662, Aug 1980.

[157] M.-A. Méasson, Y. Gallais, M. Cazayous, B. Clair, P. Rodière, L. Cario, and A. Sacuto, "Amplitude Higgs mode in the $2H-\mathrm{NbSe_2}$ superconductor," *Phys. Rev. B*, vol. 89, p. 060503, Feb 2014.

[158] R. Grasset, T. Cea, Y. Gallais, M. Cazayous, A. Sacuto, L. Cario, L. Benfatto, and M.-A. Méasson, "Higgs-mode radiance and charge-density-wave order in $2H-\mathrm{NbSe_2}$," *Phys. Rev. B*, vol. 97, p. 094502, Mar 2018.

[159] D. Sherman, U. S. Pracht, B. Gorshunov, S. Poran, J. Jesudasan, M. Chand, P. Raychaudhuri, M. Swanson, N. Trivedi, A. Auerbach, M. Scheffler, A. Frydman, and M. Dressel, "The higgs mode in disordered superconductors close to a quantum phase transition," *Nat. Phys.*, vol. 11, pp. 188–192, Feb 2015.

[160] D. Hagenmüller, J. Schachenmayer, C. Genet, T. W. Ebbesen, and G. Pupillo, "Enhancement of the electron–phonon scattering induced by intrinsic surface plasmon–phonon polaritons," *ACS Photonics*, vol. 6, no. 4, pp. 1073–1081, 2019.

[161] R. D. Parks, *Superconductivity.* New York: M. Dekker, 1969.

[162] X.-L. Qi and S.-C. Zhang, "Topological insulators and superconductors," *Rev. Mod. Phys.*, vol. 83, pp. 1057–1110, Oct 2011.

[163] M. Sato and Y. Ando, "Topological superconductors: a review," *Rep. Prog. Phys.*, vol. 80, p. 076501, may 2017.

[164] L. Schwarz, B. Fauseweh, N. Tsuji, N. Cheng, N. Bittner, H. Krull, M. Berciu, G. S. Uhrig, A. P. Schnyder, S. Kaiser, and D. Manske, "Classification and characterization of nonequilibrium higgs modes in unconventional superconductors," *Nat. Commun.*, vol. 11, p. 287, Jan 2020.

[165] H. Krull, N. Bittner, G. S. Uhrig, D. Manske, and A. P. Schnyder, "Coupling of Higgs and Leggett modes in non-equilibrium superconductors," *Nat. Commun.*, vol. 7, p. 11921, Jun 2016.

[166] J.-J. Chang and D. J. Scalapino, "Nonequilibrium superconductivity," *J. Low Temp. Phys.*, vol. 31, no. 1, pp. 1–32, 1978.

[167] D. N. Basov and T. Timusk, "Electrodynamics of high-T_c superconductors," *Rev. Mod. Phys.*, vol. 77, pp. 721–779, Aug 2005.

[168] A. Dienst, M. C. Hoffmann, D. Fausti, J. C. Petersen, S. Pyon, T. Takayama, H. Takagi, and A. Cavalleri, "Bi-directional ultrafast electric-field gating of interlayer charge transport in a cuprate superconductor," *Nat. Photonics*, vol. 5, no. 8, pp. 485–488, 2011.

[169] Y. Laplace and A. Cavalleri, "Josephson plasmonics in layered superconductors," *Adv. Phys-X*, vol. 1, no. 3, pp. 387–411, 2016.

[170] P. E. Dolgirev, A. Zong, M. H. Michael, J. B. Curtis, D. Podolsky, A. Cavalleri, and E. Demler, "Periodic dynamics in superconductors induced by an impulsive optical quench," 2021.

[171] A. Bardasis and J. R. Schrieffer, "Excitons and plasmons in superconductors," *Phys. Rev.*, vol. 121, pp. 1050–1062, Feb 1961.

[172] A. A. Allocca, Z. M. Raines, J. B. Curtis, and V. M. Galitski, "Cavity superconductor-polaritons," *Phys. Rev. B*, vol. 99, p. 020504(R), 2019.

[173] H. Chu, M.-J. Kim, K. Katsumi, S. Kovalev, R. D. Dawson, L. Schwarz, N. Yoshikawa, G. Kim, D. Putzky, Z. Z. Li, H. Raffy, S. Germanskiy, J.-C. Deinert, N. Awari, I. Ilyakov, B. Green, M. Chen, M. Bawatna, G. Cristiani, G. Logvenov, Y. Gallais, A. V. Boris, B. Keimer, A. P. Schnyder, D. Manske, M. Gensch, Z. Wang, R. Shimano, and S. Kaiser, "Phase-resolved Higgs response in superconducting cuprates," *Nat. Commun.*, vol. 11, p. 1793, Apr 2020.

[174] Y. Murakami, P. Werner, N. Tsuji, and H. Aoki, "Multiple amplitude modes in strongly coupled phonon-mediated superconductors," *Phys. Rev. B*, vol. 93, p. 094509, Mar 2016.

[175] F. Kretzschmar, B. Muschler, T. Böhm, A. Baum, R. Hackl, H.-H. Wen, V. Tsurkan, J. Deisenhofer, and A. Loidl, "Raman-scattering detection of nearly degenerate s-wave and d-wave pairing channels in iron-based $Ba_{0.6}K_{0.4}Fe_2As_2$ and $Rb_{0.8}Fe_{1.6}Se_2$ superconductors," *Phys. Rev. Lett.*, vol. 110, p. 187002, May 2013.

[176] T. Böhm, A. F. Kemper, B. Moritz, F. Kretzschmar, B. Muschler, H.-M. Eiter, R. Hackl, T. P. Devereaux, D. J. Scalapino, and H.-H. Wen, "Balancing act: Evidence for a strong subdominant d-wave pairing channel in $Ba_{0.6}K_{0.4}Fe_2As_2$," *Phys. Rev. X*, vol. 4, p. 041046, Dec 2014.

[177] D. Jost, J.-R. Scholz, U. Zweck, W. R. Meier, A. E. Böhmer, P. C. Canfield, N. Lazarević, and R. Hackl, "Indication of subdominant d-wave interaction in superconducting $CaKFe_4As_4$," *Phys. Rev. B*, vol. 98, p. 020504, Jul 2018.

[178] N. Tsuji and H. Aoki, "Theory of Anderson pseudospin resonance with Higgs mode in superconductors," *Phys. Rev. B*, vol. 92, p. 064508, Aug 2015.

[179] Z. M. Raines, A. A. Allocca, M. Hafezi, and V. M. Galitski, "Cavity higgs polaritons," *Phys. Rev. Research*, vol. 2, p. 013143, Feb 2020.

[180] M. B. Lundeberg, Y. Gao, R. Asgari, C. Tan, B. Van Duppen, M. Autore, P. Alonso-González, A. Woessner, K. Watanabe, T. Taniguchi, R. Hillenbrand, J. Hone, M. Polini, and F. H. L. Koppens, "Tuning quantum nonlocal effects in graphene plasmonics," *Science*, vol. 357, no. 6347, pp. 187–191, 2017.

[181] E. J. C. Dias, D. A. Iranzo, P. A. D. Gonçalves, Y. Hajati, Y. V. Bludov, A.-P. Jauho, N. A. Mortensen, F. H. L. Koppens, and N. M. R. Peres, "Probing nonlocal effects in metals with graphene plasmons," *Phys. Rev. B*, vol. 97, p. 245405, Jun 2018.

[182] G. X. Ni, A. S. McLeod, Z. Sun, L. Wang, L. Xiong, K. W. Post, S. S. Sunku, B.-Y. Jiang, J. Hone, C. R. Dean, M. M. Fogler, and D. N. Basov, "Fundamental limits to graphene plasmonics," *Nature*, vol. 557, pp. 530–533, May 2018.

[183] S. Wang, S. Zhao, Z. Shi, F. Wu, Z. Zhao, L. Jiang, K. Watanabe, T. Taniguchi, A. Zettl, C. Zhou, and F. Wang, "Nonlinear luttinger liquid plasmons in semiconducting single-walled carbon nanotubes," *Nat. Mater.*, vol. 19, pp. 986–991, Sep 2020.

[184] D. Pekker and C. Varma, "Amplitude/Higgs modes in condensed matter physics," *Annu. Rev. Condens. Matter Phys.*, vol. 6, no. 1, pp. 269–297, 2015.

[185] T. Cea, D. Bucheli, G. Seibold, L. Benfatto, J. Lorenzana, and C. Castellani, "Optical excitation of phase modes in strongly disordered superconductors," *Phys. Rev. B*, vol. 89, p. 174506, May 2014.

[186] D. Podolsky, A. Auerbach, and D. P. Arovas, "Visibility of the amplitude (Higgs) mode in condensed matter," *Phys. Rev. B*, vol. 84, p. 174522, Nov 2011.

[187] P. B. Littlewood and C. M. Varma, "Gauge-invariant theory of the dynamical interaction of charge density waves and superconductivity," *Phys. Rev. Lett.*, vol. 47, pp. 811–814, Sep 1981.

[188] P. B. Littlewood and C. M. Varma, "Amplitude collective modes in superconductors and their coupling to charge-density waves," *Phys. Rev. B*, vol. 26, pp. 4883–4893, Nov 1982.

[189] T. Cea and L. Benfatto, "Nature and raman signatures of the Higgs amplitude mode in the coexisting superconducting and charge-density-wave state," *Phys. Rev. B*, vol. 90, p. 224515, Dec 2014.

[190] A. J. Leggett, "The ubiquity of superconductivity," *Annu. Rev. Condens. Matter Phys.*, vol. 2, no. 1, pp. 11–30, 2011.

[191] J. Waldram, *Superconductivity Of Metals and Cuprates.* Bristol: Institute of Physics Publishing, 1996.

[192] L. Rademaker, Y. Wang, T. Berlijn, and S. Johnston, "Enhanced superconductivity due to forward scattering in FeSe thin films on $SrTiO_3$ substrates," *New J. Phys.*, vol. 18, p. 022001, feb 2016.

[193] G. Singh, A. Jouan, L. Benfatto, F. Couëdo, P. Kumar, A. Dogra, R. C. Budhani, S. Caprara, M. Grilli, E. Lesne, A. Barthélémy, M. Bibes, C. Feuillet-Palma, J. Lesueur, and N. Bergeal, "Competition between electron pairing and

phase coherence in superconducting interfaces," *Nat. Commun.*, vol. 9, p. 407, Jan 2018.

[194] K. Yang and S. L. Sondhi, "Low-energy collective modes, Ginzburg-Landau theory, and pseudogap behavior in superconductors with long-range pairing interactions," *Phys. Rev. B*, vol. 62, pp. 11778–11792, Nov 2000.

[195] K. S. Tikhonov, M. A. Skvortsov, and T. M. Klapwijk, "Superconductivity in the presence of microwaves: Full phase diagram," *Phys. Rev. B*, vol. 97, p. 184516, May 2018.

[196] E. A. Yuzbashyan, B. L. Altshuler, V. B. Kuznetsov, and V. Z. Enolskii, "Nonequilibrium cooper pairing in the nonadiabatic regime," *Phys. Rev. B*, vol. 72, p. 220503, Dec 2005.

[197] E. A. Yuzbashyan, O. Tsyplyatyev, and B. L. Altshuler, "Relaxation and persistent oscillations of the order parameter in fermionic condensates," *Phys. Rev. Lett.*, vol. 96, p. 097005, Mar 2006.

[198] B. Mansart, J. Lorenzana, A. Mann, A. Odeh, M. Scarongella, M. Chergui, and F. Carbone, "Coupling of a high-energy excitation to superconducting quasiparticles in a cuprate from coherent charge fluctuation spectroscopy," *Proc. Natl. Acad. Sci. U.S.A.*, vol. 110, no. 12, pp. 4539–4544, 2013.

[199] C. Chin, R. Grimm, P. Julienne, and E. Tiesinga, "Feshbach resonances in ultracold gases," *Rev. Mod. Phys.*, vol. 82, pp. 1225–1286, Apr 2010.

[200] M. Randeria and E. Taylor, "Crossover from Bardeen-Cooper-Schrieffer to Bose-Einstein condensation and the unitary fermi gas," *Annu. Rev. Condens. Matter Phys.*, vol. 5, no. 1, pp. 209–232, 2014.

[201] R. Combescot, M. Y. Kagan, and S. Stringari, "Collective mode of homogeneous superfluid fermi gases in the BEC-BCS crossover," *Phys. Rev. A*, vol. 74, p. 042717, Oct 2006.

[202] R. B. Diener, R. Sensarma, and M. Randeria, "Quantum fluctuations in the superfluid state of the BCS-BEC crossover," *Phys. Rev. A*, vol. 77, p. 023626, Feb 2008.

[203] A. Altland and B. D. Simons, *Condensed Matter Field Theory*. Cambridge University Press, 2 ed., 2010.

[204] F. Peronaci, M. Schiró, and M. Capone, "Transient dynamics of d-wave superconductors after a sudden excitation," *Phys. Rev. Lett.*, vol. 115, p. 257001, Dec 2015.

[205] G. Nemova and R. Kashyap, "Laser cooling of solids," *Rep. Prog. Phys.*, vol. 73, no. 8, p. 086501, 2010.

[206] J. Hammer, M. Aprili, and I. Petković, "Microwave cooling of josephson plasma oscillations," *Phys. Rev. Lett.*, vol. 107, p. 017001, 2011.

[207] K. Sengupta, S. Powell, and S. Sachdev, "Quench dynamics across quantum critical points," *Phys. Rev. A*, vol. 69, p. 053616, May 2004.

[208] M. A. Cazalilla, "Effect of suddenly turning on interactions in the luttinger model," *Phys. Rev. Lett.*, vol. 97, p. 156403, Oct 2006.

[209] M. Cheneau, P. Barmettler, D. Poletti, M. Endres, P. Schauss, T. Fukuhara, C. Gross, I. Bloch, C. Kollath, and S. Kuhr, "Light-cone-like spreading of correlations in a quantum many-body system.," *Nature*, vol. 481, no. 7382, pp. 484–7, 2012.

[210] S. Trotzky, Y.-A. Chen, A. Flesch, I. P. McCulloch, U. Schollwöck, J. Eisert, and I. Bloch, "Probing the relaxation towards equilibrium in an isolated strongly correlated one-dimensional Bose gas," *Nat. Phys.*, vol. 8, pp. 325–330, feb 2012.

[211] J. Schachenmayer, B. P. Lanyon, C. F. Roos, and A. J. Daley, "Entanglement growth in quench dynamics with variable range interactions," *Phys. Rev. X*, vol. 3, p. 031015, Sep 2013.

[212] S. Ruffo, "Dynamics and thermodynamics of systems with long-range interactions.," in *Abstract Book of the XXIII IUPAP International Conference on Statistical Physics*, Genova, Italy: Springer-Verlag Berlin Heidelberg, 9-13 July 2007.

[213] A. Mitra, "Quantum quench dynamics," *Annu. Rev. Condens. Matter Phys.*, vol. 9, no. 1, pp. 245–259, 2018.

[214] D. A. Abanin, E. Altman, I. Bloch, and M. Serbyn, "Colloquium: Many-body localization, thermalization, and entanglement," *Rev. Mod. Phys.*, vol. 91, p. 021001, May 2019.

[215] M. Halbhuber, J. Mornhinweg, V. Zeller, C. Ciuti, D. Bougeard, R. Huber, and C. Lange, "Non-adiabatic stripping of a cavity field from electrons in the deep-strong coupling regime," *Nat. Photonics*, vol. 14, pp. 675–679, Nov 2020.

[216] K. Kamarás, K. Barth, F. Keilmann, R. Henn, M. Reedyk, C. Thomsen, M. Cardona, J. Kircher, P. L. Richards, and J. Stehlé, "The low-temperature infrared optical functions of $SrTiO_3$ determined by reflectance spectroscopy and spectroscopic ellipsometry," *J. Appl. Phys.*, vol. 78, no. 2, pp. 1235–1240, 1995.

[217] V. Fritsch, J. Hemberger, M. V. Eremin, H.-A. Krug von Nidda, F. Lichtenberg, R. Wehn, and A. Loidl, "Magnetization and specific heat of $LaTiO_3$," *Phys. Rev. B*, vol. 65, p. 212405, 2002.

[218] Y. Suemune, "Thermal conductivity of $BaTiO_3$ and $SrTiO_3$ from 4.5° to 300°K," *J. Phys. Soc. Japan*, vol. 20, no. 1, pp. 174–175, 1965.

[219] H. Wang, X. Huang, J. Lin, J. Cui, Y. Chen, C. Zhu, F. Liu, Q. Zeng, J. Zhou, P. Yu, X. Wang, H. He, S. H. Tsang, W. Gao, K. Suenaga, F. Ma, C. Yang, L. Lu, T. Yu, E. H. T. Teo, G. Liu, and Z. Liu, "High-quality monolayer superconductor $NbSe_2$ grown by chemical vapour deposition," *Nat. Commun.*, vol. 8, p. 394, Aug 2017.

[220] A. F. Hebard, M. J. Rosseinsky, R. C. Haddon, D. W. Murphy, S. H. Glarum, T. T. M. Palstra, A. P. Ramirez, and A. R. Kortan, "Superconductivity at 18 K in potassium-doped C60," *Nature*, vol. 350, pp. 600–601, Apr 1991.